IntechOpen

Optical Amplifiers

A Few Different Dimensions

Edited by Pankaj Kumar Choudhury

OPTICAL AMPLIFIERS - A FEW DIFFERENT DIMENSIONS

Edited by **Pankaj Kumar Choudhury**

Optical Amplifiers - A Few Different Dimensions
http://dx.doi.org/10.5772/intechopen.70912
Edited by Pankaj Kumar Choudhury

Contributors

Mingming Tan, Boris I. Lembrikov, Yossef Ben-Ezra, Kyo Inoue, Jing Huang, Amira Tandirovic Gursel, Pankaj Kumar Choudhury

© The Editor(s) and the Author(s) 2018
The rights of the editor(s) and the author(s) have been asserted in accordance with the Copyright, Designs and Patents Act 1988. All rights to the book as a whole are reserved by INTECHOPEN LIMITED. The book as a whole (compilation) cannot be reproduced, distributed or used for commercial or non-commercial purposes without INTECHOPEN LIMITED's written permission. Enquiries concerning the use of the book should be directed to INTECHOPEN LIMITED rights and permissions department (permissions@intechopen.com).
Violations are liable to prosecution under the governing Copyright Law.

Individual chapters of this publication are distributed under the terms of the Creative Commons Attribution 3.0 Unported License which permits commercial use, distribution and reproduction of the individual chapters, provided the original author(s) and source publication are appropriately acknowledged. If so indicated, certain images may not be included under the Creative Commons license. In such cases users will need to obtain permission from the license holder to reproduce the material. More details and guidelines concerning content reuse and adaptation can be foundat http://www.intechopen.com/copyright-policy.html.

Notice

Statements and opinions expressed in the chapters are these of the individual contributors and not necessarily those of the editors or publisher. No responsibility is accepted for the accuracy of information contained in the published chapters. The publisher assumes no responsibility for any damage or injury to persons or property arising out of the use of any materials, instructions, methods or ideas contained in the book.

First published in London, United Kingdom, 2018 by IntechOpen
eBook (PDF) Published by IntechOpen, 2019
IntechOpen is the global imprint of INTECHOPEN LIMITED, registered in England and Wales, registration number: 11086078, The Shard, 25th floor, 32 London Bridge Street
London, SE19SG – United Kingdom
Printed in Croatia

British Library Cataloguing-in-Publication Data
A catalogue record for this book is available from the British Library

Additional hard and PDF copies can be obtained from orders@intechopen.com

Optical Amplifiers - A Few Different Dimensions
Edited by Pankaj Kumar Choudhury

p. cm.

Print ISBN 978-1-78923-498-5

Online ISBN 978-1-78923-499-2

eBook (PDF) ISBN 978-1-83881-480-9

Meet the editor

Pankaj Kumar Choudhury held academic/research positions in the Banaras Hindu University (Varanasi, India), Goa University (Goa, India), Laval University (Quebec, Canada), Gunma University (Kiryu, Japan), Multimedia University (Cyberjaya, Malaysia), and Telekom R&D (Malaysia). He is currently a professor at the Institute of Microengineering and Nanoelectronics, Universiti Kebangsaan Malaysia (Bangi, Malaysia). His research focuses on photonics. He has published over 220 research papers, 12 chapters in research-level books, and edited and coedited 4 books. He is an editorial board member of *Optik—International Journal for Light and Electron Optics* (Elsevier, The Netherlands) and the editor in chief of the *Journal of Electromagnetic Waves and Applications* (Taylor & Francis, UK). He is also a senior member of IEEE, OSA, and SPIE.

Contents

Preface

This book covers a few different aspects of solid-state and fiber-based optical amplifiers in terms of fundamental understanding and applications. Some of the chapters highlight the design principles to be used for communication channels, whereas some review on the recent developments. As such, the book essentially provides readers a glimpse of a few different dimensions in which the operation of optical amplifiers relies on.

Chapter 1 remains the introductory type, wherein a *revisit* is made up of optical amplifiers and their operational principles. A few different types of fundamentally used optical amplifiers are touched upon in this chapter in cursory form, so that the novice readers would have enough foundation before they jump into the following chapters in the book. This chapter partially says about semiconductor optical amplifiers (SOAs), which constitute one of the prime areas of research on solid-state kind of optical amplifiers. These are much useful in applications like wavelength converters and preamplifiers to increase the receiver sensitivity. However, these suffer from the drawbacks of polarization sensitivity, interchannel cross talk, and large coupling loss. Within the context, Chapter 2 of this book emphasizes on a new form of SOA, namely, quantum-dot SOA, in which *Ezra* and *Lembrikov* discussed the dynamics of these amplifiers theoretically and highlighted the applications. This chapter gives a glimpse of quantum dot–based SOAs, which the readers would benefit from, in order to design different amplifier configurations.

While the fiber-based amplifiers are in use, intense incident electric fields result into nonlinear effects. These would be useful in designing efficient parametric amplifiers with improved signal-to-noise ratio. *Jing Huang* reviews such amplifiers in Chapter 3, wherein the discussions are made on the ways to exploit these in optical communication systems. The chapter digs into the theoretical understanding of the subject and enlightens a few relevant configurations. The applications of parametric amplifiers for phase and amplitude regeneration of differential forms of signals are touched upon.

Raman scattering is a nonlinear phenomenon, which would take place in optical fibers, and can be used in achieving laser action. As a consequence, Raman fiber lasers can be developed upon utilizing Raman scattering. *Mingming Tan* puts a detailed study of Raman fiber laser-based amplification techniques and their applications in distant communication links (Chapter 4). Within the context, the author takes up different design issues and discusses their relative merits and demerits.

As fiber lasers are prudent in optical communication systems, the doping media in the host play vital roles in determining the gain and noise figure-related properties of amplifier. Chapter 5 by *Amira Tandirovic Gursel* reviews a few different forms of doped fiber amplifiers and incorporates the exploitation of the features of fiber lasers in medical arena. The chapter remains informative in the sense of throwing knowledge with respect to fundamentals of fiber lasers and their applications in medical diagnostics.

During the operation of optical amplifiers, the noise-related parameters remain of high importance as these essentially degrade the signal quality. In Chapter 6 of this book, *Kyo Inoue* discusses the topic of quantum noise in optical amplifiers. Within the context, the quantum mechanical treatment based on the Heisenberg equation for physical quantity operators is taken up to determine quantum optical properties of amplifiers. The presented study essentially remains of paramount importance owing to the reasons as discussed before.

The aforementioned glimpse of the book—*Optical Amplifiers: A Few Different Dimensions*—essentially leaves the impression of the volume highlighting on some fundamental and advanced aspects of solid-state and fiber-based amplifiers and their applications in optical communication channels. The six chapters of this book stand in their own ways to meet the expectations of the authors. The editor hopes the book to be useful for R&D scientists in laboratories and academic setups.

Pankaj Kumar Choudhury
Institute of Microengineering and Nanoelectronics
Universiti Kebangsaan Malaysia
Bangi, Malaysia

Chapter 1

Introductory Chapter: A Revisit to Optical Amplifiers

Pankaj Kumar Choudhury

Additional information is available at the end of the chapter

http://dx.doi.org/10.5772/intechopen.78671

1. Introduction

The modern age of information may be regarded as the era of fast- and high-bandwidth communication, which exploits fiber-optic communication system. Transmission of signals spanning distances of over thousands of kilometers essentially cause signal degradation. Due to varieties of loss mechanisms in the medium (the optical channel used for transmission), there happens gradual attenuation in the power of signals being transmitted, as those propagate through a communication channel. Clearly, the attenuation imposed by the medium remains a serious issue that affects light propagating ultra-long distances through a fiber-optic cable (the communication link). The degradation of signal must be overcome, which makes the utilization of the process of amplification (of signal) vital. Further, in order for the information carried by a signal to be detectable at the receiving end, there must be a minimum amount of threshold power, which the signal must possess. As such, optical amplifiers, which would incorporate optical fibers and/or waveguides, remain indispensable in fiber-optic communication systems owing to the limitations imposed by the transmission channels/systems. These limitations would arrive in the form of fiber loss and dispersion, which are usually overcome by exploiting varieties of amplifiers. In reality, loss and dispersion are related to each other [1], which can be well-understood upon giving a thought to a pulse shape—more broad a pulse becomes (causing dispersion), more will be the decrease in power (causing loss), and vice-versa.

In earlier days, optoelectronic repeaters were in use for the purpose of amplification, wherein the optical signal is first converted into an electric current, and then regenerated using a transmitter [2]. However, the process of regeneration used to be quite complex and expensive, in particular, when multichannel optical systems are in use. As such, the exploitation of optical amplifier evolved as the alternative approach for amplifying optical signals during transmission. It is a device that directly amplifies an optical signal, without the need of conversion to an electrical signal—the feature needed in the *so-called* repeaters.

2. The mechanism involved

To the very fundamental level, optical amplifiers amplify the incident light through the process of stimulated emission—the mechanism similar to what exploited in the operation of lasers. One would say that optical amplifiers are, in fact, lasers without feedback mechanism, and the optical gain is realized when the amplifier is pumped to achieve population inversion [3]. The achieved optical gain depends not only on the frequency of the incident optical signal, but also, the local beam intensity at any point inside the amplifier. As such, the bandwidth of an amplifier remains greatly important as it determines the frequency and intensity dependence of the optical gain (of an amplifier).

3. A few different amplifier types

Optical amplifiers can be of varieties of forms ranging from the solid-state type to the fiber-based ones [2]. Usually the operation of an optical amplifier relies on the process of feedback, which essentially yields enough gain corresponding to the frequency of signal. An optical amplifier can also be without feedback—the category addressed as traveling wave amplifiers [4]. In these, the amplified signal travels in the forward direction only. In solid-state kind of amplifiers, the resonator is generally made of certain solid materials (e.g., semiconductors), the shape and structure of which tailor the gain parameter. On the other hand, fiber-based amplifiers would rely on the phenomenon of inelastic scattering of light, and/or certain dopants (in the fiber) would make the guide itself an *all-optical* type of structure to yield the required amount of gain. In this section, a few different types of optical amplifiers are touched upon in cursory form.

3.1. Semiconductor optical amplifiers

Semiconductor optical amplifiers (SOAs) fall in the category of solid-state amplifier, wherein semiconductor lasers are used [5]. These experience a relatively large amount of feedback because of multiple reflections (of light) occurring at the cleaved facets of the Fabry-Perot (FP) kind of laser cavity. As such, SOAs can be used as amplifiers when biased below threshold. These amplifiers are easy to fabricate, but the optical signal gain remains highly sensitive to the variations in temperature (of amplifier) and the input optical frequency.

If the SOA is to be of the traveling wave type, the feedback due to reflection from the end facets is to be suppressed. A simple way to reduce the reflectivity would be to coat the facets with a kind of antireflection coating. Indeed, the reflectivity of one of the facets must be extremely small (<0.1%) for the SOA to be operated as a traveling wave amplifier. The minimum amount reflectivity would depend on the amplifier gain. However, it remains almost impossible to realize low reflectivity values of facets in a predictable form—the feature that motivated to investigate other possibilities to achieve the same. Within the context, one of the possibilities would be to use a tilted resonator cavity in laser. In such a kind of laser structure, the angled-facet makes the reflected light to be physically separated from the light propagating in the forward direction. However, to attain a vanishing amount of feedback is almost impossible, due to the physical properties of light propagating in a guiding channel. Apart from this kind of structure, another form would be to use a window-facet structure, wherein a *transparent* window in implanted between the ends of active region and the facets. Losses take place in such structures due to the spreading of signal in the window section—the feature that causes to minimize the reflectivity.

3.2. Fiber Raman amplifiers

It has been known that the response of any dielectric medium to light becomes nonlinear in the case of high electric fields. Such nonlinearities would result in nonlinear (or inelastic) scattering, and the frequency of the scattered light would be downshifted, thereby resulting into a kind of loss (in the fiber). As such, the scattering of photon contributes to the loss of power at the incident frequency. However, corresponding to low incident power levels, the scattering cross-sections remain very small, and therefore, the loss becomes negligible. On the other hand, for high incident optical fields, the nonlinear phenomenon of stimulated Raman scattering (SRS) takes place that leads to a considerable amount of loss. Once the incident optical power exceeds a threshold value, the intensity of the scattered light grows exponentially.

In fiber Raman amplifiers, SRS takes place in silica fibers in the case, when an intense optical pump signal propagates through it [6]. Here the incident pump photon gives up its energy to create another photon of reduced energy at a lower frequency. The remaining amount of energy is absorbed by the medium in the form of molecular vibrations, thereby generating optical phonons. As such, fiber Raman amplifiers are pumped optically to achieve gain. The difference in energy is known as Stokes shift. The pump and signal frequencies are injected into a fiber, and the energy is *transferred* from the pump beam to the signal beam through the process of SRS, as the two beams co-propagate along the fiber. The pump and signal beams can also be injected into the fiber in such a way that they would counter-propagate (inside the fiber). Indeed, it depends on the pumping configurations used to achieve the required amount of gain with certain merits and demerits.

Fiber Raman amplifiers exhibit broad bandwidth—the feature which remains useful for amplifying several channels simultaneously, and also, short optical pulses [7]. These amplifiers can also be used to overcome fiber loss in soliton-based communication systems, and therefore, highly recommended for distributed amplification. However, these suffer from the drawback of the need of high-power lasers for optical pumping, thereby making the communication not enough cost-effective.

3.3. Fiber Brillouin amplifiers

Fiber Brillouin amplifiers operate similarly to fiber Raman amplifiers except that the gain in this case is provided by the process of stimulated Brillouin scattering (SBS), instead of SRS. When such amplifiers are pumped optically, a part of the pump power is transferred to the signal through SBS [8–13]. Each pump photon uses most of its energy to create a signal photon, and the remaining amount of energy is used to excite an acoustic phonon. As such, the amplifier system relies on acoustic phonons, instead of optical phonons, as we come across in the case of fiber Raman amplifiers [14, 15]. The phenomenon of SBS differs from SRS in the following forms:

- In SBS, amplification occurs only when the signal beam propagates in a direction opposite to that of the pump beam (backward pumping configuration), whereas in the case of SRS, both kinds of configurations would be exploited.
- The Stokes shift in SBS is smaller (nearly 10 GHz) by three orders of magnitude compared with that obtained in SRS.
- The Brillouin gain spectrum is narrow (less than 100 MHz).

This much amount of narrow bandwidth results into low gain-bandwidth product provided by fiber Brillouin amplifiers, which is the prime disadvantage of this kind of device for the usage in amplifying optical signals in lightwave communication systems. As such, better usage of Fiber Brillouin amplifier would be as preamplifier to improve the receiver sensitivity. In addition, the *noise figure* of such amplifiers is quite large (over 15 dB).

3.4. Doped-fiber amplifiers

Doped-fiber amplifiers make use of rare earth elements (namely erbium, holmium, neodymium, samarium, thulium and ytterbium) as a gain medium (i.e., the cavity resonator). Such elements are doped in usual silica fibers, and therefore, the characteristics of these amplifiers are determined by the dopants rather than by the silica fiber [2]; the latter one plays the role of host medium only. The use of different types of dopants makes the fiber amplifier to operate in different wavelengths covering a range of 0.5–3.5 μm. Among the others, the erbium-doped fiber amplifiers (EDFAs) are greatly attractive as these operate near 1.55 μm wavelength, corresponding to which the fiber loss remains minimum [16, 17]. The key element in EDFA is erbium— a rare earth element in the lanthanide series.

Erbium was a relatively unimportant element in the past, but now it has been postulated that what silicon is to the semiconductor technology, erbium will be to the photonics technology. According to Emmanuel Desurvire [18], small amount of erbium doping in optical fibers —"*makes it possible to distribute the gain over the fiber itself, thereby minimizing the power excursion of the signal. Such an approach makes possible virtually lossless signal transmission from one fiber network to the next.*"

EDFAs can be designed to operate in such a way that the pump and signal beams propagate along the same direction (unidirectional pumping configuration). In bidirectional pumping, the amplifier is pumped in both directions simultaneously by using two semiconductor lasers located at the two fiber ends. Both the types of configurations have their relative merits and demerits. Some of such relevant configurations have been reported before in Refs. [19–21].

The gain characteristics of EDFAs depend on the pumping scheme as well as the other co-dopants, such as germania and alumina—the materials that remain present in the fiber core.

The amorphous nature of silica broadens the energy levels of Er^{3+} ions into Er^{3+} bands—the feature facilitating different possible transitions that can be used to pump the EDFA. Structural disorders lead to inhomogeneous broadening of the EDFA gain profile, whereas Stark splitting of various energy levels is responsible for homogeneous broadening. The addition of alumina to the core broadens the gain spectrum even more.

Efficient EDFA pumping generally requires semiconductor lasers operating near 0.98 and 1.48 μm. The required amount of pump power can be reduced by using silica fibers doped with aluminum and phosphorous or by using fluorophosphate fibers. Within the context, the EDFA gain spectrum can vary from amplifier to amplifier even when the core composition is the same. This is because the EDFA gain also depends on the length of amplifier, that is, the size of FP cavity resonator wherein multiple reflections take place. Gain essentially depends on both the absorption and emission cross-sections, which have distinct spectral characteristics. Apart from these, other device as well as operational parameters, such as Er^{3+} ion concentration, amplifier length, core radius and pump power, also play vital roles to determine EDFA gain spectrum.

EDFAs exhibit relatively low noise levels, making them suitable for applications in lightwave communication systems. Nevertheless, long haul fiber-optic communication systems employing multiple EDFAs suffer from the issues related to amplifier noise. Such problems become severe when the system operates in the anomalous dispersion region of fiber. This happens primarily due to the fact that the nonlinear phenomenon, known as modulation instability, plays a prime role to enhance the amplifier noise, thereby degrading the spectral characteristics of signal.

As stated before, EDFAs are ideal for lightwave communication systems operating near 1.55 μm wavelength. However, worldwide telecommunication network contains huge span of communication link optimized for operations at other wavelengths as well, at 1.3 μm. Clearly, signal amplification in such communication networks needs other forms of amplifiers. Within the context, silica fibers, doped with neodymium ions, would provide fiber amplifiers that can be operated in the 1.30–1.36 μm wavelength span. However, such amplifiers suffer from the undesirable effects, such as excited-state absorption and radiative transitions, thereby limiting the performance characteristics. To overcome the issues, varieties of other forms of amplifiers, such as Nd^{3+} ion-doped fluoride fibers, ZABLAN (ZrF_4-BaF_2-LaF_3-AlF_3-NaF) fibers doped with praseodymium (Pr^{3+}) ions, ytterbium-doped fibers, etc., were investigated with their relative merits and demerits [2].

4. Applications

There can be various forms of applications of optical amplifiers. For example, as stated earlier, the use of optical amplifiers is particularly attractive for multichannel systems since they can amplify all channels simultaneously. The use of SOAs as preamplifiers increases the sensitivity of optical receivers. In such a kind of application, the signal is optically amplified before it falls on the receiver. The preamplifier boosts the signal to a level that the receiver performance is improved in terms of noise figure. Such amplifiers are used in local area networks (LANs) as well in order to compensate the loss due to the distribution of signal. SOAs can also be used as power amplifiers to boost the signal power. Further, a power amplifier can increase the distance of optical transmission by 100 km or more. However, it essentially depends on the amplifier gain and channel loss. Finally, the purpose of using amplifiers in transmission links is to boost the propagating power [2].

After all these different types of applications of SOA, it must be emphasized that these suffer from many drawbacks, namely polarization sensitivity, interchannel cross-talk, and large coupling loss, which essentially limit their usage as in-line amplifiers. Fiber amplifiers do not suffer from such severe issues and can be exploited satisfactorily for signal amplification in the 1.55 μm-based communication links. However, as to the 1.3 μm-based lightwave systems, SOAs remain better alternative because fiber amplifiers do not perform well in this wavelength. Furthermore, SOAs can be used as wavelength converter and fast switch for wavelength routing in wavelength-division-multiplexed (WDM) networks [22].

5. Current scenario

Varieties of optical amplifiers have been put forward by the investigators that are capable for usages based on specific needs. The scope of the present introductory chapter remains out of accounting all those in concise forms. Just to state a few, one may focus on the organic semiconductor lasers, which contribute to major advances in the area of organic light emitting diodes (LEDs). Such semiconductors exhibit high absorption and broadband spectra. Further, their operations in the visible spectrum regime make them highly prudent for many applications [23]. These amplifiers are pumped optically, and day-by-day, the pumping scheme has seen improvements to the extent that compact sources, such as microchip lasers [24], have been in use with high efficiency. High absorption yields large gain, and therefore, the gain-bandwidth product becomes very large for such solid-state amplifiers [25]. Furthermore, these amplifiers exhibit good compatibility with polymer-based optical fibers.

The communication schemes currently employ WDM systems, and therefore, optical amplifiers are designed accordingly so that all the channels with different wavelengths can be simultaneously amplified. As such, the demand remains for optical amplifiers with better performance, in terms of optical nonlinearities, channel crosstalk, gain flatness, large gain-bandwidth product, etc. Meeting these specifications only would make the amplifier suitable for dense-WDM systems. Within the context, hybrid optical amplifiers (HOAs) are of promising use as these are suitably applicable for high-speed broadband applications in cost-effective ways [26]. In fact, the combination of more than one optical amplifier in any configuration is termed as HOA. The implementation of such scheme has the potential benefits of large gain over a broad bandwidth with large channel spacing and reduced nonlinear losses. However, these also suffer from cross talk, noise and nonlinear losses. HOA can be used in DWDM systems where high gain and/or gain bandwidth with less variation is required. However, relative merits and demerits of different configurations have been making the investigators engaged in coming up with new ideas to design such amplifiers with enhanced efficiencies [27–31].

6. Summary

Optical amplifiers are the key components in the present-day distant communication systems, wherein fiber-based networks are vigorously exploited under the principle of WDM. Indeed, merits and demerits remain in adopting different configurations, which essentially depend on the need of operation. The very basic principles of some of the forms of optical amplifiers are discussed in this introductory chapter. This is made primarily with the aim of creating the background before authors read the contributions by the different authors in this Book. Apart from this chapter, there are six other chapters included—all of which are dedicated to the recent advancements in the area of optical amplifiers; the introductory chapter would make the understanding of the remaining part (of the Book) fairly simpler. With such thoughts, the editor of the Book expects the volume to be of help for graduate students as well as established scientists—the former group of readers would generate their own ideas, where the latter ones would foster own research with having glimpse of the ongoing investigations in the relevant field.

Author details

Pankaj Kumar Choudhury

Address all correspondence to: pankaj@ukm.edu.my

Institute of Microengineering and Nanoelectronics, Universiti Kebangsaan Malaysia, UKM, Bangi, Selangor, Malaysia

References

[1] Kaiser G. Optical Fiber Communications. Singapore: McGraw-Hill; 2000

[2] Agrawal G. Fiber-Optic Communication Systems. New York: Academic Press; 2002

[3] Quimby RS. Photonics and Lasers: An Introduction. New York: Wiley; 2006

[4] Desurvire E, Simpson JR, Becker PC. High-gain erbium-doped traveling-wave fiber amplifier. Optics Letters. 1987;**12**:888-890

[5] Liu JM. Photonic Devices. New York: Cambridge; 2005

[6] Aoki Y. Properties of fiber Raman amplifiers and their applicability to digital optical communication systems. Journal of Lightwave Technology. 1988;**6**:1225-1239

[7] Han B, Zhang X, Zhang G, Lu Z, Yang G. Composite broad-band fiber Raman amplifiers using incoherent pumping. Optics Express. 2005;**13**:6023-6032

[8] Nasir MNM, Al-Mansoori MH, Abdul Rashid HA, Choudhury PK, Yusoff Z. Multi-wavelength Brillouin erbium fiber laser incorporating a fiber Bragg grating filter. Laser Physics. 2008;**18**:446-448

[9] Nasir MNM, Yusoff Z, Al-Mansoori MH, Abdul Rashid HA, Choudhury PK. Broadly tunable multi-wavelength Brillouin-erbium fiber laser in a Fabry-Perot cavity. Laser Physics Letters. 2008;**5**:812-816

[10] Nasir MNM, Yusoff Z, Al-Mansoori MH, Abdul Rashid HA, Choudhury PK. Low threshold and efficient multi-wavelength Brillouin-erbium fiber laser incorporating a fiber Bragg grating filter with intra-cavity pre-amplified Brillouin pump. Laser Physics Letters. 2009;**6**:54-58

[11] Nasir MNM, Yusoff Z, Al-Mansoori MH, Abdul Rashid HA, Choudhury PK. Widely tunable multi-wavelength Brillouin-erbium fiber laser utilizing low SBS threshold photonic crystal fiber. Optics Express. 2009;**7**:12829-12834

[12] Johari MI, Adamiat A, Shahabuddin NS, Yusoff Z, Abdul Rashid HA, Al-Mansoori MH, Choudhury PK. Ring cavity multiwavelength Brillouin-erbium fiber laser with a partially reflective fiber Bragg grating. Journal of the Optical Society of America B. 2009;**26**:1675-1678

[13] Nasir MNM, Yusoff Z, Al-Mansoori MH, Abdul Rashid HA, Choudhury PK. On the pre-amplified linear cavity multi-wavelength Brillioun-erbium fiber laser with low SBS threshold highly nonlinear photonic crystal fiber. Laser Physics. 2009;**19**:2027-2030

[14] Song KY, Hotate K. 25 GHz bandwidth Brillouin slow light in optical fibers. Optics Letters. 2007;**32**:217-219

[15] Xing L, Zhan L, Luo S, Xia Y. High-power low-noise fiber Brillouin amplifier for tunable slow-light delay buffer. IEEE Journal of Quantum Electronics. 2008;**44**:1133-1138

[16] Desurvire E, Giles CR, Simpson JR, Zyskind JL. Efficient erbium-doped fiber amplifier at a 1.53 μm wavelength with a high output saturation power. Optics Letters. 1989;**14**:1266-1268

[17] Desurvire E, Simpson JR. Amplification of spontaneous emission in erbium-doped single-mode fibers. IEEE Journal of Lightwave Technology. 1989;**7**:835-845

[18] Desurvire E. Erbium-Doped Fiber Amplifiers. New York: Wiley; 1994

[19] Pathmanathan SS, Abdul-Rashid HA, Choudhury PK. An experimental investigation of double-pass erbium-doped optical amplifier with tunable band-pass filter. Asian Journal of Physics. 2008;**17**:241-244

[20] Pathmanathan SS, Abdul-Rashid HA, Choudhury PK. An experimental investigation of Er^{+3}-doped optical amplifiers with very low 1480 nm pump power. International journal of microwave and optical. Technology. 2008;**3**:134-138

[21] Pathmanathan SS, Muhd-Yassin SZ, Abdul-Rashid HA, Choudhury PK. An experimental investigation of the gain spectrum of erbium-doped fiber amplifiers under various system configurations. Optik. 2010;**121**:184-187

[22] Willner AE, Xie Y. Wavelength domain multiplexed (WDM) fiber-optic communication networks. In: Bass M, Van Stryland EW, editors. Fiber Optics Handbook—Fiber, Devices and Systems for Optical Communications. New York: McGraw-Hill; 2002. pp. 13.1-13.31

[23] Tessler N. Lasers based on semiconducting organic materials. Advanced Materials. 1999; **11**:363-370

[24] Turnbull GA, Andrew P, Barnes WL, Samuel IDW. Operating characteristics of a semiconducting polymer laser pumped by a microchip laser. Applied Physics Letters. 2003;**82**:313-315

[25] Lawrence JR, Turnbull GA, Samuel IDW. Broadband optical amplifier based on a conjugated polymer. Applied Physics Letters. 2002;**8**:3036-3038

[26] Lee JH, Chang YM, Han YG, Chung H, Kim SH, Lee SB. A detailed experimental study on single-pump Raman/EDFA hybrid amplifiers: Static, dynamic, and system performance comparison. Journal of Lightwave Technology. 2005;**23**:3484-3493

[27] Tiwari U, Rajan K, Thyagarajan K. Multi-channel gain and noise figure evaluation of Raman/EDFA hybrid amplifiers. Optics Communications. 2008;**281**:1593-1597

[28] Singh S, Kaler RS. Investigation of hybrid optical amplifiers for dense wavelength division multiplexed system with reduced spacing at higher bit rates. Fiber and Integrated Optics. 2012;**31**:208-220

[29] Rocha AM, Nogueria RN. Flexible single pump hybrid fiber amplifier for the S+C bands. Optics Communications. 2014;**320**:105-108

[30] Singh S, Kaler RS. Novel optical flat gain hybrid amplifier for dense wavelength division multiplexed system. IEEE Photonics Technology Letters. 2014;**26**:173-176

[31] Singh S, Kaler RS. Performance optimization of EDFA-Raman hybrid optical amplifier using genetic algorithm. Optics and Laser Technology. 2015;**68**:89-95

Chapter 2

Quantum Dot-Semiconductor Optical Amplifiers (QD-SOA): Dynamics and Applications

Yossef Ben Ezra and Boris I. Lembrikov

Additional information is available at the end of the chapter

http://dx.doi.org/10.5772/intechopen.74655

Abstract

Quantum dot-semiconductor optical amplifiers (QD-SOA) attracted strong interest for applications in optical communications and in all-optical signal processing due to their high operation rate, strong nonlinearity, small gain recovery time of about few picoseconds, broadband gain, low injection current and low noise figure (NF). In this chapter, we present the theoretical investigation of the gain recovery time acceleration in DQ SOA; the specific features of the cross gain modulation (XGM) in QD-SOA; the influence of the optical injection on the dynamics of QD-SOA based on the QD in a well (QDWELL) structure. We describe the following applications of QD-SOA: the all-optical ultra-wideband (UWB) pulse generation based on the Mach-Zehnder interferometer (MZI) with a QD-SOA; the ultra-fast all-optical signal processor based on QD-SOA-MZI; the ultra-fast all-optical memory based on QD-SOA. The contents of the chapter are mainly based on the original results.

Keywords: quantum dot, semiconductor optical amplifier, cross-gain modulation, all-optical processor, all-optical radio signal generation

1. Introduction

Quantum dot-semiconductor optical amplifiers (QD-SOA) are characterized by ultrafast gain recovery time (GRT) of the order of magnitude of several picoseconds, broadband gain, low noise figure (NS), high saturation output power, and high four-wave mixing (FWM) efficiency [1]. QD-SOA can be used as ultra-wideband (UWB) polarization-insensitive high-power amplifiers, high-speed signal regenerators, and wideband wavelength converters (WC) [1–5]. These unique features of QD-SOA are essentially due to the concentration of the injected electrons and holes into nanosized QD [1]. QD is a nanostructure characterized by the electron

IntechOpen

and hole confinement in all three dimensions [2, 6]. QD is a cluster with the dimensions of several nanometers made of a semiconductor material [2]. In a QD charge carriers occupy a limited number of energy levels similarly to an atom, and the density of states is quantized [2]. As a result, QD has freedom of a wavelength choice [1]. A QD contains hundreds of thousands of atoms [2]. Typically, III-V QD are epitaxially grown on a semiconductor substrate [2]. The process of the spontaneous formation of three-dimensional islands during strained layer epitaxial growth is known as the Stranski-Krastanov mechanism [2]. A continuous film of a quantum well (QW) thickness lies underneath QD, and it is called the wetting layer (WL) [2]. The lattice constant of the deposited semiconductor material must be larger than that of the substrate [2]. For instance, an InAs film with the lattice constant of 6.06 Å can be deposited on a GaAs substrate with the lattice constant of 5.64 Å or on an InP substrate with the lattice constant of 5.87 Å [2]. Stranski-Krastanov grown QD typically has a pyramidal shape with a base of 15–20 nm and a height of about 5 nm; the QD density per unit area is between 10^9 and 10^{12} cm^{-2} [1, 2]. The methods of the QD energy levels and density of states evaluation are presented in Ref. [6].

The theory of the optical signal amplification and processing based on the density matrix equations for the electron-light interaction and the optical pulse propagation equations has been developed [7]. The QD spatial localization, the inhomogeneous spectral broadening caused by the QD size, shape, composition, and stain distribution, the carrier capture from WL, the carrier emission to WL, intradot population relaxation, and homogeneous spectral broadening have been taken into account, and the nonlinear optical response has been also investigated [7]. The phenomenological approach to the QD-SOA theory is based on the system of rate equations for photons and charge carriers in QD [2, 5, 8]. In such a case, the QD is considered as a three-state system including the ground state (GS), the excited state (ES) and WL [2, 5, 8]. The electron dynamics in QD is assumed to be slower than the hole dynamics, and for this reason, only the rate equations for electron populations of GS, ES and WL are included in the dynamic model [2, 5, 8]. Using this model, we investigated theoretically acceleration of gain recovery and dynamics of electrons in QD-SOA [9, 10]. We have shown that the QD-SOA GRT may be substantially decreased, and the patterning effect is reduced by increasing the optical pump power, while the chirp in QD-SOA is about one order of magnitude lower than the one in the bulk SOA [9, 10]. We studied theoretically the cross-gain modulation (XGM) process in QD-SOA taking into account the QD-SOA inhomogeneous spectral broadening [11]. We have shown that XGM in QD-SOA occurs at larger detuning between the pump and signal light waves as compared to the bulk SOA, the asymmetric chirp may be diminished by the bias current increase, and XGM process slows down in the nonlinear regime [11].

Recently, QD-SOA and lasers based on a novel quantum dot-in-a-well (QDWELL) structure have been proposed where the self-assembled QD has been grown into QW with the discrete energy levels and the two-dimensional (2D) electron gas instead of ordinary QD laser and SOA with the continuous carrier energy in WL [12, 13]. The operation of QD-SOA based on a QDWELL structure (QDWELL SOA) has been investigated both theoretically and experimentally [12–16]. The complicated dynamics of QDWELL SOA is described by the system of the rate equations for the electrons and holes in QD and QW including the strongly nonlinear electron and hole scattering rates for the carrier scattering between QD and QW [12, 17]. The operation rate of QDWELL SOA is limited by the desynchronized recovery dynamics of electrons and holes caused by the different microscopic scattering rates [15]. We have shown theoretically that the electron and hole dynamics in QDWELL lasers and SOA can be synchronized by a sufficiently strong optical injection and consequently the QDWELL lasers and SOA performance including the operation rate can be significantly improved [18–22].

Optical signal processing is based on the linear and nonlinear optical techniques for the digital, analogous and quantum information [23]. It is a promising technology for increasing the processing speed of devices, the capacity of optical links, and reducing of energy consumption [23]. In particular, QD-SOA are excellent candidates for high-speed data and telecommunication applications due to their ultrafast gain dynamics and pattern effect-free amplification [15]. We proposed the following novel applications of QD-SOA in optical communications:

1. a novel all-optical method of the impulse radio ultra-wideband (IR-UWB) pulse generation based in an integrated Mach-Zehnder interferometer (MZI) with QD-SOA as an active element inserted into one arm of the integrated MZI [24–26];
2. an ultra-fast all-optical processor based on QD-SOA [27, 28]; and
3. an ultra-fast all-optical memory based on QD-SOA [29, 30].

The detailed results of the numerical simulations are presented in Refs. [9–11, 18–22, 24–30]. In this work, we discuss the theoretical models of QD-SOA, QDWELL SOA, and some devices for the all-optical signal processing, summarize the results obtained and present the necessary numerical estimations. The chapter is organized as follows. In Section 2, we discuss the dynamics of the gain recovery and XGM processes in QD-SOA. In Section 3, we consider the influence of the optical injection on the QDWELL SOA performance. The applications of QD-SOA in optical signal processing are discussed in Section 4. The conclusions are presented in Section 5.

2. Specific features of the QD-SOA dynamics

2.1. Theoretical model of QD-SOA

In this section, we theoretically investigate the gain recovery process and XGM in QD-SOA. The analysis is based on the simultaneous solution of the rate equations for the electron density per unit volume in WL N_w, electron occupation probabilities f and h of GS and ES, respectively, and the equations for pump and signal wave photon densities $S_{p,s}$ and phases $\theta_{p,s}$ [9–11]. The energy band structure of QD-SOA is shown in **Figure 1**.

The carrier transitions between WL, ES and GS are characterized by different relaxation times. The fast transition processes between WL and ES, and between ES and GS are described by the relaxation times $\tau_{w2}, \tau_{21}, \tau_{12} \sim \left(10^{-12} - 10^{-11}\right)s$ [5, 8]. The transitions from ES to WL are characterized by the much larger carrier escape time $\tau_{2w} \sim 10^{-9}s$ [5]. The rate equations for the spatially averaged over the QD-SOA length L values of N_w, f, h have the form [5, 8–11]:

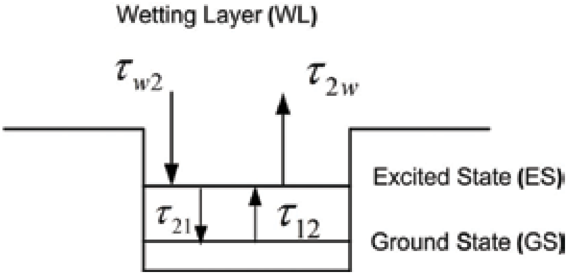

Figure 1. The QD-SOA energy band structure.

$$\frac{\partial N_w}{\partial t} = \frac{J}{eL_w} - \frac{N_w(1-h)}{\tau_{w2}} + \frac{N_w h}{\tau_{2w}} - \frac{N_w}{\tau_{wR}} \tag{1}$$

$$\frac{\partial h}{\partial t} = \frac{N_w L_w(1-h)}{N_Q \tau_{w2}} - \frac{N_w L_w h}{N_Q \tau_{2w}} - \frac{(1-f)h}{\tau_{21}} + \frac{f(1-h)}{\tau_{12}} \tag{2}$$

$$\begin{aligned}\frac{\partial f}{\partial t} = &\frac{(1-f)h}{\tau_{21}} - \frac{f(1-h)}{\tau_{12}} - \frac{f^2}{\tau_{1R}} - \frac{g_p Lc}{N_Q\sqrt{\varepsilon_r}}(2f-1)S_p \\ &- \frac{g_s Lc}{N_Q\sqrt{\varepsilon_r}}(2f-1)S_s\end{aligned} \tag{3}$$

The equations for $S_{p,s}$ and $\theta_{p,s}$ are given by [8–11, 31]:

$$\frac{\partial S_{p,s}(z,\tau)}{\partial z} = \left(g_{p,s} - \alpha_{\text{int}}\right) S_{p,s}(z,\tau) \tag{4}$$

$$\frac{\partial \theta_{p,s}}{\partial z} = -\frac{1}{2}\alpha g_{p,s} \tag{5}$$

Here, J is the bias current density, N_Q is the QD density per unit area, L_w is the effective thickness of the active layer, τ_{wR}, τ_{1R} are the spontaneous lifetime in WL and QD, respectively, c is the free space light velocity, e is the electron charge, ε_r is the active layer permittivity, α_{int} is the absorption coefficient of the QD-SOA material, α is the linewidth enhancement factor (LEF), $\tau = t \mp z/v_g$ is the temporal variable related to the wave propagation in a retarded frame, $v_g = c/n_g$ is the light group velocity, n_g is the group refraction index, $S_{p,s} = P_{p,s}/\left(\hbar\omega_{p,s}\left(v_g\right)_{p,s} A_{eff}\right)$, $P_{p,s}$ are the pump and signal wave power, $\hbar = h/2\pi$, h is the Planck constant, A_{eff} is the QD-SOA effective cross-section, $g_{p,s}$ are the pump and signal wave modal gains. They are given by [31]:

$$g_{p,s}(\omega_0) = \frac{2\Gamma N_Q}{a}\int d\omega F(\omega)\sigma(\omega_0)(2f-1) \tag{6}$$

where Γ is the confinement factor which is the same for both light waves, a is the mean size of QD, factor 2 takes into account the spin degeneracy of the QD levels, $F(\omega)$ is the Gaussian distribution of the transition frequency. It is related to the inhomogeneous broadening, and it has the form [31]:

$$F(\omega) = \frac{1}{\Delta\omega\sqrt{\pi}} \exp\left[-\frac{(\omega - \overline{\omega})^2}{(\Delta\omega)^2} \right] \tag{7}$$

where $\overline{\omega}$ is the average transition frequency, $\Delta\omega$ is related to the inhomogeneous linewidth $\gamma_{in\text{hom}}$ as follows: $\gamma_{in\text{hom}} = 2\sqrt{\ln 2}\Delta\omega$ [31]. Typically, the inhomogeneous broadening of QD lasers and SOA σ_E is about 30–40 meV and the homogeneous broadening is about 15–20 meV at room temperature [3]. The QD device inhomogeneous broadening has both advantages and disadvantages for different applications. The generation, propagation, and amplification of ultrafast pulses can be realized due to the wide bandwidth [2]. On the other hand, the inhomogeneous broadening caused by the QD size fluctuations increases the transparency current and reduces the modal and differential gain [2]. The cross-section $\sigma(\omega_0)$ of interaction of photons of frequency ω_0 with the carriers in QD at the transition frequency ω is given by [31]:

$$\sigma(\omega_0) = \sigma_{res} \frac{1}{\left[1 + (\omega - \omega_0)^2 T_2^2 \right]} \tag{8}$$

The cross-section $\sigma(\omega_0)$ at the frequency $\omega = \omega_0$ has its maximum value of the resonant cross section σ_{res} which has the form [31]:

$$\sigma_{res} = \frac{\mu^2 \omega_0 T_2}{c n_g \varepsilon_0 \hbar} \tag{9}$$

where μ is the dipole moment of the optical transition, $T_2 = 2\gamma_{\text{hom}}^{-1}$ is the dephasing time related to the homogeneous linewidth γ_{hom}, ε_0 is the free space permittivity.

In our analysis of the QD-SOA dynamics, we are interested in the temporal dependence of the power $P_{p,s}$ and phase $\theta_{p,s}$ of the lightwave pulses with the bit rates $B \leq 40\ Gb/s$ at the output of the QD-SOA [9–11]. In such a case, the lightwave radiation is filling the QD-SOA active region of the length $L \sim 1\ mm$ and interacts with all QD. For this reason, the light intensity can be averaged over the QD-SOA length L [9–11]. Integrating Eq. (4) over z and averaging the result over the QD-SOA active region length L, we obtain [11]:

$$S_{p,s}(\tau) = \frac{1}{L} \left(S_{p,s}(\tau) \right)_{in} \int_0^L dz \exp\left[\int_0^z \left(g_{p,s} - \alpha_{\text{int}} \right) dz' \right] \tag{10}$$

Integrating Eq. (5), we obtain the phases $\theta_{p,s}$ [11]:

$$\theta_{p,s} = -\frac{\alpha}{2} \int_0^L g_{p,s} dz \tag{11}$$

The chirp $\delta\nu_{p,s}$ is given by [11]:

$$\delta\nu_{p,s} = -\frac{1}{2\pi}\frac{\partial\theta_{p,s}(\tau)}{\partial\tau} \tag{12}$$

System of Eqs. (1)–(3) with the average pump and signal photon densities (10) describes the gain recovery and XGM processes in QD-SOA. These equations are strongly nonlinear, and for this reason, they are extremely complicated. Their analytical solution in a closed form is hardly possible. We solved the system of Eqs. (1)–(5) numerically for the following typical values of the material parameters: $L = 2\ mm$, $L_w = 0.1 - 0.2\ \mu m$, the QD-SOA width $W = 10\ \mu m$, $\Gamma \sim 3 \times 10^{-2}$, $\tau_{w2} = 3\,ps$, $\tau_{21} = 0.16\,ps$, $\tau_{12} = 1.2\,ps$, $\tau_{1R} = 0.4\,ns$, $\tau_{2w} = \tau_{wR} = 1\,ns$, $N_Q = 5\times 10^{10}\ cm^{-2}$, $g_{\max} = 11.5\ cm^{-1}$, $\sigma_E = 30\,meV$, $\tau_{12} = \tau_{21}\rho\exp(\Delta E_{21}/k_B T)$, $\rho = 1$, $\alpha_{\text{int}} = 3\ cm^{-1}$, $\alpha = 0.1$, the energy separation between ES and GS $\Delta E_{21} = 30\ meV$, the temperature $T = 300\ K$, k_B is the Boltzmann constant [5, 8, 31, 32]. The simulation results for the case of the QD-SOA gain recovery process [9, 10] and XGM in QD-SOA [11] are discussed in subsections 2.2 and 2.3, respectively.

2.2. Theoretical analysis of the gain recovery process in QD-SOA

The QD-SOA performance is mainly determined by their GRT and the magnitude of the chirp $\delta\nu_{p,s}$. GRT is limited by the carrier lifetime which can be decreased by the increase of the applied bias current and the light intensity in the active layer of SOA [9, 10]. Consider first the two lightwaves with the same wavelength $\lambda = 1550\,nm$ inserted into the QD-SOA: a continuous wave (CW) probe lightwave and a pump lightwave representing a Gaussian pulse with a full-width of half maximum (FWHM) of 150 fs [9]. In such a case, the numerical simulation results for the probe power $P_p = 10\mu W$ and the bias current of 20 mA show that the 10–90% GRT is about 378 fs, which is comparable to the experimental results for SOA based on self-assembled InAs-InGaAS QD [2, 33, 34]. It is much smaller than the GRT of about 100 ps for the QW SOA and several hundred ps for the bulk SOA [2, 35]. The low GRT in QD-SOA is related to the small electron transition time from ES to GS $\tau_{21} \sim 10^{-1}\ ps$. The GRT decreases with the increase of the input probe wave power $P_{p,in}$ due to the high stimulated transition rates [9]. The chirp (12) increases with the increase of $P_{p,in}$ due to the increase of the photo carrier density, which results in a larger change of the QD-SOA refractive index Δn [9].

Consider now the influence of the bias current and the CW probe optical wave intensity on the QD-SOA dynamics in two cases of the optical signal wave with the power of $P_s = 1\ mW$, wavelength $\lambda = 1550\,nm$ and a bit rate $B = 40\ Gb/s$: (1) the pseudorandom bit sequence (PRBS) of the length $\left(2^{11} - 1\right)$; (2) the Gaussian pulse with FWHM $T_0 = 15\,ps$ [10].

We start with the analysis of the QD-SOA dynamics in the absence of the probe optical wave. In the PRBS case, the simulation results show that at a low bias current of an order of magnitude of $I = 10\ mA$ close to the transparency value of about 6 mA, the patterning effect is strongly pronounced. In such a case, the QD-SOA does not respond adequately to the fast changes of the input optical signal. The electron exchange processes between WL and ES are substantially slower than the transitions between ES and GS. As a result, only the GS electron occupation probability $f(t)$ follows the PRBS. The rise time of the WL electron density $N_w(t)$ coincides with time duration of long pulses $\Delta t_r \sim 100\, ps$ since it is determined by $\tau_{2w} = 1\ ns$. On the contrary, the decrease of $N_w(t)$ determined by the faster electron transitions from WL to ES is characterized by the short characteristic time $\Delta t_d \sim \tau_{w2} \sim 10^{-12}\ s$ [10]. The QD-SOA dynamics for the Gaussian pulse at the low bias current is similar since the recovery times for the dynamic variables are quite different: it is about 50 ps for $N_w(t)$, 25 ps for $h(t)$, and 17 ps for $f(t)$ [10]. The pulse broadening for each one of the dynamic variables is different which results in the patterning effect. For the bias current $I = 30\ mA$ which is much larger than the transparency current, the strong injection of the charge carriers increases the ES population and the number of fast transitions from ES to GS with a characteristic timescale of $\tau_{12} \sim 1\ ps$. These fast transitions become dominant. However, the WL population dynamics determined by slow processes does not change significantly. For this reason, the patterning effect decreases for large bias current, but it still exists [10]. The numerical simulation results show that in the absence of the optical probe wave the increase of the bias current does not improve significantly the QD-SOA performance both for the Gaussian pulse and for the PRBS signal [10]. Consider now the influence of the counter-propagating strong probe wave with the power $P_p \sim 1\ mW$ and wavelength $\lambda = 1535\ nm$ on the QD-SOA carrier dynamics [10]. This optical injection gives rise to the stimulated emission between the GS and the valence band. Consequently, the transitions from ES to GS accelerate, the ES population is rapidly decreasing, and the fast transitions from WL to ES characterized by $\tau_{w2} = 3\ ps$ become dominant. The numerical simulation results show that in such a case, the changes of $N_w(t), h(t), f(t)$ do not exceed 10%, GRT is about 15 ps, the pulse broadening and the delay time are approximately the same for all dynamic variables $N_w(t), h(t), f(t)$, and the patterning effect completely vanishes [10]. At probe wave, power of several milliwatts and FWHM of 150 fs, the GRT reduces to 0.2 ps since the GRT lower limit is determined by the QD-SOA lowest transition time between ES and GS $\tau_{21} = 0.16\, ps$. GRT of 39 ps in the bulk SOA has been demonstrated experimentally for the optical injection power of 100 mW, or by the bias currents of 150–450 mA without optical injection [35].

2.3. Peculiarities of XGM in QD-SOA

Consider now the peculiarities of XGM in QD-SOA caused by the gain inhomogeneous broadening which is due to the variation of QD size, shape, and local strain [11]. XGM is an essentially nonlinear process in SOA caused by the carrier density change influence on the input signal waves [36]. Typically, XGM in SOA may realize the wavelength conversion [36]. The XGM process in QD-SOA involves three types of transitions: (1) fast transitions between ES and GS characterized by $\tau_{21}, \tau_{12} \sim (0.1 - 1)\ ps$; (2) intermediate timescale transitions from WL to ES with the relaxation time τ_{w2} of several picoseconds; (3) slow escape transitions from ES to WL determined by the spontaneous recombination time in WL $\tau_{wR} = \tau_{2w} \sim 1\ ns$. We investigated theoretically the wavelength conversion in QD-SOA for the CW pump wave with the power $P_p = 0.1\ mW$ and the wavelength $\lambda_p = 1530\ nm$ and the input PRBS nonreturn-to-zero (NRZ) signal of the length $2^{11} - 1$ with the wavelength $\lambda_p = 1550\ nm$. We solved numerically system of Eqs. (1)–(3) with the modal gains $g_{p,s}$ (6), the average photon densities $S_{p,s}$ (10), phases $\theta_{p,s}$ (11) and the typical values of the material parameters mentioned in subsection 2.1 [11]. For the sake of definiteness, we consider the counter-propagating signal and pumping waves [11]. A schematic diagram of the traveling wave (TW) QD-SOA is shown in **Figure 2**.

We used the bias current values $I = 10\ mA$, $I = 30\ mA$, and the bit rates of 10, 40 Gb/s [11]. We start with the analysis of the bias current, the optical power, and the signal bit rate influence on the XGM in QD-SOA. The numerical simulation results show that at the low input signal power level $P_s = 0.1\ mW$ and $I = 30\ mA$, QD-SOA operates close to the linear regime where $f \approx 1$ and the variations of the ES and GS populations of about 10–20% are relatively small [11]. However, in the linear regime, the population exchange between ES and GS is sufficient for the required level of XGM. In the nonlinear regime corresponding to the strong enough signal wave power $P_s = 10\ mW$, an additional number of electrons in GS is necessary for maintaining the gain level. As a result, the electron concentration N_w in WL reduces to about 30% of its maximum value; WL refilling is necessary, and the slow transitions between ES and WL become essential. The XGM process is slowing down [11].

Consider now the temporal dependence of the input signal power P_s and the output power P_s^{out}. The patterning effect is strongly pronounced for the bit rate of 10 Gb/s and a low bias current $I = 10\ mA$, and it becomes even stronger for the bit rate of 40 Gb/s. The patterning effect can be reduced by the increase of the bias current for comparatively low bit rates. Indeed, for the increased bias current $I = 30\ mA$ and for the bit rate of 10 Gb/s, the patterning effect practically vanishes. However, at higher bit rate of 40 Gb/s, the increase of the bias current does not reduce the patterning effect because the QD-SOA operation rate is still limited

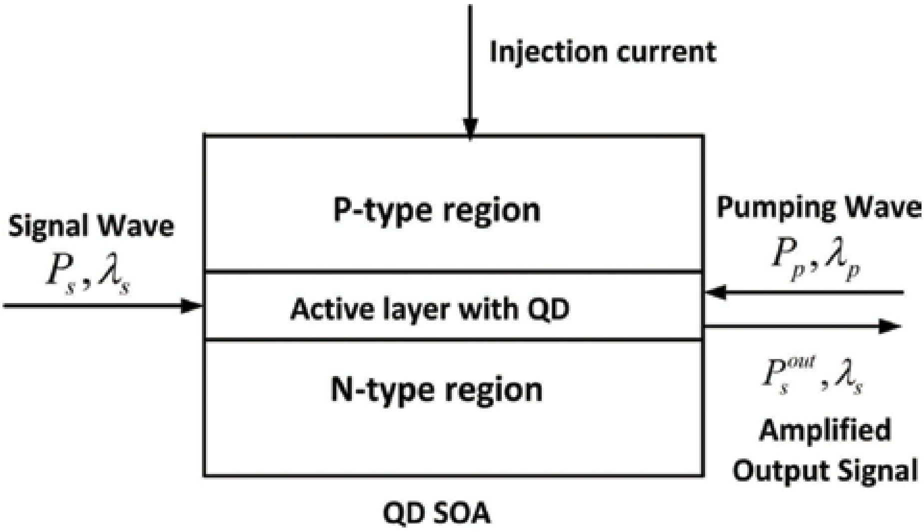

Figure 2. Schematic diagram of the traveling wave (TW) QD-SOA with the counter-propagating signal and pumping optical waves.

by the comparatively slow processes in WL. The chirp $\delta\nu_{p,s}$ evaluated according to Eq. (12) increases substantially up to 20 GHz for the bias current $I = 30\ mA$ and the bit rate of 40 Gb/s, and it is strongly asymmetric with the magnitude of the negative chirp substantially larger than the positive one [11].

Consider the possibility of XGM in QD-SOA between the waves with the detuning larger than the QD-SOA homogeneous broadening. In such a case, we divide QD into groups with different resonant frequencies caused by the inhomogeneous broadening. This time, we solve Eqs. (1)–(3) numerically for the QD group 1 and 2 with a detuning substantially larger than the QD-SOA homogeneous broadening [11]. The numerical simulation results show that the strong interaction through WL for these QD groups occurs for a comparatively low bit rate of 10 Gb/s and significantly diminishes at 40 Gb/s. At the large bit rates, the ES and GS populations of the first QD group do not follow the changes of the ES and GS populations of the second QD group, the WL electron concentration is slightly varying, and the XGM effect vanishes. The output optical power P_{out} and the output signal chirp correlate with the input power for the bit rate of 10 Gb/s, but they do not correlate anymore for the bit rate of 40 Gb/s.

The comparison of the performance of bulk, multiquantum well (MQW) and QD-SOA shows that XGM can be realized in the bulk SOA for the bias current of $(160 - 200)\ mA$, in MQW SOA for the bias current of $(30 - 150)\ mA$, while in QD-SOA, similar results for XGM can be achieved for the bias current of $30\ mA$ (see [11] and references therein). The bulk and MQW SOA performance significantly deteriorates at the bit rates of about 10 Gb/s because of the large radiative relaxation time. On the ontrary, the pattern-effect-free XGM in QD-SOA is possible at 10 Gb/s due to the small relaxation time $\tau_{21} \sim 10^{-1}\ ps$: $\tau_{21}^{-1} \gg B = 10\ Gb/s$. XGM in the columnar QD (CQD) SOA at the wavelength of 1550 nm has been demonstrated experimentally [37]. CQD-SOA based on near isotropically shaped CQD make possible polarization-independent WC [37]. It has been shown in particular that the bit rate of 40 Gb/s is cut-off transmission capacity for the distortion-free XGM wavelength conversion [37].

3. The influence of the optical injection on the QDWELL SOA performance

In this section, we consider XGM in the TW QDWELL SOA mainly following references [20–22].

The block diagram of the TW QDWELL SOA is presented in **Figure 3**. Typically, a QDWELL active region structure consists of 10–15 InGaAs quantum well (QW) layers with a height of about 4 nm containing embedded InAs QD with a size of approximately 4 nm x 18 nm x 18 nm [12]. The layers of InGaAs/InAS QD are separated by 33 nm GaAS spacers providing the strain relaxation between successive QD layers [13]. The electric bias current is injected into the QW layers which represent the reservoir of the 2D carrier gas unlike the WL with the continuous energy of carriers in ordinary QD-SOA [12]. The ridge width and the waveguide length are $2 - 4\ \mu m$ and $1 - 2\ mm$, respectively [13]. The co-propagating optical signal and pumping waves with the power $P_{p,s}$ and wavelength $\lambda_{p,s}$ are fed into the QDWELL SOA. GS is in the

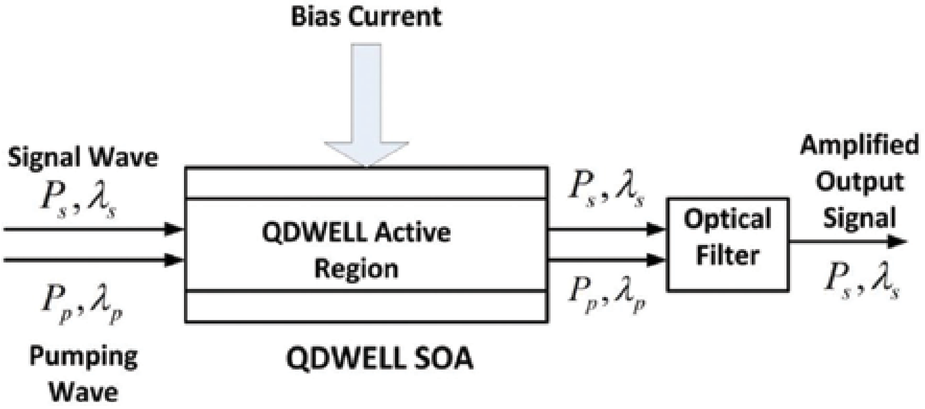

Figure 3. The block diagram of the TW QDWELL SOA with the co-propagating optical signal wave (P_s, λ_s) and pumping wave (P_p, λ_p).

resonance with the signal wave to be amplified [13]. The GS is filled by the carriers from ES and QW carrier reservoir [13]. The fast transitions between ES and GS provide the ultrafast GS recovery time of about $130\,fs$, the scattering time from the QW into the QD is about $1-2\,ps$, and the time of slow recovery of the QW reservoir after depletion is about $100-150\,ps$ [13]. As a result, the maximum frequency bandwidth of the QW carrier reservoir is about $7-10\,GHz$ while the fast QD dynamics bandwidth is beyond $100\,GHz$ [13]. The QDWELL SOA dynamics is described by the system of Lüdge-Schöll (LS) rate equations for the electron and hole occupation probabilities $\rho_{e,h}$ in the confined GS of QD and for the electron and hole densities per unit area $w_{e,h}$ in QW [12, 17]. The energy levels of the QDWELL structure are shown in **Figure 4**.

For the moderate bias currents and comparatively slow processes, the dynamics of the ES-GS transitions can be adiabatically eliminated [12]. Then, the LS rate equations have the form [12, 17]:

$$\begin{aligned}\frac{\partial \rho_{e,h}}{\partial t} &= -W_{ind}A\left(\rho_e + \rho_h - 1\right)\left(n_{ph,p} + n_{ph,s}\right) - R_{sp}\left(\rho_e, \rho_h\right) \\ &+ S^{in}_{e,h}(w_e, w_h)\left(1 - \rho_{e,h}\right) - S^{out}_{e,h}(w_e, w_h)\rho_{e,h}\end{aligned} \tag{13}$$

$$\frac{\partial w_{e,h}}{\partial t} = \frac{J}{e} - 2N_{QD}\left[S^{in}_{e,h}(w_e, w_h)\left(1 - \rho_{e,h}\right) - S^{out}_{e,h}(w_e, w_h)\rho_{e,h}\right] - \tilde{R}_{sp} \tag{14}$$

where W_{ind} is the Einstein coefficient for the induced emission, A is the in-plane area of QW, N_{QD} is the total QD density per unit area in all QW layers, $S^{in}_{e,h}(w_e, w_h)$, $S^{out}_{e,h}(w_e, w_h)$ are the strongly nonlinear electron and hole scattering rates for the scattering in and out of QD, respectively, $R_{sp}\left(\rho_e, \rho_h\right) = W_{sp}\rho_e\rho_h$, $\tilde{R}_{sp}$ are the spontaneous emission rates in QD and QW, respectively, W_{sp} is the Einstein coefficient for the spontaneous emission. The complicated analytical expressions of $S^{in}_{e,h}(w_e, w_h)$, $S^{out}_{e,h}(w_e, w_h)$ can be found in Ref. [17]. The carrier lifetimes $\tau_{e,h}$ determined by the Coulomb scattering between QD and QW are defined by these

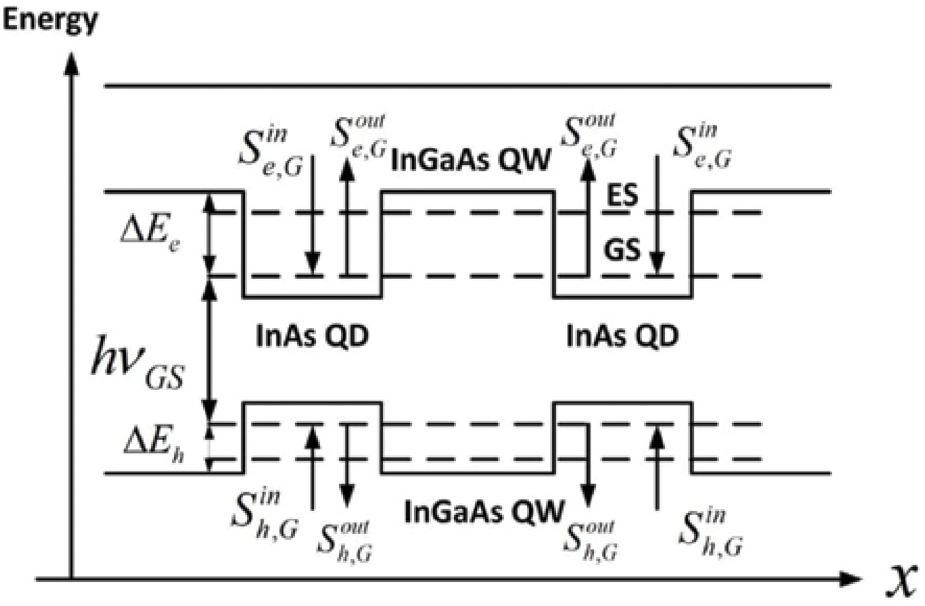

Figure 4. Energy diagram of the QDWELL structure. $\Delta E_{e,h}$ determines the position of the electron and hole GS in QD.

scattering rates as follows [17]: $\tau_e = \left(S_e^{in} + S_e^{out}\right)^{-1}$ and $\tau_h = \left(S_h^{in} + S_h^{out}\right)^{-1}$. Comparison of Eqs. (1), (2) and (13), (14) clearly shows that the QDWELL SOA dynamics is much more complicated than the dynamics of the ordinary QD-SOA. In the case of the QDWELL lasers and SOA, there exist different timescales for electrons and holes in QD and QW reservoir, and for this reason, the carrier dynamics is desynchronized limiting the QDWELL SOA operation rate [12, 38]. The strong optical injection can synchronize the QDWELL laser carrier dynamics in QDWELL lasers and improve their performance [18]. Similarly, in the case of the XGM in the QDWELL SOA, the pumping and signal optical waves play a role of the optical injection according to Eq. (13) and synchronize the carrier dynamics improving QDWELL SOA performance [20–22].

The equations for the pumping and signal wave photon density per unit area $n_{ph,p,s}$ and phases $\Phi_{p,s}$ have the form [20–22, 31]:

$$\frac{\partial n_{ph,p,s}(z,\tau)}{\partial z} = \left(g_{\text{mod}p,s} - \alpha_{\text{int}}\right) n_{ph,p,s}(z,\tau) \tag{15}$$

$$\frac{\partial \Phi_{p,s}}{\partial z} = -\frac{\alpha}{2} g_{\text{modp},\text{s}} \tag{16}$$

The photon density per unit area $n_{ph,p,s}$ and the photon density $S_{p,s}$ per unit volume are related as follows: $S_{p,s} = \partial n_{ph,p,s}/\partial z$, and $n_{ph,p,s}(0,\tau) = S_{p,s}/\left(g_{\text{mod}p,s} - 2\kappa\right)$ [20]. The QDWELL SOA modal gain $g_{\text{mod}p,s}$ has the form [20]:

$$g_{\text{mod}p,s}(\omega_0) = \frac{2\Gamma N_{QD}}{a} \int d\omega F(\omega)\sigma(\omega_0)\left(\rho_e + \rho_h - 1\right) \tag{17}$$

where $\Gamma = a_L h_{QW}/h_w$ is the confinement factor, a_L is the number of QW layers, $h_{QW} \approx a$ is the height of the QW layer with QD, and h_w is the height of the waveguide. The term $\left(\rho_e + \rho_h - 1\right)$ in Eqs. (13) and (17) describes the electron and hole population inversion in the two-level system of QD. Comparison of Eqs. (13), (15) and (17) shows that the population inversion $\left(\rho_e + \rho_h - 1\right) > 0$ is the necessary condition of the amplification in the QDWELL SOA. Similarly to the previous case of the QD-SOA, we evaluate the spatially averaged over the QDWELL SOA length L photon density per unit area $n_{php,s}(\tau)$ [20]:

$$n_{php,s}(\tau) = \frac{1}{L}\left(n_{php,s}(\tau)\right)_{in} \int_0^L dz \exp\left[\int_0^z \left(g_{\text{mod}p,s} - \alpha_{\text{int}}\right) dz'\right] \tag{18}$$

The phases $\Phi_{p,s}$ and the chirp $\Delta\nu_{chirp}^{p,s}$ are given by [20]:

$$\Phi_{p,s} = -\frac{\alpha}{2}\int_0^L g_{\text{mod}p,s} dz; \Delta\nu_{chirp}^{p,s} = -\frac{1}{2\pi}\frac{\partial\Phi_{p,s}}{\partial t} \tag{19}$$

The relation between the pumping and signal wave optical power $P_{opt,p,s}(z,\tau)$ and instantaneous pumping and signal photon densities per unit area $n_{ph,p,s}$ can be obtained by using the expressions of $S_{p,s}$. It has the form [20]:

$$\frac{\partial n_{ph,p,s}}{\partial z} = \frac{P_{opt,p,s}(z,\tau)\sqrt{\varepsilon_r}}{2\hbar\omega c A_W} \tag{20}$$

where A_W is the optical waveguide cross-section area.

We solved numerically the system of Eqs. (13)–(16) for the typical values of the material parameters $W_{sp} = 0.7\ ns^{-1}$, $W_{ind} = 0.11\ \mu s^{-1}$, $L = 1\ mm$, $\alpha_{\text{int}} = 12.56\ cm^{-1}$, $A = 4 \times 10^{-5}\ cm^2$, the bias current density corresponding to the transparency $J_0 = 6.72 \times 10^5\ Am^{-2}$, $a_L = 15$, $N_{QD} = 10^{11}\ cm^{-2}$, the central pumping and signal wavelengths are $\lambda_p = 1.25\ \mu m$ and $\lambda_s = 1.35\ \mu m$, respectively [17]. In our case, the detuning between the pumping and signal waves $\hbar\left(\omega_p - \omega_s\right) \approx 73.5\ meV > \hbar\gamma_{inhom}, \hbar\gamma_{\text{hom}}$, and we have taken into account the modal gain inhomogeneous broadening according to Eqs. (17) and (7)–(9). LEF has been chosen to be $\alpha = 10$, which is feasible for QD-SOA [2].

We evaluated the QDWELL SOA gain for $\lambda_s = 1.35\ \mu m$ and for the optical pumping power $P_p = 2\ mW, 5\ mW, 10\ mW$ [20]. The numerical simulation results show that the gain magnitude reaches the level of 20 dB and then decreases with the further increase of the pumping power due to XGM and gain saturation. The QDWELL SOA bandwidth is strongly enhanced due to the fast stimulated transitions in QD caused by the strong optical pumping. The bias current density slightly influences the gain because of the weak connection between the QW carrier reservoir and QD in the XGM process.

Consider now the synchronization of the carrier dynamics and gain recovery process for the super-Gaussian pulse of the signal wave $\sim \exp\left(-t^4/T_0^4\right)$, $T_0 = 20\, ps$ and the bias current density $J = 2J_0$ [20]. For the small pumping power $P_p = 1\mu W \ll P_s = 1\, mW$, the electron and hole dynamics in QD is desynchronized, and the temporal dependences of $\rho_{e,h}$ are essentially different since their dynamics is determined by the different QD carrier-carrier scattering rates $S_{e,h}^{in}(w_e, w_h)$, $S_{e,h}^{out}(w_e, w_h)$. These nonlinear scattering rates strongly depend on the bias current providing the carriers into the QW reservoir. A comparatively large time interval is necessary for the filling of the QD levels from the QW reservoir. The numerical simulation results show that the QW carrier densities are slightly varying with the deviation of about 1% due to the bias current, while the QD carrier occupation probabilities are approximately equal and varying by 10–20% [20]. The situation changes when the pumping and signal powers are equal and strong enough: $P_p = P_s = 1\, mW$. In such a case, GRT is approximately two times smaller than in the weak pumping case. The behavior of the QD electron and hole occupation probabilities $\rho_{e,h}$ is determined by the sign of the right-hand side (RHS) of Eq. (13). In the case of the strong pumping power P_p, the first term in the RHS of Eq. (13) is dominant providing the fast stimulated transitions in QD. The QD carrier dynamics in such a case synchronized due to the strong optical pumping. The population inversion term $\left(\rho_e + \rho_h - 1\right)$ reaches its minimum value due to the fast recombination process, and the the positive definite term $S_{e,h}^{in}(w_e, w_h)\left(1 - \rho_{e,h}\right) > 0$ in the RHS of Eq. (13) becomes dominant. Then, the QD electron and hole occupation probabilities $\rho_{e,h}$ rapidly increase again. The GRT decreases due to the strong optical pumping.

Consider now the QDWELL SOA large signal response for the electrical PRBS signal with the length of $\left(2^{11} - 1\right)$, repetition frequency of 140 Gb/s, a signal wave power $P_s = 1\, mW$, and the bias current density of $2J_0$ [20]. The numerical simulation results show that for the small optical pumping power $P_p = 1\, \mu W$, the QD and QW carrier dynamics is desynchronized and determined by the scattering rates $S_{e,h}^{in}(w_e, w_h)$, $S_{e,h}^{out}(w_e, w_h)$. The QD levels cannot be filled completely by the capture of carriers from the QW reservoir since the scattering rates $S_{e,h}^{in}(w_e, w_h)$, $S_{e,h}^{out}(w_e, w_h)$ are different for electrons and holes, and the corresponding lifetimes $\tau_e = \left(S_e^{in} + S_e^{out}\right)^{-1}$ and $\tau_h = \left(S_h^{in} + S_h^{out}\right)^{-1}$ are large. As a result, QDWELL SOA exhibits the pattern effect. The chirp $\left|\Delta \nu_{chirp}^s\right| \approx 80\, GHz$ is large and asymmetric.

The QW and QD carrier behavior changes drastically in the case of the strong optical pumping $P_p = P_s = 1\, mW$ even at the same bias current density of $2J_0$. The QD carrier dynamics now is synchronized, the QD electron and hole occupation probabilities $\rho_{e,h}$ remain practically constant at the level of $\rho_e = (0.635 - 0.638)$ and $\rho_h = (0.425 - 0.4285)$ while the positive population inversion $\left(\rho_e + \rho_h - 1\right) > 0$ is slightly varying. The QW carrier dynamics is also synchronized, and the relative variations of the QW carrier densities $w_{e,h}$ are about 10^{-4} [20]. The oscillation period is determined by the optically enhanced GRT. The pattern effect vanishes, and the chirp $\left|\Delta \nu_{chirp}^s\right| \approx 5\, GHz$ sharply reduces and becomes symmetric [20].

Consider now the influence of the optical pumping on the XGM and cross-phase modulation (XPM) of the co-propagating pumping and signal optical waves in QDWELL SOA [20–22]. We suppose that these waves have the same polarization corresponding to a maximum value of the gain since the gain in QDWELL SOA has strong polarization dependence [4]. We investigated the XGM in the in QDWELL SOA both in the pulse regime and in the PRBS regime.

In the pulse regime, for the pulse duration of 5 ps, pump wave power $P_p = 0.4\ \mu W$, the signal wave power $P_s = 1\ mW$ and the bias current density $J = 3J_0$ the QD carrier dynamics is synchronized, and the XGM efficiency is high since the pump wave optical power is depleted almost down to zero [21]. For the pulse duration of 3 ps and the signal wave power increase up to $P_s = 10\ mW$, the QW carrier is also synchronized because the fast light stimulated transitions in QD are dominant. The GRT decreases, the XGM efficiency remains high, the fall time of the signal pulse significantly decreases from about 0.05 ns for $P_s = 1\ mW$ to about 0.01 ns for $P_s = 10\ mW$ while the rise and fall time of the weak pumping pulse do not change [21]. The optical injection enhances the QDWELL SOA bandwidth facilitating the ultra-fast pulse propagation, decreases the spectral broadening, and preserves the pulse waveform.

The synchronized dynamics of the QW and QD carriers in the PRBS regime due to the high level of the optical power also provides the efficient XGM and eliminates the pattern effect [21]. The chirp of output signal wave $\left|\Delta\nu^s_{chirp}\right| \leq 2\ GHz$ remains comparatively small and symmetric. The QDWELL SOA performance is high even at the repetition rate of 140 Gb/s for the signal wave power $P_s = 1\ mW$ and a comparatively strong pumping power $P_p = 2\ mW$ [21]. It deteriorates at the extremely high repetition rate of 250 Gb/s because of the slow carrier dynamics. However, even in such a case, the QDWELL SOA performance can be improved by increasing optical pumping power P_p up to 20 mW [21]. However, for such a strong pumping, the XGM efficiency is decreasing since the gain saturates due to the depletion of the QD carriers. The QD levels are not filling rapidly enough from the QW carrier reservoir.

We theoretically investigated the extinction ratio (ER) dependence on the CW pumping power P_p and the detuning between the signal and pumping optical waves for $P_p = 0.01\ mW$ and 0.1 mW, signal wave optical power $P_s = 1\ mW$ and the signal wavelength $\lambda_s = 1.35\ \mu m$ [21]. It has been shown that ER reduces with the increase of the CW pumping power P_p and with the increase of the detuning [21].

4. The applications of QD-SOA in optical signal processing

In this section, we discuss the applications of QD-SOA in all-optical generation of UWB impulse radio signals [24, 25], ultra-fast all-optical processor [27, 28] and all-optical memory [29, 30].

4.1. All-optical generation of UWB impulse radio signals based on MZI with QD-SOA

UWB communication systems are characterized by low power consumption, immunity to multipath fading, precise object location, and high data rates [39]. However, they can operate in the frequency range from 3.1 to 10.6 GHz with an effective isotropic radiated power level of less than -41 dBm/MHz according to the U.S. Federal Communication Commission (FCC) decision [24, 40]. For this reason, UWB wireless systems are limited by short distances of a several tens of meters [40]. In order to increase the area of coverage, the UWB- over-optical-fiber (UROOF) technology had been proposed [24, 39, 40]. UWB-over-fiber technology can be used for radars, wideband wireless personal area networks (WPAN), sensor networks, imaging systems UWB positioning systems, and so on (see [24] and references therein). In particular, impulse-radio (IR) UWB technology is important where the information is carried by a set of narrow electromagnetic pulses with a bandwidth inversely proportional to the pulse width [24]. Carrier-free impulse modulation avoids complicated frequency mixer, intermediate frequency carrier and filter circuits and has better pass-through characteristic due to the base-band transmission [39]. For instance, Gaussian monocycle and doublet pulses, which are the first and second order derivatives of Gaussian pulse, respectively have lower bit error rate better multipath performance and wider bandwidth as compared to other impulse signals [39, 40].

There exist different methods of the optical IR UWB generation [39–44]. Different optically based systems for the generation of the Gaussian IR UWB monocycles and doublets may include an electro-optic phase modulator (EOPM), a single mode fiber (SMF), erbium-doped fiber amplifier (EDFA), SOA, a fiber Bragg grating (FBG), a photodetector (PD), a Sagnac interferometer, photonic microwave filters [39–44]. The shortages of such systems are the necessity of the complicate electronic circuit for the generation of the short electric Gaussian pulses, the use of EOM and long SMF.

We proposed a novel all-optical method of IR UWB pulse generation based on the integrated MZI with QD-SOA inserted into one arm of the integrated MZI [24]. An intensity-dependent signal interference occurs at the output of the MZI with QD-SOA. The proposed UWB IR signal generation process is based on the XGM and XPM processes in QD-SOA, which are characterized by strong optical nonlinearity and high operation rate as it has been mentioned earlier.

The block diagram of the proposed all-optical UWB IR signal consisting of a CW laser, MZI with a QD-SOA as an active element in the upper arm of the MZI, and a pulsed laser is shown in **Figure 5**. A CW signal of a wavelength λ and an optical power P_0 is split into two signals with the equal optical power $P_0/2$ and inserted into the two ports of the integrated MZI. The train of the short Gaussian pulses generated by the pulsed laser is counter-propagating with respect to the CW optical wave. The optical signal in the lower signal of MZI remains CW while the CW signal propagating through the MZI upper arm transforms into the Gaussian pulse at the MZI output due to the XGM and XPM in the QD-SOA. These pulses from the lower and upper arms interfere at the MZI output. The shape of the output pulse is determined by the power-dependent phase difference $\Delta\theta(t) = \theta_1(t) - \theta_2(t)$ where $\theta_{1,2}(t)$ are the phase shifts in the upper and lower MZI arms, respectively. The MZI output optical power P_{out} is given by [24]

$$P_{out}(t) = \frac{P_0}{2}\left[G_1(t) + G_2(t) - 2\sqrt{G_1(t)G_2(t)}\cos\Delta\theta(t)\right] \tag{21}$$

where $G_{1,2}(t)$ are the amplification factors of the upper and lower MZI arms. In our case, the upper arm amplification factor $\exp(g_{sat}L) \le G_1(t) = \exp(gL) \le \exp(g_0L)$ is limited by the QD-SOA saturation gain g_{sat} and the maximum modal gain g_0 for the linear regime. The lower arm amplification factor $G_2 = 1$. We neglect the losses in the proposed system because of the small

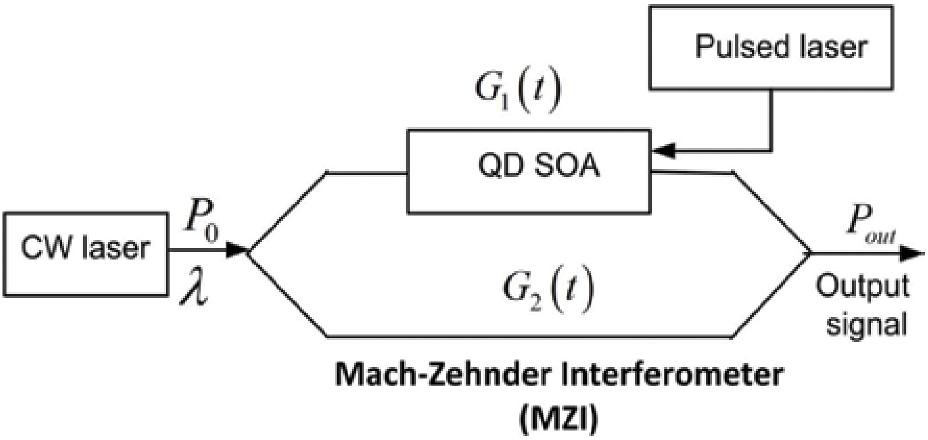

Figure 5. Block diagram of the all-optical UWB IR signal generator based on the MZI with QD-SOA as an active element.

lengths of the integrated elements. The XGM and XPM in QD-SOA are described by Eqs. (1)–(5). The relation between the MZI phase shift $\Delta\theta(t)$ and the upper arm amplification factor $G_1(t)$ has the form $\Delta\theta(t) = -(\alpha/2)\ln G_1(t)$. We solved numerically Eqs. (1)–(5) for the typical values of the QD-SOA material parameters mentioned above, the QD-SOA active region length $L = 2\ mm$, its width $W = 10\ \mu m$, confinement factor $\Gamma = 3 \times 10^{-2}$, the maximum QD-SOA gain $g_{\max} = 11.5\ cm^{-1}$, and the QD-SOA losses $\alpha_{\text{int}} = 3\ cm^{-1}$ [24]. The simulation results show that at the high Gaussian pulse power levels, QD-SOA passes to the saturation regime accompanied by the decrease of the XPM phase shift $\Delta\theta(t)$ and the upper arm amplification factor $G_1(t)$ to their minimum values. In such a case, the MZI output signal power P_{out} also has its minimum value due to the maximum value of the oscillating term in Eq. (21). Then, the XPM process is dominant, and the Gaussian doublet occurs at the MZI output [24]. In the opposite case of the weak Gaussian pulse, QD-SOA operates in the linear regime, and the Gaussian pulse remains unchanged [24]. The simulation results for the temporal dependence of the output signal power, optical signal power in the MZI upper and lower arms, and the MZI phase difference for the pulse power $P_p = 0.5\ mW$ and the CW power $P_{CW} = 0.005\ mW$ are presented in **Figure 6**. Different input power levels provide different contributions of the XGM and XPM processes in QD-SOA, which results in the different shapes of the MZI output pulses. Actually, the shape of the signal and its spectrum can be tailor-made [24].

The spectrum of the simulated UWB IR signal exhibits the filtering features of the proposed generator [24]. Indeed, for the Gaussian pulses duration $\sim 10^{-11}\ s$, a rise time and a fall time of the pulse propagating through the QD-SOA are limited by the fast transition time $\tau_{12} \sim 1\ ps$ between GS and ES.

4.2. Ultrafast all-optical processor based on QD-SOA

The major application areas of SOA-based MZI are all-optical logic gates, optical WC, and optical regenerators. The latter devices provide the so-called 3R regeneration [3], that is,

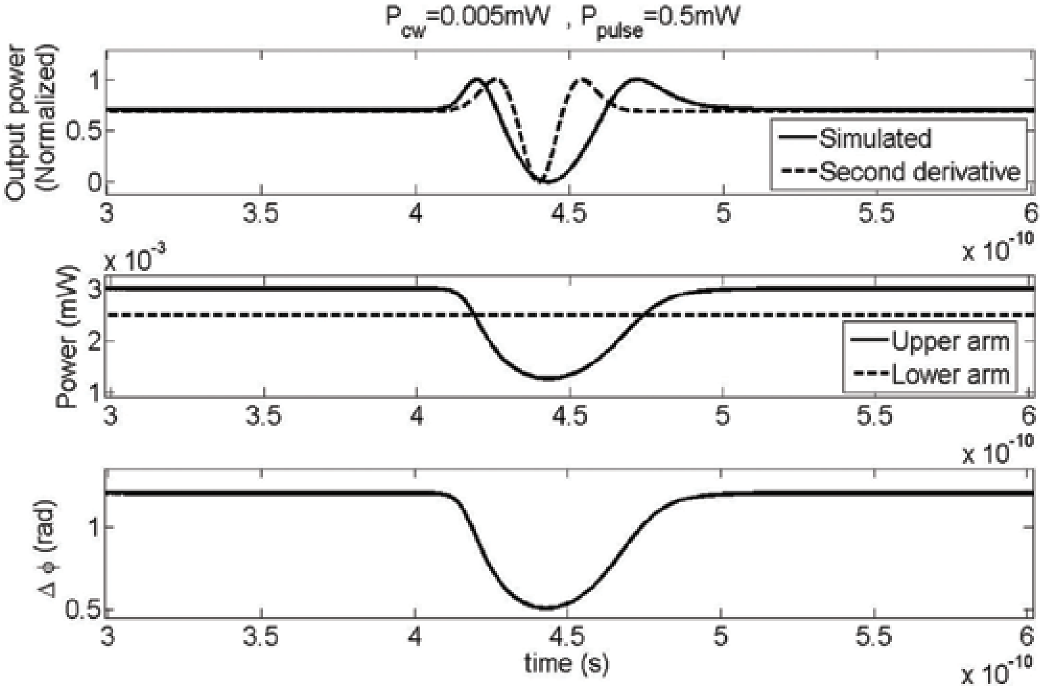

Figure 6. The temporal dependence: Gaussian doublet (solid line) and the second derivative of the Gaussian pulse (dashed line) for $P_p = 0.5\ mW$ and $P_{CW} = 0.005\ mW$ (the upper box); the optical signal power in the MZI upper arm (solid line) and the lower arm (dashed line) (intermediate box); the phase difference (lower box).

re-amplification, re-shaping, and re-timing which are necessary for the elimination of the noise, crosstalk and nonlinear distortions and for the transmission of the good quality signals over sufficiently large distances in all-optical networks (see [27, 28] and references therein).

We proposed a theoretical model of an ultrafast all-optical signal processor based on MZI containing QD-SOA in each arm (QD-SOA-MZI) where XOR logic operation, wavelength conversion, and 3R signal regeneration can be realized simultaneously by AO-XOR logic gates for the bit rates up to 100 Gb/s for the bias current $I \approx 30\ mA$ and 200 Gb/s for the bias current $I \approx 50\ mA$ [27].

The block diagram of AO-XOR logic gate based on the QD-SOA-MZI is shown in **Figure 7**.

The theoretical analysis of the proposed processor is based on the QD-SOA dynamics described by Eqs. (1)–(5) and the expression for the MZI output power (21). However, this time, QD-SOA are situated in both arms of the MZI, and the QD-SOA amplification factors $G_{1,2}(t)$ have the form $G_{1,2}(t) = \exp\left(g_{1,2}L_{1,2}\right)$ where $g_{1,2}; L_{1,2}$ are the first and second QD-SOA gains and active region lengths, respectively. When the control signal A and/or B are fed into the two QD-SOA, they modulate the SOA gains and also phase of the co-propagating CW signal due to LEF α according to Eq. (5). The phase shift at the QD-SOA-MZI has the form [27]:

$$\Delta\theta(t) = -(\alpha/2)\ln[G_1(t)/G_2(t)] \tag{22}$$

For the typical values of LEF $\alpha = (5 - 7)$, gain $g_{1,2} = 11.5\ cm^{-1}$ and $L_{1,2} = 1500\ \mu m$ the phase shift of about π can be achieved.

We start with the operation of the logic gate based on the QD-SOA-MZI, which consists of a symmetrical MZI with one QD-SOA in each arm [27, 28]. Two optical control beams A and B at the same wavelength λ are fed into the ports A and B of QD-SOA-MZI separately. A third signal representing a clock stream of CW series of unit pulses is split into two equal parts and injected in two QD-SOA. Two cases of the detuning between the signals A, B and the clock stream may occur. If the detuning is less than the QD homogeneous broadening, then the ultrafast operation can be realized. If the detuning is large and compared to the QD inhomogeneous broadening XGM in DQ SOA is also possible due to the QD interaction through WL for the comparatively low bit rates up to 10 Gb/s [11]. Such a case is discussed in subsection 2.3.

Suppose that the data stream at the input of the QD-SOA-MZI is absent: $A = B = 0$. In such a case, the phase difference of the signal propagating through both arms of QD-SOA-MZI is π, and the output signal is "0" because of the destructive interference [27]. Let now $A = 1, B = 0$. Then, the signal propagating through the upper arm and interacting with the data stream A acquires the additional phase determined by XPM between the signal and A while the phase of the signal propagating through the lower arm of the QD-SOA-MZI does not change. As a result, the output signal is "1" [27]. Evidently, the same output corresponds to the input $A = 0, B = 1$. Finally, in the case when $A = 1, B = 1$ the phase changes of the signal in both arms of the QD-SOA-MZI are equal, and the output signal is "0" [27].

Consider now the wavelength conversion in the proposed processor. An ideal WC must be characterized by the following properties: transparency to different bit rates and signal formats, fast setup of the output wavelength, the possibility of conversion to shorter and longer wavelengths, moderate input power levels, the possibility for no conversion regime, insensitivity to

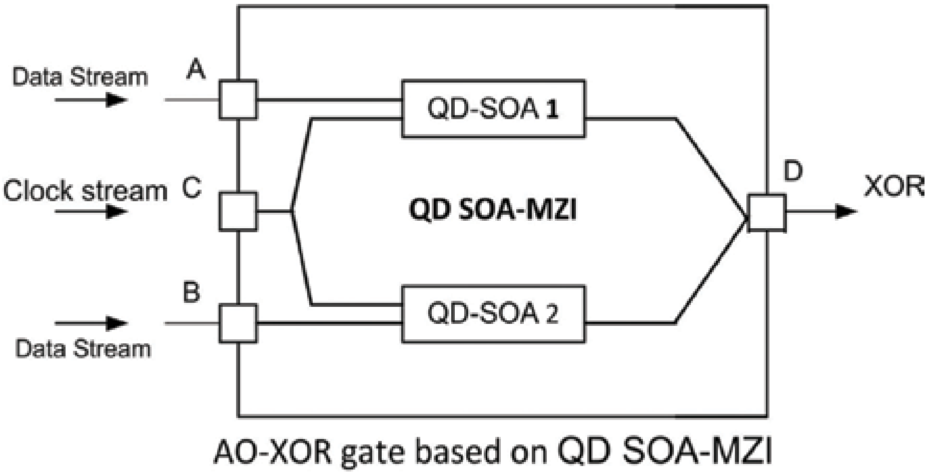

Figure 7. The block diagram of the AO-XOR logic gate based on QD-SOA-MZI.

the input signal polarization, the output signal with low chirp, high ER and large signal-to-noise ratio (SNR), and simple implementation [45]. SOA is a promising candidate for applications in WC because it possesses these characteristics.

WC performance can be substantially improved by replacing the bulk SOA with QD-SOA due to its specific features discussed in Section 2: the pattern-free high-speed wavelength conversion of optical signals by XGM, a low threshold current density, a high material gain, high saturation power, broad gain bandwidth, and a weak temperature dependence as compared to bulk and MQW SOA [9–11]. In the proposed ultrafast all-optical processor, the advantages of the QD-SOA as a nonlinear component and of the MZI as a system with the controlled output signal [27, 28]. Consider the situation where one of the inputs signals A or B is absent. In such a case, CW signal with the required output wavelength is split asymmetrically between the QD-SOA-MZI arms and interferes at the QD-SOA-MZI constructively or destructively with the intensity modulated input signal at another wavelength. The interference result depends on the phase difference between the two QD-SOA-MZI arms output, which is actually determined by the corresponding QD-SOA. The QD-SOA-MZI operates as an amplifier of the propagating signal. The operation with the output "1" can be defined as a wavelength conversion caused by XGM between the input signal A or B and the clock stream signal [27, 28]. The $(10-40)\ Gb/s$ pattern-effect-free wavelength conversion by XGM at the wavelength $\lambda = 1.3\ \mu m$ using QD-SOA with InGaAs/GaAs self-assembled QD had been demonstrated experimentally [7].

The deterioration of the ultrafast all-optical processor with the bit rate increase is shown in **Figures 8** and **9**. For the bias current $I = 30\ mA$ and the bit rate of $100\ Gb/s$, the patterning effect is moderate, and the eye in the eye diagram is open (**Figure 8**). For the bit rate of $200\ Gb/s$ at the same bias current, the patterning effect is strongly pronounced, and the eye is closed (**Figure 9**).

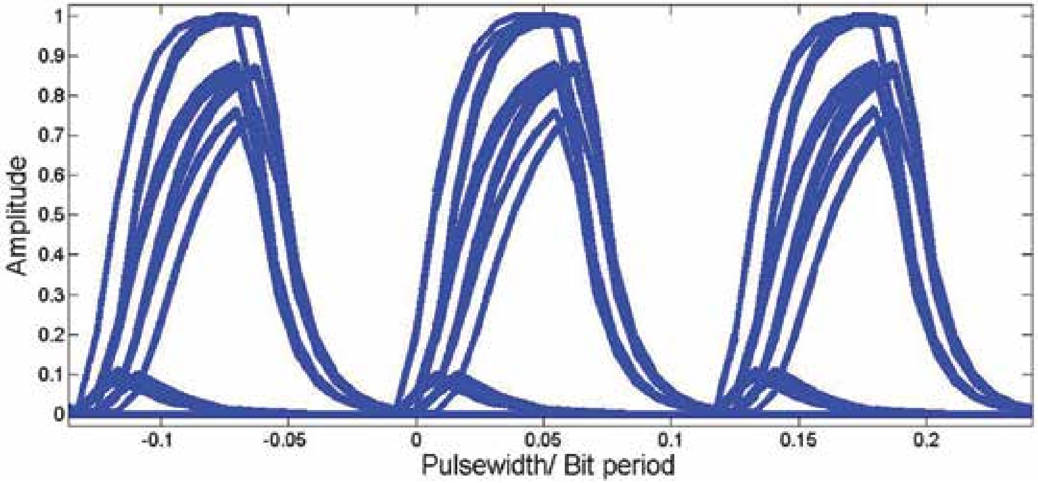

Figure 8. The eye diagram for the bit rate $100\ Gb/s$, the bias current $I = 30\ mA$.

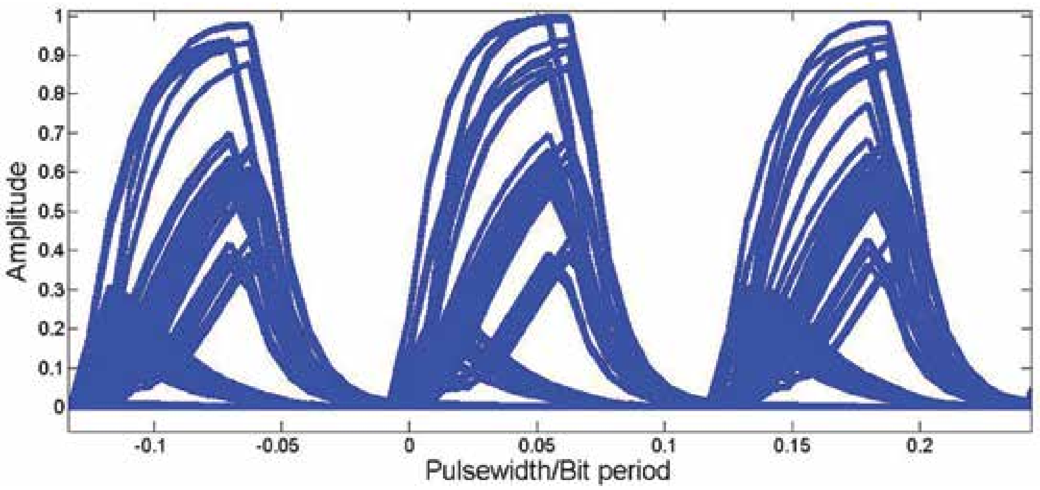

Figure 9. The eye diagram for the bit rate 200 Gb/s, the bias current $I = 30\ mA$.

The proposed ultrafast all-optical processor can solve three problems of the short pulse 3R regeneration mentioned above [27, 28]. The efficient pattern-effect-free signal re-amplification can be realized in each of the QD-SOA-MZI by the corresponding QD-SOA. The wavelength conversion based on all-optical logic gate discussed above can provide the reshaping since only the data signals can close the gate, while the comparatively weak noise cannot close the gate. The re-timing in the QD-SOA-MZI-based processor is provided by the optical clock stream, which is also necessary for the re-shaping. If the CW input signal is replaced with the optical clock stream, the 3R regeneration can be carried out simultaneously with the logic operations [27, 28].

4.3. Ultrafast all-optical memory based on QD-SOA

Optically assisted signal processing combines optical and electronic components [46]. For instance, optical components characterized by high operation rate can carry out some functions very fast, while the electronic components can realize the complex computations using buffers and memory [46]. In optical networks, the bandwidth mismatch between optical transmission and electronic routers requires a different optical signal processing and the study of the optical packet switching (OPS) [47]. The packet switching is used when it is necessary to select a packet of tens or hundreds of bits from a bit stream [48]. The flip-flop memory is an essential component of the packet switch in OPS networks, which is necessary for avoiding the packet collisions during packet routing [48, 49]. Usually, this memory consists of two coupled lasers switching the output signal between the wavelengths λ_1 and λ_2 [48]. We proposed a novel architecture of the all-optical memory loop based on the ultra-fast all-optical signal processor discussed in subsection 4.2 [29, 30]. The block diagram of the all-optical memory loop is shown in **Figure 10**.

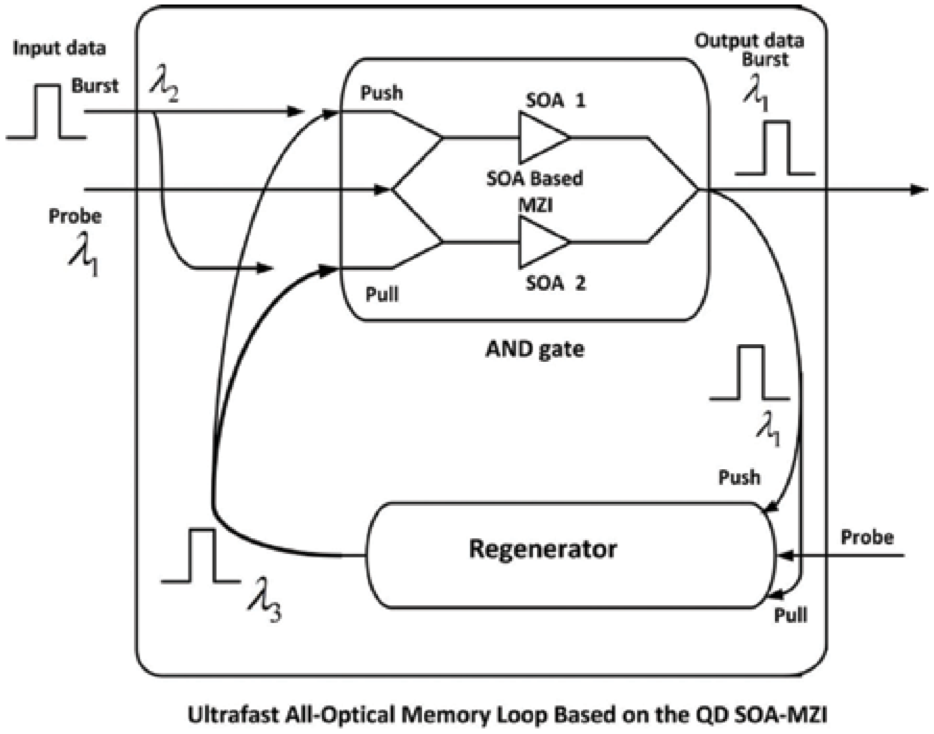

Figure 10. The block diagram of the ultrafast all-optical memory based on the QD-SOA-MZI.

The novel all-optical memory loop is characterized by the following advantages: (1) it includes only one QD-SOA-MZI reducing the complexity of the electronic synchronization scheme; (2) it can operate at the high bit rates up to 100 Gb/s due to fast GRT of QD-SOA discussed in subsection 2.2; (3) a regenerator is included into the loop for the optical fiber loss compensation and increasing of the loop length [28, 29]. The regenerator can be also based on SOA as it was mentioned above.

The QD-SOA dynamics and the ultra-fast all-optical processor operation principle have been discussed in detail in Section 2 and subsection 4.2, respectively. The theoretical model of the proposed all-optical memory loop is based on the QD-SOA carrier rate Eqs. (1)–(3), the average pump and signal wave photon densities $S_{p,s}(\tau)$ expression (10), the pump and signal wave phase $\theta_{p,s}$ expression (11), the modal gain $g_{p,s}$ expression (6), and the MZI output power P_{out} and phase difference $\Delta\theta$ expressions (21), (22), respectively. The phase difference $\Delta\theta$ at the output of the QD-SOA-MZI is defined by the optical signal power difference in the upper and lower arms of the QD-SOA-MZI. Typically, 80% and 20% of the input signal power were injected through the coupler into the upper and lower arms of the QD-SOA-MZI, respectively. Consequently, the dynamic processes in QD-SOA placed into the upper and lower arms of MZI are determined by different carrier relaxation time and GRT as it was mentioned in Section 2.

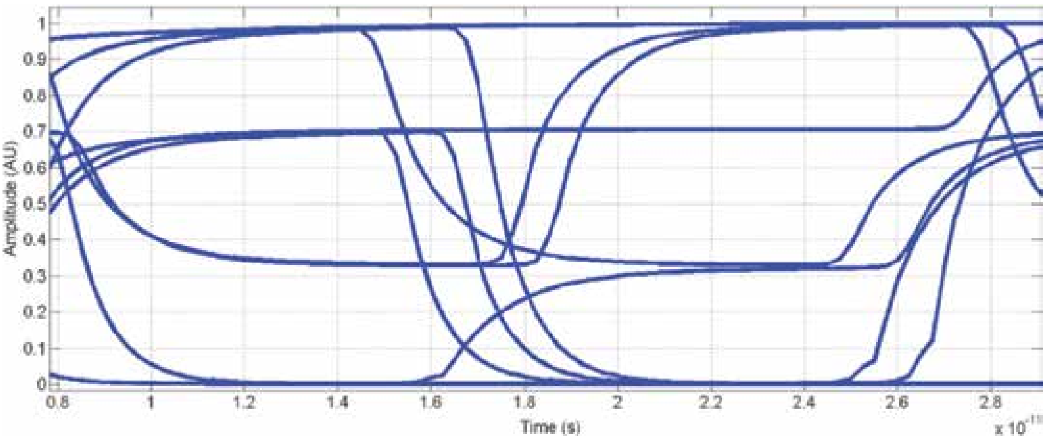

Figure 11. The eye diagram for the 4 PAM modulation format, a bit rate of 100 Gb/s; the signal is after one round in the all-optical memory loop.

We solved numerically Eqs. (1)–(3), (10), (11), (21), and (22) for the typical values of the material parameters presented in Section 2 in two cases: (1) the on–off keying (OOK) modulation format, the loop length $L_{loop} = 2\ km$, the bit rate 50 Gb/s and the quality factor at the input $Q = 15.8932$; (2) the pulse modulation 4 (4-PAM) format, the loop length $L_{loop} = 1\ km$, the bit rates 50 Gb/s and 100 Gb/s [28, 29]. In the case of the OOK modulation format, the numerical simulation results show that after four rounds in the loop the signal quality factor Q decreases by approximately 18% to 13.3156, and the patterning effect is slightly pronounced [28, 29]. In the case of the 4-PAM format, the patterning effect is negligible after two rounds in the loop for the bit rate of 50 Gb/s and it is slightly pronounced for the bit rate of 100 Gb/s [28, 29]. Hence, the performance of the QD-SOA-based all-optical memory does not deteriorate substantially up to the bit rate of 100 Gb/s.

For instance, the eye diagram for the 4 PAM modulation format and a bit rate of 100 Gb/s after 1 round in the all-optical memory loop is shown in **Figure 11**.

The numerical estimations show that for the loop length $L_{loop} = 1\ km$, the light velocity in the optical fiber $v \approx 2 \times 10^8\ m/s$ and the bit rates of 50 Gb/s and 100 Gb/s the all-optical storage values are of $0.25Mb$ and $0.5Mb$, and the storage times are $5\mu s$ and $10\mu s$, respectively [28, 29].

5. Conclusions

We studied theoretically the dynamics of QD-SOA. We solved numerically the QD-SOA carrier rate equations simultaneously with the truncated equations for the light wave photon density and phase. We have shown that the injection of the additional light wave drastically changes the QD-SOA dynamics. As a result, GRT may be strongly reduced by using the short Gaussian pulses and strong additional light wave. The lower GRT limit is defined by the QD-SOA fastest transition between ES and GS with the transition time $\tau_{21} = 0.16\ ps$. We investigated theoretically the specific features of XGM in QD-SOA. We have shown that the patterning effect manifests for the bit rates of about 10 Gb/s, but it can be diminished by increase of the bias current. However, at the higher bit rates of about 40 Gb/s, the bias current does not influence the patterning effect. The interaction between the nonresonant QD groups for the signal and pumping light waves with the detuning larger than the QD homogeneous broadening is possible for the large bias currents and fast pulses with the duration of nanoseconds and several dozen picoseconds. In such a case, QD can interact through WL due to the sufficiently fast relaxation carrier from WL to QD. QD-SOA have the lowest bias current, the highest operation bit rate, and the large gain bandwidth as compared to the bulk and MQW SOA. For this reason, they are the promising candidates for the all-optical signal processing.

The novel generation of QD lasers and SOA is based on the QDWELL structures where the self-assembled QD is imbedded into QW layers. The QW layers play a role of the reservoir for the 2D carrier gas instead of WL with the continuous carrier energy in ordinary QD-SOA. The complicated QDWELL laser and SOA dynamics are described by the system of LS rate equations for electrons and holes in QD and QW. The QDWELL laser and SOA performance are limited by the strongly desynchronized dynamics of electrons and holes in QD and QW. The different relaxation times of the electrons and holes in QW and QD are determined by the strongly nonlinear electron and hole scattering rates in and out of QD.

We solved numerically the modified LS rate equations and the truncated equations for the pumping and signal waves in the QDWELL SOA for the pulse regime and the large PRBS signal. We have shown that the strong optical injection with the power $(1-10)$ mW synchronizes the carrier dynamics in QDWELL SOA because the fast light stimulated transitions become dominant. The bias current remains comparatively low preventing the device heating. The propagation of the signal and CW pumping waves gives rise to the XGM. In such a case, the pumping wave in QDWELL SOA plays a role of the synchronizing optical injection. As a result, the QDWELL SOA performance significantly improves, the fast gain recovery occurs, the patterning effect vanishes, and the operation rate increases up to 140 Gb/s.

The QD-SOA can be successfully used in the all-optical signal processing due to their strong nonlinearity, high operation rate, and low bias current. We proposed a novel all-optical method of the UWB IR signal generation based on the integrated MZI with QD-SOA in each arm as a nonlinear element. The proposed method does not need SMF, EOPM, and FBG reducing complexity and cost of the UWB IR generator. The UWB IR signal generated by the QD-SOA-based MZI has a form of the Gaussian doublet.

We proposed a theoretical model of the ultrafast all-optical signal processor also based on QD-SOA-MZI structure. We have shown theoretically that such a processor may realize logic gate XOR operation, wavelength conversion, and 3R regeneration of the moderately distorted optical signals. The operation of the processor is based on the XGM and XPM in QD-SOA in both arms of the MZI. The processor limiting bit rate depends on the bias current I and may reach 200 Gb/s for $I = 50$ mA.

We proposed a novel architecture of the ultra-fast all-optical memory based on MZI with two QD-SOAs. The numerical simulation results for the OOK and 4 PAM modulation format show that the proposed memory is characterized by high operation rate up to 100 Gb/s due to the QD-SOA fast dynamics and in particular rapid gain recovery process. Evaluations show that for the 4 PAM modulation format, $l = 1km$ light velocity in the optical fiber $v \approx 2 \times 10^8\ m/s$ and typical values of the bit rate of 50 Gb/s and 100 Gb/s the memory storage values are 0.25 Mb and 0.5 Mb, respectively. The corresponding storage times are 5 μs and 10 μs, respectively.

Author details

Yossef Ben Ezra and Boris I. Lembrikov*

*Address all correspondence to: borisle@hit.ac.il

Department of Electrical Engineering and Electronics, Holon Institute of Technology (HIT), Holon, Israel

References

[1] Akiyama T, Sugawara M, Arakawa Y. Quantum-dot semiconductor optical amplifiers. Proceedings of the IEEE. 2007;**95**:1757-1766. DOI: 10.1109/JPROC2007.900899

[2] Rafailov EU, Cataluna MA, Avrutin EA. Ultrafast Lasers Based on Quantum Dot Structures. 1st ed. Wiley-VCH: Weinheim; 2011. p. 261. ISBN: 978-3-527-40928-0

[3] Sugawara M, Akiyama T, Hatori N, Nakata Y, Ebe H, Ishikawa H. Quantum-dot semiconductor optical amplifiers for high-bit-rate signal processing up to 160 Gbs^{-1} and a new scheme of 3R regenarators. Measurement Science and Technology. 2002;**13**:1683-1691. DOI: 10.1088/0957-0233/13/11/304

[4] Bakonyi Z, Onishchukov G, Lester LF, Gray AL, Newell TC, Tünnermann A. High-gain quantum-dot semiconductor optical amplifier for 1300 nm. IEEE Journal of Quantum Electronics. 2003;**39**:1409-1414. DOI: 10.1109/JQE.2003.818306

[5] Qasaimeh O. Optical gain and saturation characteristics of quantum-dot semiconductor optical amplifiers. IEEE Journal of Quantum Electronics. 2003;**39**:793-798. DOI: 10.1109/JQE.2003.810770

[6] Harrison P. Quantum Wells, Wires and Dots. 2nd ed. UK: Wiley; 2005. p. 508. ISBN: 978-0-470-01080-8 (PB)

[7] Sugawara M, Ebe H, Hatori N, Isida M, Arakawa Y, Akiyama T, Otsubo K, Nakata Y. Theory of optical signal amplification and processing by quantum-dot optical amplifiers. Physical Review B. 2004;**69**:235332-1-235332-39. DOI: 10.1103/PhysRevB.69.235332

[8] Qasaimeh O. Characteristics of cross-gain (XG) wavelength conversion in quantum-dot semiconductor optical amplifiers. IEEE Photonics Technology Letters. 2004;**16**:542-544. DOI: 10.1109/LPT.2003.821047

[9] Ben-Ezra Y, Haridim M, Lembrikov BI. Theoretical analysis of gain-recovery time and chirp in QD-SOA. IEEE Photonics Technology Letters. 2005;**17**:1803-1805. DOI: 10.1109/LPT.2005.853030

[10] Ben-Ezra Y, Haridim M, Lembrikov BI. Acceleration of gain recovery and dynamics of electrons in QD-SOA. IEEE Journal of Quantum Electronics. 2005;**41**:1268-1273. DOI: 10.1109/JQE.2005.854131

[11] Ben-Ezra Y, Haridim M, Lembrikov BI. Specific features of XGM in QD-SOA. IEEE Journal of Quantum Electronics. 2007;**43**:730-737. DOI: 10.1109/JQE.2007.901587

[12] Lüdge K. Modeling quantum-dot-based devices. In: Lüdge K, editor. Nonlinear Laser Dynamics. Weinheim, Germany: Wiley; 2012. pp. 3-33. ISBN: 978-3-527-41100-9

[13] Meuer C, Kim J, Laemmlin M, et al. High-speed small-signal cross-gain modulation in quantum-dot semiconductor optical amplifiers at 1.3 μm. IEEE Journal of Selected Topics in Quantum Electronics. 2009;**15**:749-756. DOI: 10.1109/JSTQE.2009.2012395

[14] Kim J, Laemmlin M, Meuer C, Bimberg D, Eisenstein G. Theoretical and experimental study of high-speed small-signal cross-gain modulation of quantum-dot semiconductor optical amplifiers. IEEE Journal of Quantum Electronics. 2009;**45**:240-248. DOI: 10.1109/JQE.2008.2010881

[15] Wegert M, Majer N, Lüdge K, et al. Nonlinear gain dynamics of quantum dot optical amplifiers. Semiconductor Science Technology. 2011;**26**:1-11. DOI: 10.1088/0268-1242/26/1/014008

[16] Wilkinson S, Lingnau B, Korn J, Schöll E, Lüdge K: Influence of noise on the signal quality of quantum-dot semiconductor optical amplifiers. IEEE Journal of Selected Topics in Quantum Electronics 2013; 19: 1900106-1-1900106-6. DOI: 10.1109/JSTQE.2012.2233464

[17] Pausch J, Otto C, Tylaite E, Majer N, Schöll E, Lüdge K. Optically injected quantum dot lasers: Impact of nonlinear carrier lifetimes on frequency-locking dynamics. New Journal of Physics. 2012;**14**:1-20. DOI: 10.1088/1367-2630/14/053018

[18] Ben-Ezra Y, Lembrikov BI. Synchronized carrier dynamics in quantum dot-in-a-well (QDWELL) laser under an optical injection. IEEE Journal of Selected Topics in Quantum Electronics. 2013;**19**:1901508-1-1901508-8. DOI: 10.1109/JSTQE.2013.2246770

[19] Ben-Ezra Y, Lembrikov BI. Quantum dot-in-a-well (QDWELL) laser dynamics under optical injection. Optical and Quantum Electronics. 2014;**46**:1239-1245. DOI: 10.1007/s11082-013-9829-3

[20] Ben-Ezra Y, Lembrikov BI. Semiconductor optical amplifier based on a quantum dot-in-a-well (QDWELL) structure under optical pumping. IEEE Journal of Quantum Electronics. 2014;**50**:340-347. DOI: 10.1109/JQE.2014.2308393

[21] Ben-Ezra Y, Lembrikov BI. Investigation of a cross-gain modulation (XGM) in a semiconductor optical amplifier (SOA) based on a quantum dot-in-a-well (QDWELL) structure. IET Optoelectronics. 2015;**9**:43-51. DOI: 10.1049/iet-opt.2014.0061

[22] Ben-Ezra Y, Lembrikov B. I: Improvement of the quantum dot-in-a-well (QDWELL) laser and amplifier performance under the optical injection. In: Pinho P, editor. Optical Communication Technology. Rijeka, Croatia: InTech; 2017. pp. 75-99. DOI: 10.5772/intechopen.69946

[23] Agrell E, Karlsson M, Chraplyvy AR, et al. Roadmap of optical communications. Journal of Optics. 2016;**18**(063002):1-40. DOI: 10.1088/2040-8978/18/6/063002

[24] Ben-Ezra Y, Haridim M, Lembrikov BI, Ran M. Proposal for all-optical generation of ultra wideband impulse radio signals in Mach-Zehnder interferometer with quantum dot optical amplifier. IEEE Photonics Technology Letters. 2008;**20**:484-486. DOI: 10.1109/LPT.2008.918256

[25] Ben Ezra Y, Lembrikov BI, Ran M, Haridim M. All-optical generation and processing of IR UWB signals. In: Lethien C, editor. Optical Fibre, New Developments. Vucovar, Croatia: InTech; 2009. pp. 425-444. ISBN: 978-953-7619-50-3

[26] Ran M, Ben-Ezra Y, Lembrikov BI. High performance analog optical links based on quantum dot devices for UWB signal transmission. In: Lembrikov BI, editor. Ultra-Wideband. InTech: Croatia; 2010. pp. 75-96. ISBN: 978-953-307-139-8

[27] Ben Ezra Y, Lembrikov BI, Haridim M. Ultra-fast all-optical processor based on quantum dot semiconductor optical amplifiers. IEEE Journal of Quantum Electronics. 2009;**45**:34-41. DOI: 10.1109/JQE.2008.2003497

[28] Ben Ezra Y, Lembrikov BI. New approach to ultra-fast all-optical signal processing based on quantum dot devices. In: Grym J, editor. Semiconductor Technologies. Croatia: InTech; 2010. pp. 419-436. ISBN: 978-953-307-080-3

[29] Ben Ezra Y, Lembrikov BI. All-optical memory based on quantum dot semiconductor optical amplifiers (QD-SOAs) for advanced modulation formats. In: Proceedings of 18th Int'l. Conf. on Transparent Optical Networks (ICTON 2016); July 10–14, 2016; Trento, Italy, Tu.A5.3 1–3. ISBN: 978–1–5090-1466-8

[30] Ben Ezra Y, Lembrikov BI. Ultra-fast all-optical memory based on quantum dot semiconductor optical amplifiers (QD-SOA). In: Roka R, editor. Optical Fiber and Wireless Communications. Rijeka, Croatia: InTech; 2017. pp. 279-293. DOI: 10.5772/intechopen.68527

[31] Uskov AV, Berg WT, Mork J. Theory of pulse-train amplification without patterning effects in quantum-dot semiconductor optical amplifiers. IEEE Journal of Quantum Electronics. 2004;**40**:306-320. DOI: 10.1109/JQE.2003.823032

[32] Qasaimeh O. Novel closed-form model for multiple-state quantum-dot semiconductor optical amplifiers. IEEE Journal of Quantum Electronics. 2008;**44**:652-657. DOI: 10.1109/JQE.2008.922324

[33] Borri P, Langbein W, Hvam JM, Heinrichsdorff F, Mao M-H, Bimberg D. Ultrafast gain dynamics in InAs-InGaAs quantum-dot amplifiers. IEEE Photonics Technology Letters. 2000;**12**:594-596. DOI: S 1041-1135(00)04605-X

[34] Berg WT, Bischoff S, Magnusdottir I, Mork J. Ultrafast gain recovery and modulation limitations in self-assembled quantum-dot devices. IEEE Photonics Technology Letters. 2001;**13**:541-543. DOI: S 1041-1135(01)04546-3

[35] Pleumeekers JL, Kauer M, Dreyer K, et al. Acceleration of gain recovery by optical injection in semiconductor optical amplifiers by optical injection near transparency wavelength. IEEE Photonics Technology Letters. 2002;**14**:12-14. DOI: S 1041-1135(02)00011-3

[36] Connely MJ. Semiconductor Optical Amplifiers. Dordrecht, The Netherlands: Cluver; 2002. p. 169. ISBN: 0-7923-7657-9

[37] Contestabile G, Maruta A, Sekiguchi S, Morito K, Sugawara M, Kitayama K. Cross-gain modulation in quantum-dot SOA at 1550 nm. IEEE Journal of Quantum Electronics. 2010; **46**:1696-1703. DOI: 10.1109/JQE.2010.2060714

[38] Lüdge K, Schöll E. Quantum-dot lasers desynchronized nonlinear dynamics of electrons and holes. IEEE Journal of Quantum Electronics. 2009;**45**:1396-1403. DOI: 10.1109/JQE.2009. 2028159

[39] Chen H, Chen M, Wang T, Li M, Xie S. Methods for ultra-wideband pulse generation based on optical cross-polarization modulation. Journal of Lightwave Technology. 2008; **26**:2492-2499. DOI: 10.1109/JLT.2008.927616

[40] Zeng F, Yao J. An approach to ultra-wideband pulse generation and distribution over optical fiber. IEEE Photonics Technology Letters. 2006;**18**:823-825. DOI: 10.1109/LPT.2006.871844

[41] Lin W-P, Chen Y-C. Design of a new optical impulse radio system for ultra-wideband wireless communications. IEEE Journal of Selected Topics in Quantum Electronics. 2006; **12**:882-887. DOI: 10.1109/JSTQE.2006.876613

[42] Li J, Xu K, Fu S, et al. Ultra-wideband pulse generation with flexible pulse shape and polarity control using a Sagnac-interferometer-based intensity modulator. Optics Express. 2007;**15**:18156-18161. ISSN: 1094-4087

[43] Zeng F, Wang Q, Yao J. All-optical UWB impulse generation based on cross-phase modulation and frequency discrimination. Electronics Letters. 2007;**43**:121-122. ISSN: 0013-5194

[44] Zeng F, Yao J. Ultra-wideband impulse radio signal generation using a high-speed electro-optic phase modualtor and a fiber-Bragg-grating–based frequency discriminator. IEEE Photonics Technology Letters. 2006;**18**:2062-2064. DOI: 10.1109/LPT.2006.883310

[45] Ramamurthy B. Swithches, wavelength routers, and wavelength converters. In: Sivalingam KM, Subramaniam S, editors. Optical WDM Networks. Principles and Practice. Boston: Kluwer; 2001. pp. 51-75 0-7923-7825-3

[46] Willner AE, Khaleghi S, Chitgarha MR, Yilmaz OF. All-optical signal processing. Journal of Lightwave Technology. 2014;**32**:660-680. DOI: 10.1109/JLT.2013.2287219

[47] Liu Y, Hill M T, Calabretta N, Tangdiongga E, Geldenhuys R, Zhang S, Li Z, De Waardt H, Khoe G D and Dorren H J S: All-optical signal processing for optical packet switching

networks. In: Proceedings of SPIE; 15 September 2005; San Diego, California, USA; 2005, 59070J-1-12. DOI: 10.1117/12.621346

[48] Agrawal GP. Fiber-Optic Communication Systems. 4th ed. New York: Wiley; 2010. p. 603. ISBN: 978-0-470-50511-3

[49] Xuelin Y, Qiwei W, Weisheng H. High-speed all-optical long-term memory using SOA MZIs: Simulation and experiment. Optics Communication. 2012;**285**:4043-4047. DOI: 10.1016/j.optcom.2012.06.027

Parametric Amplifiers in Optical Communication Systems: From Fundamentals to Applications

Jing Huang

Additional information is available at the end of the chapter

http://dx.doi.org/10.5772/intechopen.73696

Abstract

Optical parametric amplifiers (PAs) utilize highly efficient nonlinear effects in an optical fiber and they have the ability to operate in phase-sensitive mode. The inclusion of PAs in optical systems can give an ultimate limit for lumped amplified links in terms of achievable signal to noise ratio. The drawback is the complexity stemming from the requirement of phase matching a number of waves at each amplifier, phase lock, and the extra spectrum consumed by idler waves. In this chapter, the theories of a parametric amplifier, including the quantum-optical equations, are given. The properties of the gain saturation and the noise figure are presented. Practical amplifier systems and their applications in phase-sensitive amplification, all-optical signal regeneration, and squeeze state generation are outlined.

Keywords: four-wave mixing (FWM), modulation interaction (MI), gain, noise figure (NF), second harmonic generation (SHG), phase-sensitive amplification, parametric amplification

1. Introduction

Ultra-dense multi-channel transmissions at higher speed are required for the high capacity optical networks. These results in phase-based modulation such as binary and quadrature phase-shift keying (BPSK, QPSK) became increasingly interesting for optic communications in the years after 2000. And the application of optical parametric amplifiers (OPA) also becomes promising. The main reason for the current interest for parametric amplifiers is the ability to operate in phase-sensitive mode. Furthermore, OPA provides high gain (reaching to 10^4) and it can be used to handle high average powers. The drawback is the complexity stemming from the requirement of phase matching a number of waves at each amplifier, and the extra spectrum consumed by idler waves [1].

In 1985, Pocholle et al. explored FWM for fiber-optic amplification [2]. The first phase-sensitive gain in an optical fiber was observed by Bar-Joseph et al. [3]. In 1993, Levenson et al. [4] observed the first optical amplification (in a KTP crystal) with a noise figure below the 3 dB limit. Marhic et al. [5] used a fiber Sagnac interferometer to realize parametric gain via degenerate FWM, and a similar structure was used by Imajuku et al. in 1999 [6], who reported the first $\chi^{(3)}$-based parametric amplifier with a noise figure of 1.8 dB.

In parametric amplifiers, the stimulated Brillouin scattering (SBS) was suppressed by a broadband phase modulation of the pump. This pump phase modulation has some unwanted effects, such as idler spectral broadening and it is generally deleterious (but no fundamental obstacle) when realizing phase-sensitive amplifiers. However, such a fiber, with an induced strain gradient to suppress SBS, enabled phase-modulation-free CW pumping with 10 dB gain [7].

In 2005, Tang et al. [8] demonstrated phase-sensitive gain in a highly nonlinear fiber (HNLF) by first generating three phase-locked waves in a conventional phase-insensitive fiber-optic parametric amplifier (FOPA) and then injecting these into a second FOPA, which now became phase sensitive. The phase-sensitive nature was elegantly manifested as wavelength oscillations of the FOPA noise spectrum by inserting a dispersive fiber between the two FOPAs. This was the first realization of the copier-phase-sensitive amplifier (PSA) scheme. A number of important theoretical contributions to FOPAs and PSAs were published around this as well; notably by McKinstrie who analyzed phase-sensitive amplification classically [9] as well as quantum mechanically [10, 11]. Also, Marhic et al. contributed significantly, e.g., with work on the FOPA gain spectrum [12, 13]. Michel Marhic, who tragically passed away in 2014, also published the first book [14] on parametric fiber devices in 2008. In a series of papers by Croussore et al. [15–17], phase regenerators were realized and evaluated, being among the first PS devices to gain traction in the community. These were based on interferometric, degenerate parametric fiber devices.

The organization of this paper is as follows: Section 2 discusses fiber FWM from a fundamental perspective leading to the work on parametric amplifiers and the various flavors of these that exist; Section 3 presents the mathematical theory of FWM in fibers, Section 4 presents the 2-mode PSA and the coherent superposition; and Section 5 describes the PSA noise properties, both from a semi-classical and a quantum mechanical perspective, and gain saturation properties. At the last parts, the copier-PSA setup that has been used in experiments including the polarization properties and nonlinear tolerance, the practical systems of parametric amplifier, and their applications are introduced.

2. Fiber optic parametric amplifier theory

In fibers, the refractive index is a function of the light intensity. If two waves (ω_1 and ω_2) copropagate in a medium, they will interfere and create a moving grating, and a third wave ω_3 may scatter, and then a fourth wave at ω_4 may generate. This is named as four-wave mixing. The fourth wave will be generated at a frequency which is the Doppler-shifted from scattering wave, $\omega_4 = \omega_3 + \omega_2 - \omega_1$. For the process to be efficient, the corresponding Bragg condition $\beta_4 = \beta_3 + \beta_2 - \beta_1$ must also be satisfied, where β_k is the propagation constants of wave k. This is also commonly referred to as the phase-matching condition. Note that both the Doppler and Bragg conditions need to be fulfilled for FWM to be efficient, and for a given dispersion relation $\beta(\omega)$, both conditions are not generally satisfied. However, around the zero-dispersion wavelength they are. This is the classical picture of FWM, and it is also very useful in understanding the polarization properties.

Light propagation in optical fibers is remarkably well described by the nonlinear Schrodinger Equation (NLSE), in a slightly generalized form with all dispersive orders as

$$i\frac{\partial u}{\partial z} + \beta\left(\omega_0 - i\frac{\partial}{\partial t}\right)u + \gamma|u|^2 u = 0 \tag{1}$$

where $\beta(\omega)$ is the dispersion relation of the fiber, ω_0 is the carrier frequency, the independent variable z is the fiber length, and the local time is t. As written, $\beta(\omega_0 - i\partial/\partial t)$ should be interpreted as a differential operator, defined by the Taylor expansion of β around ω_0. The field amplitude $u(z, t)$ is chosen so that $|u|^2$ is the propagated power in Watt units. The nonlinear coefficient γ is around 15 $(\mathrm{W\ km})^{-1}$ for HNLFs. Losses are neglected as the propagation is only over a few 100 m of HNLF.

Consider the propagation of three waves, a pump symmetrically surrounded by a signal and an idler wave, i.e., $u = u_p\exp(i\omega_p t) + u_s\exp(i\omega_s t) + u_i\exp(i\omega_i t)$, where $2\omega_p = \omega_i + \omega_s$. We assume CWs, so that $u_{p,s,i(z)}$ are the functions of z only. After inserting this into the NLSE, we collect terms oscillating at the three separate frequencies and neglect the others. The result is the coupled system

$$\frac{\partial u_p}{\partial z} = iu_p\left[\beta_p + \gamma\left(2P - |u_p|^2\right)\right] + i\gamma 2u_p^* u_s u_i \tag{2}$$

$$\frac{\partial u_s}{\partial z} = iu_s\left[\beta_s + \gamma\left(2P - |u_s|^2\right)\right] + i\gamma 2u_p^2 u_i^* \tag{3}$$

$$\frac{\partial u_i}{\partial z} = iu_i\left[\beta_i + \gamma\left(2P - |u_i|^2\right)\right] + i\gamma 2u_p^2 u_s^* \tag{4}$$

$P = |u_s|^2 + |u_p|^2 + |u_i|^2$ is the total power.

The pump power is much larger than the signal power, i.e., $|u_p|^2 = P_p >> |u_{s,i}|^2$. Then (2) for the pump can be approximately solved as $u_p(z) = \sqrt{P_p}\exp[i(\beta_p + \gamma P_p)z]$. After inserting this into (3) and (4) and peeling off the phase via the substitution $u_{s,i} = e_{s,i}\exp(i(\kappa + \beta_{s,i})z)$, one has a coupled first-order system with constant coefficients as

$$\frac{de_s}{dz} = i\kappa e_s + i\gamma P_p e_i^* \tag{5}$$

$$\frac{de_i^*}{dz} = -i\kappa e_i^* - i\gamma P_p e_s \tag{6}$$

Here, we introduced the notation $\kappa = \gamma P_p + \Delta\beta/2$, where $\Delta\beta = 2\beta_p - \beta_s - \beta_i$ is the linear phase mismatch. In matrix form

$$\frac{d}{dz}\vec{E}(z) = i\begin{vmatrix} \kappa & \gamma P_p \\ -\gamma P_p & -\kappa \end{vmatrix}\vec{E} = M\vec{E} \tag{7}$$

where M is the coefficient matrix and $\vec{E}(z) = \begin{vmatrix} e_s(z) \\ e_i^*(z) \end{vmatrix}$. A convenient way is to use the matrix exponential, to write the solution as

$$\vec{E}(z) = \exp(iMz)\,\vec{E}(0) = K(z)\,\vec{E}(0) \tag{8}$$

The transfer matrix $K(z)$ can be explicitly expressed as

$$\begin{aligned} K &= I\cosh(gz) + iM\frac{\sinh(gz)}{g} \\ &= \begin{vmatrix} \cosh(gz) + i\dfrac{\kappa}{g}\sinh(gz) & i\dfrac{\gamma P_p}{g}\sinh(gz) \\ i\dfrac{\gamma}{g}\sinh(gz) & \cosh(gz) - i\dfrac{\kappa}{g}\sinh(gz) \end{vmatrix} \end{aligned} \tag{9}$$

Here, $g = (\gamma P_\mathrm{p})^2 - \kappa^2$ is the parametric gain coefficient, which is maximum when κ vanishes, and this occurs when the linear mismatch balances the nonlinear phase shift.

The maximum parametric gain (for $\kappa = 0$) equals $G = \cosh^2(\gamma P_p z)$, and it is the phase-insensitive gain, since it is the gain the signal wave gets when no idler is present at the input. It grows exponentially with the nonlinear phase shift $\gamma P_p z$. If the pump lies exactly on the zero-dispersion frequency, the linear mismatch $\Delta\beta$ vanishes, and the transfer matrix reduces to

$$K = I + iMz = \begin{vmatrix} 1 + i\gamma P_p z & i\gamma P_p z \\ -i\gamma P_p z & 1 - i\gamma P_p z \end{vmatrix} \tag{10}$$

which is linear in the nonlinear phase shift. The corresponding parametric gain is quadratic in the nonlinear phase shift. However, this scheme has theoretically very large bandwidth that in practice will be limited by longitudinal zero-dispersion variations [18, 19] and/or higher orders of dispersion [12].

The properties of the transfer matrix K are important in order to understand and explain the gain and noise properties of parametric amplifiers. It is often given in a general form as

$$K = \begin{vmatrix} \mu & \nu \\ \nu^* & \mu^* \end{vmatrix} \tag{11}$$

where μ and ν are complex coefficients, so that $|\mu|^2 - |\nu|^2 = 1$.

Eq. (11) parameterizes the set of matrices that preserve the invariant. Matrices with this property form a group, the symplectic group, which means that the product of two symplectic matrices is also symplectic. It is interesting to compare and contrast with the unitary group, which preserve the sum of the powers (rather than the difference) and has a similar (but not equivalent) parameterization. The symplectic property was discussed for parametric processes in [20].

By inspection of the form of K in (11), we can draw some important conclusions. The phase-insensitive gain is $G = |\mu|^2$ and the idler conversion efficiency is $\eta = |\nu|^2 = G - 1$. The absolute phases of the μ and ν coefficients are mostly of less interest, and in many cases, it is enough to characterize the transfer matrix by the single parameter G.

3. Phase-sensitive parametric amplifier

If both waves (signal and idler) are present at the input, the interaction given by the matrix K above is phase sensitive, i.e., the two waves $e_{s,in}$ and $e_{i,in}$ will be coherently superposed, as in interferometry, so the corresponding output waves will be

$$e_{s,out} = \mu e_{s,out} + \nu e^*_{i,in} \tag{12}$$

$$e^*_{i,out} = \nu^* e^*_{i,in} + \mu^* e_{s,in} \tag{13}$$

In reality this is difficult to realize as it requires phase-locking between the pump, signal, and idler waves. The three waves can be generated by either using a "copier," as done originally by Tang et al. [8] or by using phase-locked frequency lines from a single laser source by, e.g., external modulation, as used in the work by Bar-Joseph et al. [3].

We see directly from the transfer equations that a two-mode PSA with equal signal and idler powers will experience a phase dependent gain for the signal as

$$G_{PSA} = \frac{|e_s\mu + e_i^*\nu|^2}{|e_s|^2} \tag{14}$$

For equal input signal and idler powers, this can be written

$$G_{PSA}(\phi) = |\mu|^2 + |\nu|^2 + 2|\mu||\nu|\cos(\phi) \tag{15}$$

where ϕ is the phase angle of $\mu e_s \nu^* e_i^*$, which we can interpret as the phase difference $\phi = \phi_s + \phi_i - 2\phi_p$ between the pump and signal waves entering the amplifier. We can take the pump phase to be zero, which is of no restriction. Clearly, this gain is maximum (minimum) for $\phi = 0 (\phi = \pi)$. It is straightforward to show that the maximum and minimum phase-sensitive gains are reciprocal, i.e., $G_{max/min} = (|\mu| \pm |\nu|)^2 = \exp(\pm 2\gamma P_p z)$. In a degenerate PSA, where the idler and the signal are the same, $\phi = 2\phi_s$, and then one quadrature $\phi_s = 0$ of the signal will exhibit gain and the other $\phi_s = \pi/2$ will exhibit anti-gain (or parametric loss). In other words, one quadrature is parametrically amplified, and the other is attenuated the same amount. This has also been clearly verified experimentally. The phase modulation applied to the pump, used to suppress SBS, reduces fidelity in such experiments by limiting the parametric attenuation, but phase-sensitive gains of up to 30 dB have been observed [21].

It is also notable that in the high-gain regime $\mu \approx \nu \approx \sqrt{G}$, and the $G_{max} = G_{PSA}(0) \approx 4|\mu|^2 = 4G$, there is $6dB$ difference between the phase-sensitive and phase-insensitive gain. This is due to the coherent superposition of two waves, and it can be generalized to give N^2-fold increase for an N-mode amplifier. For example the 4-mode PSA, the PS gain is 16 times of the PI. In the corresponding experiment, 10.5 dB was measured [22].

The specific eigenmodes that are amplified/attenuated may differ in various systems. For example, in the 2-mode amplifier, there can be linear combinations so that $e_s + e_i^*$ exhibits gain and $e_s - e_i^*$ exhibits loss. By decomposing the transfer matrix into a matrix product whose elements are defined by its eigenmodes and eigenvalues (i.e., singular value decomposition, but in this context called Schmidt decomposition and Schmidt modes), one can gain further insight into multimode phase-sensitive processes [23].

4. Saturation gain of parametric amplifier

When power is transferred from the pump to the signal, the optical-pump power cannot sustain the exponential growth of the gain, saturation occurs [24]. The relative magnitudes of the pump and signal/idler powers will affect the flow of power between them due to the nonlinear phase-matching condition.

The asymptotic power conversion corresponds to a gain that can be expressed as

$$G(P_{s0}) = \frac{G_0}{1 + P_{s0}/P_{sat}} \tag{16}$$

where G_0 is the unsaturated gain given by

$$G_0 = 1 + \frac{16}{7}\sinh^2\left(\frac{\sqrt{7}}{4}\gamma P_p L\right) \tag{17}$$

and P_{s0} is the signal input power. The saturation power P_{sat} is given by

$$P_{sat} = \frac{1}{2}\frac{P_p}{G_0} \tag{18}$$

This saturation power can be interpreted as the input signal power required for the gain G_0 to convert the whole pump to the signal and idler waves. These equations are only valid for the single wavelength when the pump is totally converted and under the assumption of three waves only.

In **Figure 1**, the gain spectrum as a function of λ_n for different signal input powers are plotted. Here, $\lambda_n = (\lambda_s - \lambda_p)/(\lambda_{max} - \lambda_p)$ is the signal wavelength normalized so that $\lambda_n = 1$ corresponds to the maximum gain wavelength λ_{max}, $\lambda_n = 1/2$ is the asymptotic conversion wavelength, and $\lambda_n = 0$ is the pump wavelength.

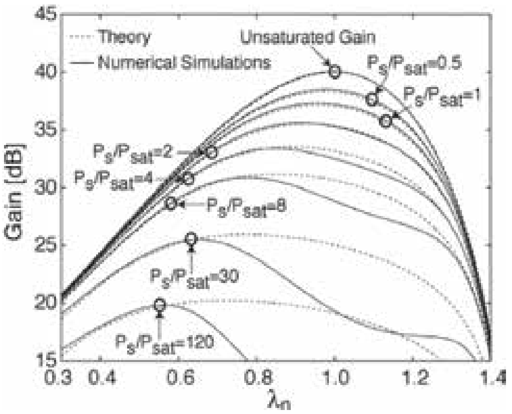

Figure 1. Gain spectrum as a function of λn for different signal input powers. $Ps0$ is normalized to the saturation power at the gain peak $P_{sat,max}$, P_s/P_{sat}. The peak gain is 40 dB, and $P_{s0}/P_{sat,max}$ = 0 (unsaturated gain), 0.50, 1, 2, 4, 8, 30, and 120.

The signal input powers are normalized to the saturated gain at the gain-peak wavelength according to $P_{s0}/P_{sat,max}$. As the input power increases, the peak gain shifts toward the pump wavelength, because the nonlinear phase matching is altered as the signal/idler powers increase. The pump is completely converted at λ_n = 0.5. The peak gain is shifted to that wavelength of higher input power and at other wavelengths, the power is periodically exchanged between the signal/idler and optical pump with length. This also explains the dramatic change in gain which is reduced at higher normalized input powers.

5. Noise in amplifiers

This section will discuss the noise properties of parametric amplifiers and in particular PSAs. We will consider both the semi-classical approach and the quantum mechanical.

5.1. Semi-classical model

The semi-classical model of light-matter interaction means that one has a classical field formulation, but a quantum mechanical model of matter. When modeling noise in optical amplification, the amplifier has spontaneously emitted photons that can be treated as additive noise and that have (at the amplifier input) a power spectral density of half a photon per mode.

From this assumption, a lot of well-known results follow; for example, the shot noise power spectral density and the familiar result for amplifier noise figures. The NF is defined as the ratio of input to output SNR (in the electrical domain, after ideal photodetection) of an optical amplifier. It is also a measure of the amount of spontaneous emission noise an amplifier adds to a signal.

Phase-insensitive amplifiers (PIA) have a noise figure of NF_{PIA} = 2–1/G, approaching 3 dB for high gain. Parametric amplifiers have, in phase-sensitive operation, a noise figure of NF_{PSA} = 1 (gain is 0 dB) instead, because the quantum noise is unevenly between the adjoining quadratures (which is known as squeezing). The PSA, however, have a NF of 1/2 (−3 dB) if only the signal wave is considered and the idler contains a conjugate signal copy. This comes from the 6 dB difference in gain between PIA and PSA as we saw above and ultimately from the coherent superposition. This means that a PSA and a PIA giving the same gain will have ASE noise floors that differ by 6 dB, as shown in the measured optical spectrum in **Figure 2**. More detailed derivations based on the semi-classical approach can be found in [25].

5.2. Quantum theory

A full noise theory for the PSA must be based on quantum mechanics, and we sketch a derivation here [26]. In quantum field theory, the two quadratures of a mode are described by operators $a_{1,2}$ that must obey the commutator relation $[a_1, a_2] = i/2$. The commutation between two operators implies a Heisenberg uncertainty relation between the two modes. A linear amplifier with gain $G_{1,2}$ for the respective quadratures is described by

$$b_1 = \sqrt{G_1}a_1 + F_1 \tag{19}$$

$$b_2 = \sqrt{G_2}a_2 + F_2 \tag{20}$$

where the added noise field operators $F_{1,2}$ are necessary if the commutation relation should hold also for the output modes $b_{1,2}$. It is easy to see that the absence of these noise fields would lead to contradictions, e.g., arbitrarily small uncertainties violating the Heisenberg uncertainty relation. Thus, every amplifier must have these additive fields. Applying the commutation relation to the output fields gives a relation on the noise field operators as

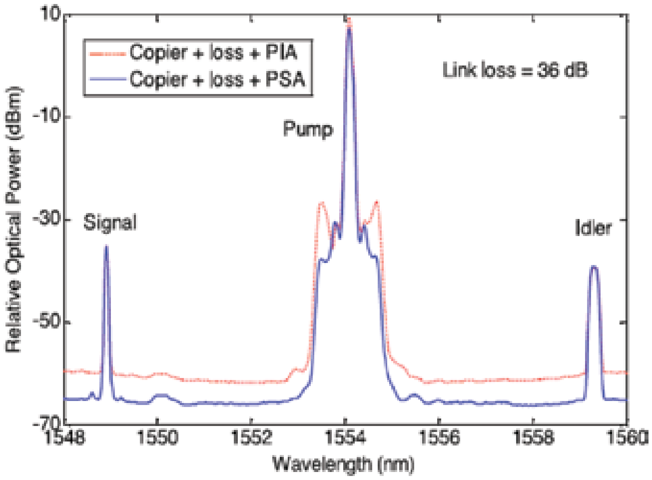

Figure 2. Optical spectra of a 2-mode parametric amplifier in PS and PI modes. The pump in the PI case is higher to make the gain equal, which leads to 6 dB higher noise floor for the PIA [25]. The increased noise close to the pumps for the PIA is likely due to dispersion variations along the HNLF, making these frequencies phase matched and having higher gain in some portions of the fiber.

$$[F_1, F_2] = \frac{i}{2}\left(1 - \sqrt{G_1 G_2}\right) \tag{21}$$

The Robertson uncertainty relation states that if two operators commute with a commutator x, their uncertainty product is $|x|^2$. The uncertainty for $F_{1,2}$ is then

$$\left\langle \Delta F_1^2 \Delta F_2^2 \right\rangle = \frac{1}{4}\left(1 - \sqrt{G_1 G_2}\right)^2 \tag{22}$$

The noise figure is then

$$\begin{aligned} NF_{PSA} &= \frac{\left\langle a_1^2\right\rangle\left\langle a_2^2\right\rangle}{\left\langle \Delta a_1^2\right\rangle\left\langle \Delta a_2^2\right\rangle}\frac{\left\langle \Delta b_1^2\right\rangle\left\langle \Delta b_2^2\right\rangle}{\left\langle b_1^2\right\rangle\left\langle b_1^2\right\rangle} \\ &= 1 + \frac{\left\langle \Delta F_1^2 \Delta F_2^2\right\rangle\left\langle \Delta b_2^2\right\rangle}{G_1 G_2\left\langle \Delta a_1^2\right\rangle\left\langle \Delta a_2^2\right\rangle} \\ &= 1 + \left(1 - \frac{1}{\sqrt{G_1 G_2}}\right)^2 \end{aligned} \tag{23}$$

For a PSA, the two quadratures' gain obey $G_1 G_2 = 1$, and this then reduces to $NF_{PSA} = 1$. For the PIA, $G_1 = G_2 = G$, and the derivation can be simplified by noting that the gain is the same for both quadratures, so that

$$NF_{PIA} = 1 + \frac{\left\langle \Delta F^2\right\rangle}{G\left\langle \Delta a^2\right\rangle} = 1 + \left(1 - \frac{1}{G}\right) = 2 - \frac{1}{G} \tag{24}$$

This summarizes the well-known properties of the noise figures for amplifiers. More detailed discussions on the quantum mechanical properties of parametric processes (including, for example, the noise for the phase conjugation and Bragg scattering processes) can be found in the works of McKinstrie [10, 11].

It should also be mentioned that other noise sources than the fundamental quantum noise discussed above contribute to parametric amplifiers, e.g., noise from the Raman effect, pump-induced noise, and excess ASE noise from the pump boosters which can make it difficult to get closer than 1 dB within the quantum noise figure limit in experiments.

6. Several kinds of parametric amplifiers

6.1. Basic setup

The most convenient PAs for use at communication wavelengths are based on nonlinear interferometers (NIs) or operate directly in fiber through partially degenerate FWM, which are listed in **Figures 3** and **4** [27, 28].

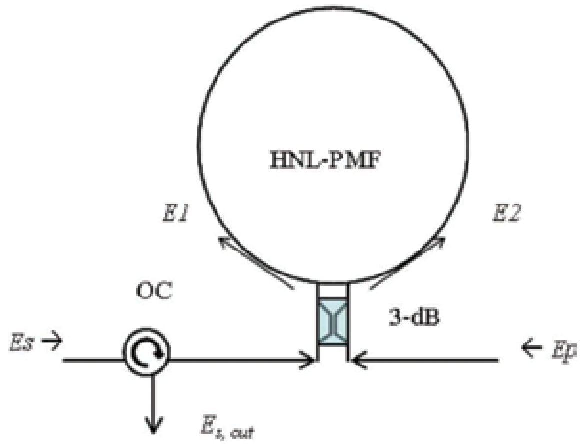

Figure 3. NI-PSA based on a Sagnac interferometer and optical fiber. OC: optical circulator; PC: PM/AM: noise adding phase and amplitude modulators.

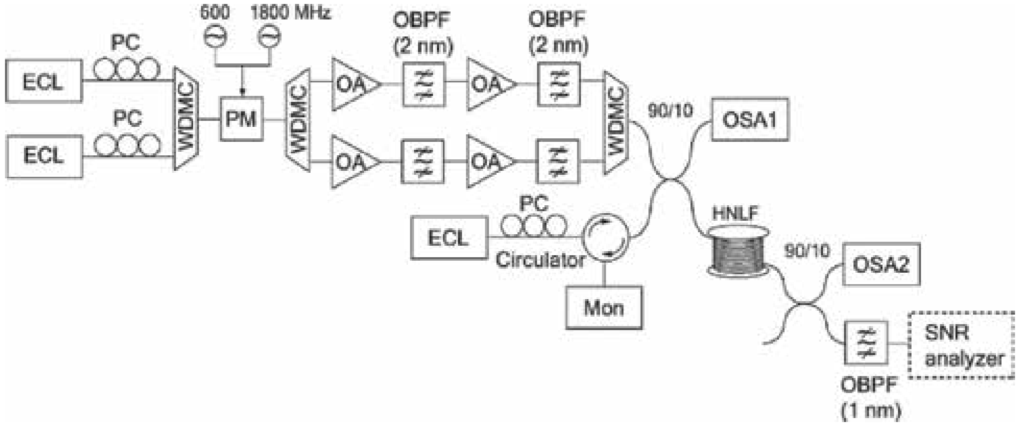

Figure 4. Setup of parametric amplification. ECL: external cavity laser, PC: polarization controller, WDMC: wavelength division multiplexing coupler, PM: phase modulator, OA: optical amplifier, OBPF: optical bandpass filter, OSA: optical spectrum analyzer, HNLF: highly nonlinear fiber, and Mon: optical power monitor.

An example of a Sagnac interferometer is depicted in **Figure 3**. Phase sensitivity of the gain arises from the interference of the waves at the input and output combined with nonlinear phase shifts due to SPM [27].

A 2-pump PA with a gain bandwidth of approximately 25 nm is shown in **Figure 4**. A method based on lock-in amplification is used. The two pumps (wavelengths λ_C = 1563 nm and λ_L = 1600 nm) are placed roughly symmetrically around the zero-dispersion wavelength, λ_0 = 1582 nm. The length of HNLF is L = 520 m and nonlinearity parameter is $\gamma \approx$ 16/W/km. The pump powers are provided by external cavity lasers (ECLs), combined with low-loss wavelength division multiplexing couplers (WDMCs) and sent into a phase modulator (PM). Two radio frequencies (RFs) 600 and 1800 MHz are sent to the PM to reduce the SBS. The high frequencies of the PM are necessary because the PM produces gain fluctuations, which create discrete frequency harmonics in the electrical spectrum of the detected signal. The two pumps are combined after the PM and amplified by two erbium-doped fiber amplifiers (EDFAs). The pumps are then filtered and boosted by high-power EDFAs, and filtered again by 2 nm optical bandpass filters (OBPFs). They are finally combined with the signal and launched into the HNLF. An optical spectrum analyzer (OSA) monitored the input powers of the signal and pumps. Another OSA monitors the output powers. The signal is filtered by an OBPF before sent to the SNR analyzer.

6.2. Optical parametric chirped-pulse amplifier system

Optical parametric chirped-pulse amplification (OPCPA) is an efficient way to amplify short optical pulses to high-power levels while avoiding some of the pitfalls of conventional CPA systems, specifically, gain narrowing, unwanted nonlinearities, and thermal effects [29].

The system includes the 1.064 μm pump laser, the tunable 1.6 μm fiber seed laser, the timing electronics setups, the rubidium titanyl phosphate (RTP) and potassium titanyl arsenate (KTA) (as the OPA crystals), and the stretcher and compressor. The timing circuitry is used to lock the phase of the two seed oscillators.

The layout of the system is shown in **Figure 5**. A 40 MHz fiber laser and amplifier provide the signal pulse and act as the master clock for the system. The custom-built fiber system is based on the design given in [30]. The short pulse (<100 fs) is used as a signal source that can tune the OPCPA across the range from 1500 to 1650 nm. These pulses are stretched to 300 ps in a stretcher (a 600 line/mm grating); however, due to the bandwidth limitations in the OPA

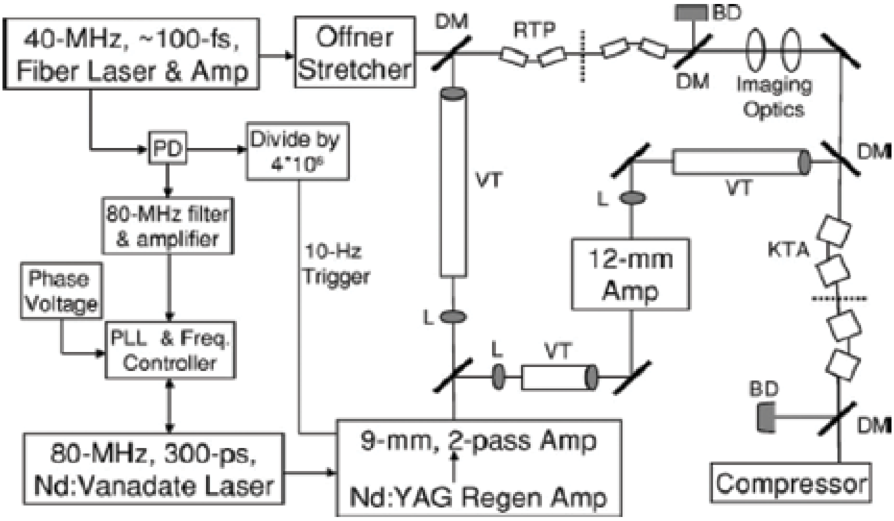

Figure 5. The system's optical and electric control layout. Dotted lines are image planes for the relay. RTP and KTA are the nonlinear crystals. VT, vacuum tubes; L, relay imaging lens; PD, photodiode; DM, dichroic mirror; and BD, beam dump.

crystals (only 10–20 nm are amplified). This reduced the bandwidth of the pulse (stretched only 30–60 ps).

The 40 MHz photodiode signal generated the 80 MHz harmonic, then filtered, and amplified the input of the phase-locked loop (PLL) to stabilize the 80 MHz pump seed laser. The seed laser is a 300 ps mode-locked Nd:vanadate laser that uses a semiconductor saturable absorber and mirror mode locker. The cavity length is controlled by a motor to maintain the repetition rate and to rapidly compensate the mechanical instabilities. The laser and locker reduce the relative timing jitter between the two lasers (<2 ps rms over the 1–100 kHz frequency range), and the piezo inducing jitter (<1 ps rms for frequencies less than 1 kHz). By employing this timing stabilization technique, the OPCPA has the ability to accept any signal that its repetition rate is some integer fraction of the 80 MHz pump laser. Once the two lasers are frequency locked, the relative phase shift between the pump and the signal pulses is set to within ±1 ns by inserting the proper electrical equipment between the 80 MHz clock signal and the PLL. The phase voltage can adjust the relative phase of the pulses at a rate of 60 ps/V. As shown in **Figure 8**, a separate output from the photodiode is transferred to 10 Hz by the standard digital electronics and then acts as the trigger for both the flash lamps and the Pockels cells in the Nd: YAG amplifier chain.

The first stage of this chain is a regeneration amplifier (the 10 nJ seed pulse to 40 mJ). The output is then collimated and amplified to 375 mJ in Nd:YAG and two-pass power amplifiers.

A software is designed to model nonlinear optical interactions. The 1.6 μm broadband light is amplified by a 1.064 μm monochromatic pump in a collinear configuration. Both crystals, RTP and KTA, have broad phase-matched bandwidths in the 1.5–1.6 μm region when used in a collinear geometry, and each has a d_{eff} between 2 and 2.5 pm/V for the optical parametric amplification process. The system uses four 5 × 5 × 6 mm RTP crystals as the preamplifiers since its bandwidth and gain are superior to KTA; however, RTP absorbs 25% of the idler energy and its aperture cannot be manufactured large enough to act as a power amplifier. For these reasons, four 8 × 8 × 8 KTA crystals are used as the power amplifiers. The spatial walk-off between the signal and the pump beams is compensated. The four-crystal arrangement provides uniform gain across the signal beam.

6.3. Tunable single-longitudinal mode fiber optical parametric oscillator (SLM FOPO)

A sub-ring cavity with a short length is used to suppress the longitudinal modes and broaden the longitudinal mode spacing [31]. A fiber loop mirror, consisted of an unpumped erbium-doped fiber, acts as an auto-tracking filter to ensure the single frequency operation. The measurement shows that the FOPO has the SLM output. It can be tunable over 14 nm for each of the signal and idler, which is limited only by the gain bandwidth of parametric amplifier.

In **Figure 6**, the pump is seeded by an external cavity tunable laser source (TLS) at the wavelength 1556 nm. To suppress the stimulated SBS, the light from the TLS is modulated with a 10 Gb/s pseudorandom bit sequence signal via a phase modulator (PM). A polarization controller PC1 aligns the polarization state of pump with the axis of the PM. The SBS can be suppressed up to 28 dB. Then the pump is amplified by a two stage EDFA, in which the first

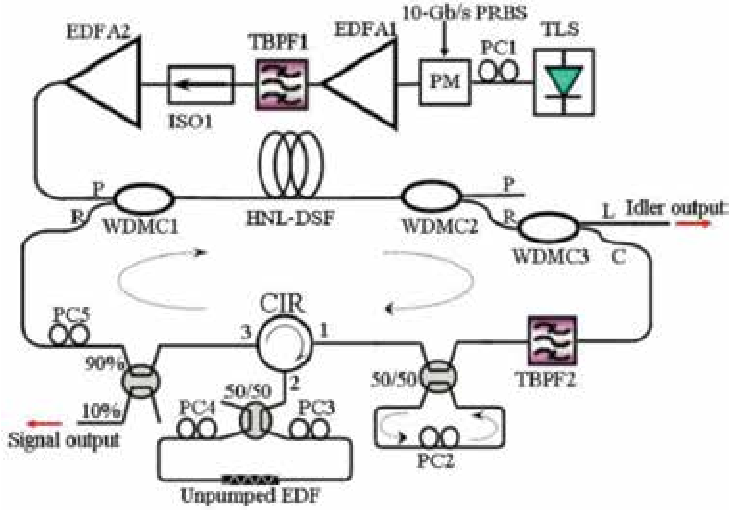

Figure 6. Schematic diagram of the tunable SLM FOPO.

stage (EDFA1) provides small signal gain to prevent self-saturation. The 0.35 nm tunable bandpass filter (TBPF1) is used to reduce the ASE noise. After passing through an isolator (ISO1), the pump is further amplified by the second stage (EDFA2), with a maximum output power of 33 dBm. Then the pump is coupled into a 400 m highly nonlinear dispersion-shifted fiber (HNL-DSF) with the zero-dispersion wavelength at 1554 nm via the P-port (transmission band: 1554.89–1563.89 nm) of a WDM coupler (WDMC1). The high-power pump is then rejected through the P-port of another WDMC2, while the amplified signal and idler propagate first through the R-port (reflection bands: 1500–1551 and 1567–1620 nm) of WDMC2 and subsequently are split into two paths by a C/L band WDMC3. Only the signal is coupled into the cavity and can oscillate, while the idler is coupled out through the L-port of WDMC3. The signal from the C-port of WDMC3 is filtered by 0.35 nm TBPF2, which determines the lasing wavelength and the possible oscillation modes. The cavity with length about 4.1 m is then inserted after TBPF2. It consists of a PC and a 50/50 coupler. Subsequently, a fiber loop mirror is linked via an optical circulator. The loop mirror consists of a 50/50 coupler, two PCs (PC3 and PC4), and a 3.5 m unpumped EDF that serves as the saturable absorber. The two in-line PCs (PC3 and PC4) are used to control the polarization state of the light. A 10/90 optical coupler is used to couple out 10% of the signal light. PC5 is used to align the polarization of the signal with the pump so as to maximize the signal gain.

The resonant frequencies of the ring cavities are obtained by making the total phase shift along the ring path equals an integral multiple of 2π. The longitudinal mode spacing is $\Delta v = c/nL$, in which c is the light speed in vacuum, n is the refractive index of the ring, and L is the cavity length. So the longitudinal mode spacing is the inverse ratio of the cavity length. To suppress the longitudinal modes and increase the longitudinal mode spacing, a coupled sub-ring cavity with a short cavity length is deployed as a mode filter. The longitudinal mode spacing can be increased from kilo-Hz level to mega-Hz level by this method. The second mechanism is a fiber loop mirror with an unpumped EDF. In the fiber loop mirror, two counter-propagating waves form a standing wave and induce spatial hole burning (SHB) in the unpumped EDF. The refraction index of the EDF changes spatially and results in an ultra-narrow bandwidth self-induced fiber Bragg grating (FBG). After the fiber loop mirror, only SLM can be transmitted and oscillated.

7. The copier-phase-sensitive amplifier

A powerful way to realize a PSA transmission link is to generate the idler wave in a parametric amplifier as a "copier" [32, 33] as shown in **Figure 7**. Then the pump, signal and idler waves will be automatically phase locked. This means that an arbitrary modulated signal can be phase-sensitively amplified along the link if all three waves are transmitted, and also, that several signal wavelengths can be used with their corresponding idlers and pump. Three channels with QPSK modulation are amplified by a 20 dB PSA using this scheme.

7.1. Sensitivity improvement

In order to obtain the 6 dB of SNR improvement for the copier-PSA scheme, it is important that the noise at the signal and idler wavelengths are uncorrelated [33], which is accomplished by the attenuation after the copier. The end result is, however, that the copier-PSA link gets a 4-fold increase of the transmission distance, at the expense of using twice the bandwidth, as the same data occupies both the signal and the idler wavelengths [34].

7.2. Nonlinear compensation

The copier-PSA scheme has one additional, somewhat unexpected, benefit over schemes that does not co-transmit a conjugated idler wave. That is, its ability to compensate nonlinear distortions from, e.g., self-phase modulation or nonlinear phase noise. The principle is similar to the so-called phase-conjugated twin waves [35], where the idea is to transmit the data and the conjugate data on two parallel channels.

When the two channels are superposed in digital signal processing, the nonlinear distortions will cancel out (to first order). In the copier-PSA scheme, the exact same superposition takes

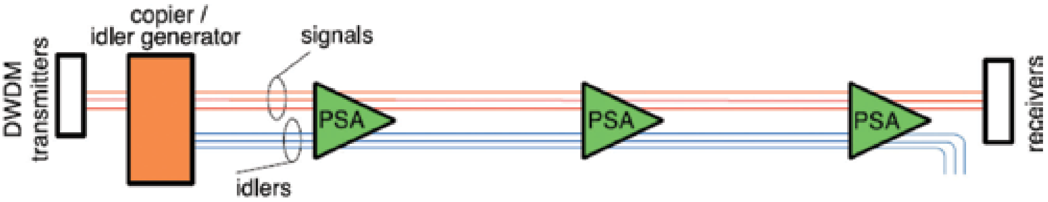

Figure 7. Transmission system based on the copier-PSA scheme. A copier (a PI parametric amplifier) directly after the transmitter generates idler waves that are conjugated versions of the signals. The idlers are only used as internal modes and dropped before detection.

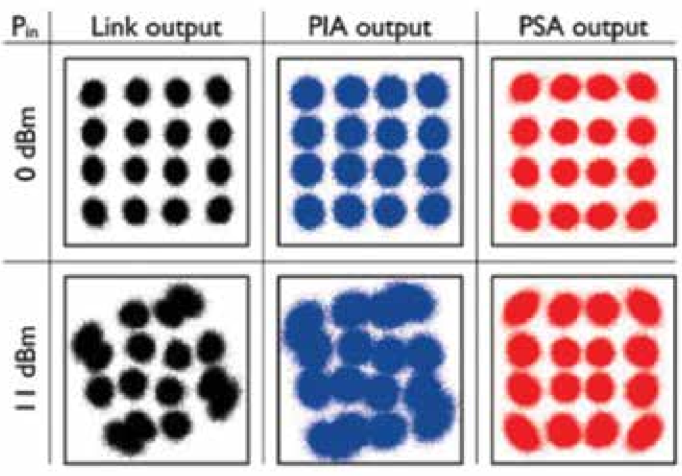

Figure 8. Linear (upper row) and nonlinear (lower row) transmission of 16-QAM data through a link and after amplification with PIA or PSA.

place in the PSA and significant nonlinear suppression can be seen. An example of a measured 16-quardrature amplitude modulation (QAM) constellation is shown in **Figure 8**.

7.3. Experimental system

The experimental setup is shown in **Figure 10** [36]. A continuous wave laser (200 kHz linewidth) at 1549.5 nm is modulated by 10 GBd 16QAM data in an IQ-modulator and then combined with a 28 dBm CW pump at 1553.7 nm in a WDM coupler.

The waves are launched into the copier (HNLF) and the net conversion efficiency is about −5 dB. An idler wave is generated at 1557.5 nm. The pump wave is then attenuated for 4 dBm power in the variable optical attenuator (VOA), VOA1, and passes through an optical delay line for equalization of the optical path between the copier and the PSA. The signal and idler waves pass through an optical processor for delay and amplitude tuning. The waves are tuned so that they have the same timing and amplitude at the PSA input. The optical processor is also used for switching between phase-insensitive (PI) and PS operation by either blocking or letting through the idler wave.

After re-combining the three waves, they are launched into a DCF for pre-compensation (dispersion is equivalent to 23.6 km of SSMF). The powers launched into the DCF are below 0 dBm for both the signal and the idler while the pump power is about 5 dBm.

The signal and idler waves are then amplified by EDFA2 and attenuated by VOA2. The signal launch power is measured at point P_{in} in **Figure 9**. The link consists of 105 km SSMF and a fiber Bragg-grating dispersion-compensating module (FBG-DCM) for the dispersion compensation. The total link loss is 30 dB, and the dispersion map is chosen for the optimum of efficient nonlinearity mitigation found for 10 GBd QPSK data.

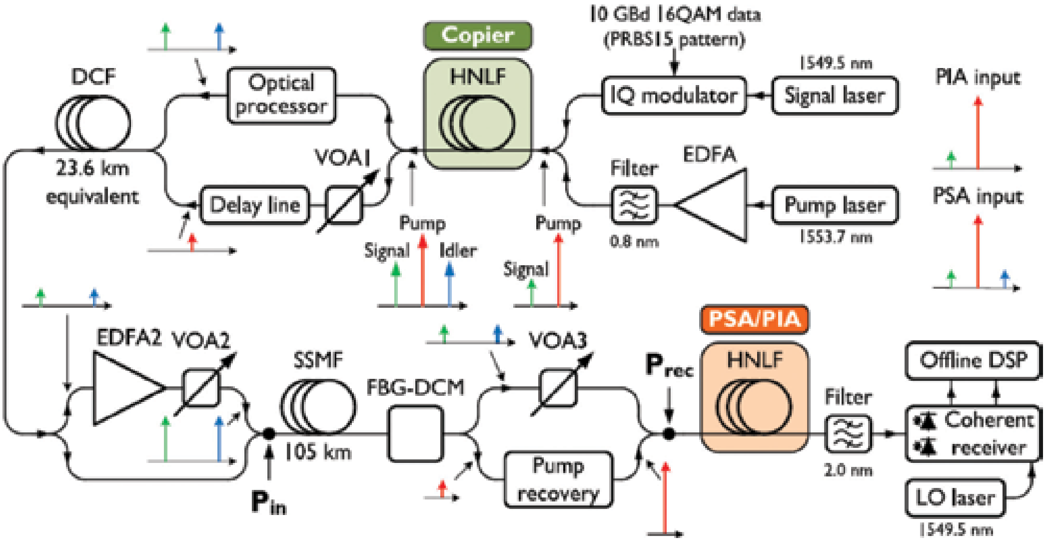

Figure 9. Experimental setup for simultaneous sensitivity improvement and nonlinearity mitigation in a 1 GBd 16QAM link. VOA: variable optical attenuator, FBG-DCM: fiber Bragg-grating dispersion-compensating module, PSA: phase-sensitive amplifier, PIA: phase-insensitive amplifier, LO: local oscillator, and DSP: digital signal processing.

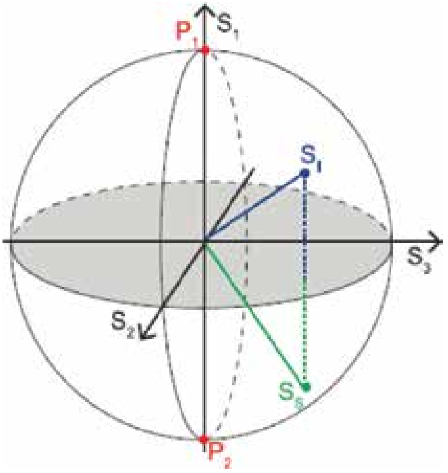

Figure 10. Polarization states on Poincaré sphere for vector PSA interaction. $S_{i,s}$ denote signal and idler Stokes vectors, and P_1 and P_2 are the pump Stokes vectors. S_s and S_i are mirrored in the plane (gray) normal to the pumps.

After the link, the pump wave is recovered by a hybrid EDFA/injection-locking system, before launched into the PIA/PSA. The pump recovery includes a PLL to stabilize the relative phase between the pump and the signal and idler. This is against thermal drift and acoustic noise introduced by splitting the pump and the signal and idler in different paths. The received signal power is varied using VOA3 and measured at point P_{rec}. Only the signal power is accounted when measuring launch power at P_{in} and received power at P_{rec}. The PIA/PSA

FOPA is implemented with a cascade of four HNLFs and provides 19 dB net gain in PS-mode and 13.5 dB net gain in PI mode.

The amplified signal is then filtered and passed to a preamplified coherent receiver, where it is mixed with a 300 kHz linewidth local oscillator laser at 1549.5 nm.

The same DD-LMS-based DSP is used to process the output from the numerical simulations with 16QAM. However, in this case, FFT-based frequency offset estimation in the DD-LMS loop is also adopted.

7.4. Polarization properties

In most applications of the copier-PSA the pump, signal and idler polarizations are aligned, and a scalar theory used. In a vector PSA, however, the polarization properties are important. The most common scheme for vector PSAs is the non-degenerate pump scheme, where the two pump waves are orthogonally polarized. An obvious question then is: what will the idler state of polarization (SOP) be, if the pumps and signal SOPs are given? The answer can be understood from the classical scatter-from-gratings picture.

Then the idler is given by two processes: pump 1 interferes with the signal and scatters pump 2 and vice versa. In terms of Jones vectors, the idler SOP will be given by

$$J_i = \left(J_s^H J_{p1}\right) J_{p2} + \left(J_s^H J_{p2}\right) J_{p1} \tag{25}$$

where $J_{p1,p2}, s, i$ are the four Jones vectors and H denotes conjugate transpose. In matrix form, one can write $J_i^* = A^* J_s$, where the matrix is given by

$$A = J_{p1}^t J_{p2} + J_{p2}^t J_{p1} \tag{26}$$

The transfer matrix for vector PSA interaction then generalizes to

$$\begin{pmatrix} J_s \\ J_i^* \end{pmatrix}_{out} = \begin{pmatrix} \mu & \nu A \\ \nu^* A^* & \mu^* \end{pmatrix} \begin{pmatrix} J_s \\ J_i^* \end{pmatrix}_{in} \tag{27}$$

The geometrical interpretation of this scattering is shown on the Poincaré sphere (in Stokes space) in **Figure 10**. The orthogonally polarized pumps (antiparallel in Stokes space) are normal to a surface in which the signal and idler SOPs are mirrored. This generalizes a theory of Marhic [37], who considered the special case, $J_{p1} = (1, 0)t$ and $J_{p2} = (0, 1)t$. Note that the signal and idler are orthogonal to each other only when they are copolarized with the pumps, but not in the general case, which is a common misconception.

To conclude this subsection: for given orthogonal pumps and signal SOPs, the generated idler SOP will be the signal mirrored in plane normal to the pumps. This set of SOPs is generated in the copier. Then, for phase-sensitive interaction (coherent superposition) to take place, the signal, idler, and pump SOPs in to the PSA must be aligned as shown in **Figure 10**. Only the relative orientation matter, so any polarization mode dispersion (PMD) that changes the relative SOPs of the four waves will reduce the phase-sensitive interaction, and must be compensated.

7.5. Transmission experiments

In practical implementations, the copier-PSA scheme is challenging as it requires full phase synchronization at each amplifier in the link, which require per-span dispersion compensation and phase tracking. Also, the polarization states need to be aligned. The pump needs to be transmitted together with the signal and idler, but must be selectively attenuated before sent in to the fiber. Then at the PSA, it must be recovered, amplified, and used as an intense pump in the PSA. This pump recovery scheme can be solved by injection locking. The first transmission experiment using a copier-PSA to implement these ideas was reported by Corcoran et al., who demonstrated transmission over a single 80 km span link [38].

In the same timeframe, Umeki et al. also reported transmission experiment using PSAs, but then using a periodically poled Lithium-Niobate PSA [39, 40]. That work is very different and not based on the copier-PSA idea. Rather the PSA is $\chi^{(2)}$-based, which illustrates that this scheme can (in contrast with the copier-PSA scheme) only amplify a single quadrature. On the other hand, it does not require the bandwidth of the copropagating idler wave. This work was also extended to cover polarization division multiplexed transmission [41].

The copier-PSA scheme was extended to a full circulating loop experiment by Olsson [42] demonstrating transmission over 3400 km. It should be noted that the first recirculating loop experiment, based on high-gain PSAs and the copier-PSA configuration, increased transmission distance of around four times compared to a PIA-based link. The possibility of tolerating a nonlinear phase shift at a BER of 10^{-3} is 5.8 radians, making it to be one of the most nonlinear transmission experiments ever performed, while also demonstrating the potential of the PSA-based links.

The PSA also demonstrates the highest sensitivity reported in [43] for 10 Gb/s OOK data, reaching a sensitivity of -41.7 dBm for a BER = 10^{-9}.

8. Applications of parametric amplifier

8.1. Phase-sensitive amplification for phase and amplitude regeneration of differential phase-shift keyed signals

PSAs offer numerous advantages in optical communications. It offers stronger phase-matched gain and suppression of amplitude-to-phase noise conversion. Squeezing of optical phase through PSA can remove accumulated phase jitter. Different implementations of PSA were used for phase regeneration of both return-to-zero differential phase-shift keying and nonreturn-to-zero differential phase-shift keying data.

Ideally, a PSA can be configured to squeeze either the phase or the amplitude of a signal. For PSK systems, the former is chosen, and amplitude regeneration follows from the different physical phenomenon of gain saturation. The orientation of the squeezing axis in phase regeneration should satisfy the synchronization of the pump and signal carrier phases, as shown in **Figure 11(a)**. A practical PSA operates as follows: the incident (noisy) signal is divided for processing and for the generation of pumps; owing to the carrier-suppressed nature of PSK formats, it is impossible to directly inject and lock a local laser to the signal frequency or to use straight forward phase-locked loops; and an optical carrier is derived from the signal through alternate means such as a decision-directed phase-locked loop.

An alternative method is to perform all optical carrier-phase and polarization recovery (CPPR). The process was recently demonstrated by using a PSA in an oscillator configuration. The resulting carrier can be used for injection locking (IL), as a local oscillator at the signal frequency. Owing to the PSA implementation, the resulting wave is amplified (by an NI-PSA) or modulated to produce sidebands (in a PSA based on FWM). The clock-recovery (CR) process can be implemented parallelly with CPPR. Phase stabilization is required when the signal and pump(s) are injected into the PSA. By properly orienting the axes, the maximum amplification is obtained.

A Sagnac PSA is configured in **Figure 12**. Ten gigabits per second RZ-DPSK data with 33% duty cycle and pattern length of at least 2^{11}–1 is generated and divided into pump and signal

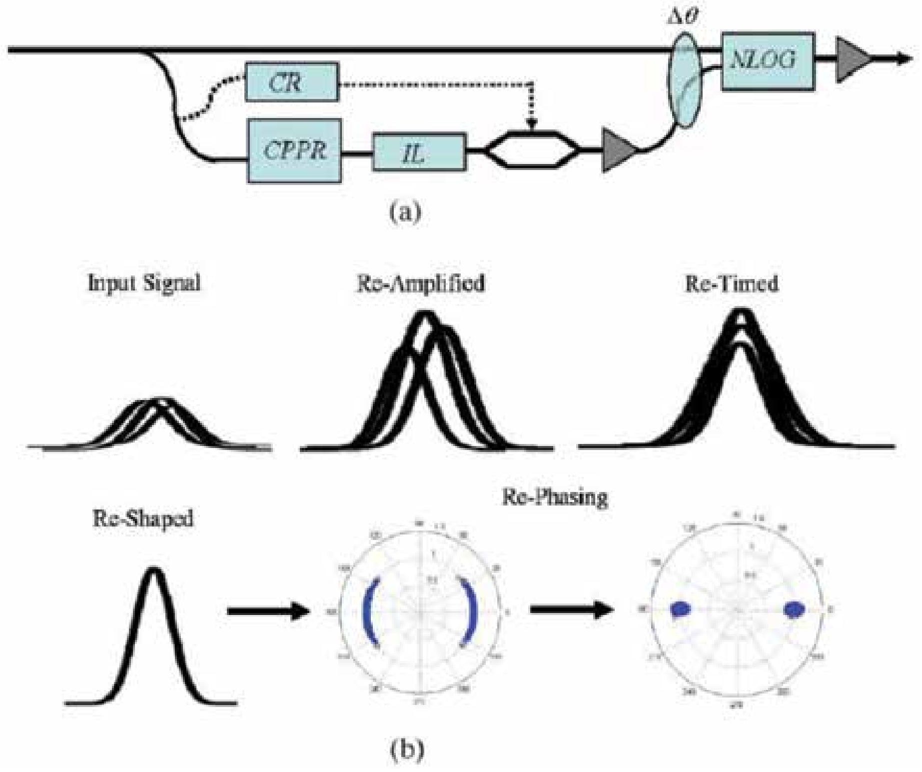

Figure 11. Regeneration of a DPSK signal. (a) Schematic of practical PSA. (b) Aspects of all-optical regeneration for DPSK. NLOG: nonlinear optical gate.

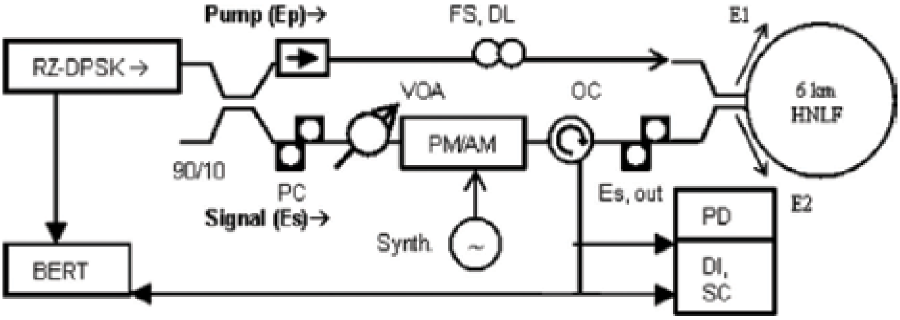

Figure 12. RZ-DPSK regeneration. FS: fiber stretcher; DL: delay line; OC: optical circulator; PC: polarization controller; DI: delay interferometer; SC: sampling oscilloscope; Synth: synthesizer; BERT: bit-error-ratio tester; PM/AM: noise adding phase and amplitude modulators.

paths. The use of a binary-phase-modulated pump can eliminate excess noise due to SBS. Different path lengths of the pump and signal ensure decorrelation of the PRBS data. The PN is quantified according to the maximum phase error, where MPE = $\max(\varphi_{n-1} - \varphi_n)$ is the maximum deviation of all detected differential phases from their original encoded values. An optical attenuator is used to adjust the pump to signal power ratio from 10 to 20 dB at the input. A free-space delay line in the pump path allows temporal alignment of the pump and signal pulses at the PSA input as well as a method for manually controlling the input phase difference. The input phase difference is stabilized by monitoring the signal gain and driving a fiber stretcher. The PSA comprises a 3 dB coupler and 6058 m HCF (not polarization maintaining) with a total insertion loss of 5 dB and effective nonlinear coefficient of 9.75/W/km. An intra-loop polarization controller is required to maximize the reflection of the pump and the transmission of the regenerated signal extracted by the optical circulator.

Several factors affect the ability of the PSA to simultaneously reduce phase and amplitude fluctuations. Performance is optimized when the average nonlinear phase shift NLPS = $\pi/2$ and the pump power is maximized, allowing the signal launch power to be minimized. In experiments, lower limits are placed on the launched signal power. Imperfections of the coupler in the PSA lead to leakage of pump. After PSA, the signal power significantly exceeds the leakage of the pump. Pump leakage increases when the intra-loop polarization controller is not adjusted properly. Due to thermal effect in the fiber, frequent adjustment of the controller is required, especially when the pumping power is changed. This problem is exacerbated when the fiber length is >6 km. And in this case, it is not polarization maintaining. Restrictions by these factors are easily removed through proper choice of components. Further restrictions resulting from pump wave imperfections is quantified in following results. To obtain the condition of NLPS = $\pi/2$, the phase-sensitive gain (PSG) at the signal port is monitored.

In **Figure 13**, light from a single tunable laser is divided into two paths for generations of pumps and a degraded signal. The signal is modulated with 10 Gb/s NRZ-DPSK data and the pattern length at least 2^{15}–1 using a phase modulator. For regeneration experiments, nonlinear phase noise and amplitude fluctuations are simulated in previous experiments. Pump waves symmetrically around the signal frequency are generated with a carrier-suppressed return-to-

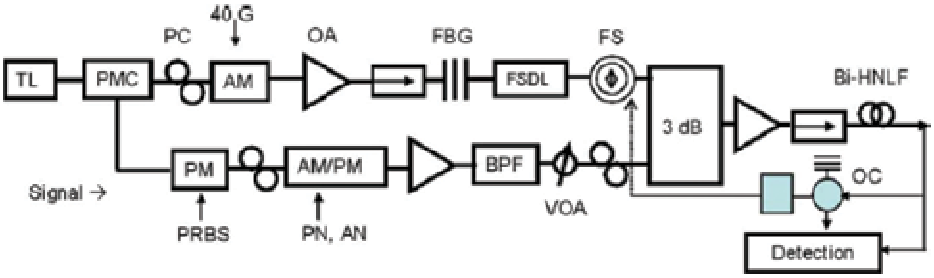

Figure 13. Experiment for NRZ-DPSK phase regeneration. TL: tunable laser; PMC: polarization maintaining coupler; OA: EDFA; FSDL: free-space delay line; FS: fiber stretcher; BPF: bandpass filter; Bi-HNLF: bismuth-oxide highly nonlinear fiber; and FBG: fiber Bragg grating.

zero (CSRZ) modulation. Experiments are performed with driving frequencies 20 and 40 GHz. The sideband separation is twice the driving frequency of the modulator, while power at the carrier frequency is typically 23 dB below that of either sideband. A FBG is used to further suppress light at the carrier frequency in the pump path to −38 dB and to minimize interference in the DPSK signal when the waves are mixed.

Both the pumps and signal are amplified by a high-power EDFA and launched into a bismuth-oxide-based optical fiber. Due to the short length, the total launch power is 31 dBm without the pump phase modulation to suppress SBS. This leads to the improvement of the performance since pump wave imperfections are minimized. The output signal is filtered and divided for feedback control and detection. Phase stabilization is achieved. The polarizations of input waves are aligned by scanning the signal phase (using a delay line) and simultaneously adjusting the polarization controller which also maximizes phase-sensitive gain. Careful adjustment allows polarization alignment but not gain an arbitrary polarization state: to obtain maximize performance, parallel linear polarizations should be adopted.

8.2. Parametric amplifier for squeezed state generation

A considerable degree of two mode broadband squeezing by combining two coherent strongly pumped single-pass type-I OPAs, which generate squeezed vacua in two orthogonal polarization modes is shown in **Figure 14** [44]. This creates a squeezed vacuum with the variance of some Stokes suppressed below the shot-noise level, which is determined by the mean number of photons. The latter, coinciding with the zeroth Stokes parameter S_0, gives the variance of any Stokes of a coherent beam with the same mean photon number and with any polarization. This special two-mode squeezing is often termed polarization squeezing, and the state is called polarization-squeezed vacuum. This definition of polarization squeezing differs from the commonly used one [45], where the modulus of some Stokes observable mean value is $Var(S_i) < \left|\langle S_j \rangle\right| < Var(S_k), \ \ i, j, k = 1, 2, 3$. This polarization squeezing is similar to quadrature squeezing rather than two mode squeezing. However, both are essentially non-classical.

In **Figure 14**, two 1 mm BBO crystals with the optical axes oriented in the vertical and horizontal planes are placed to induce the beam of a Nd:YAG laser third harmonic (wavelength $\lambda_p = 355$ nm).

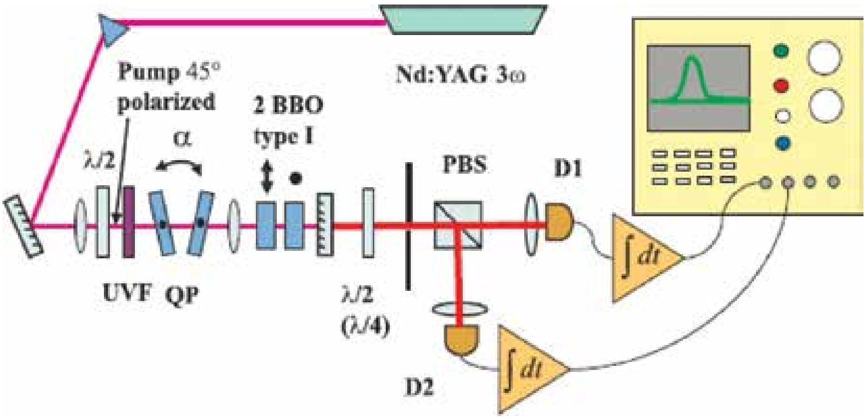

Figure 14. Experimental setup. UVF, UV filter; QP, quartz plates; PBS, polarizing beam splitter; and D1 and D2, detectors.

The fundamental and second-harmonic radiation of the laser is eliminated using a prism and a UV filter. The pump pulse width is 17 ps, the repetition rate is 1 kHz, and the mean power is up to 120 mW. The pump is focused into the crystals by either a lens with focal length 100 cm, which results in a beam waist of 70 μm, or with a telescope, providing a softer focusing (beam waist about 500 μm). Using a half wave plate (HWP), the pump polarization is aligned to be at 45° to the planes of the crystals' optical axes. The crystals are aligned for type-I collinear frequency-degenerate phase matching. After the crystals, the pump radiation is cut off by two dichroic mirrors with high reflection for the pump and 98.5% transmission for down-converted radiation.

The detection part includes a polarizing beam splitter, a HWP or a quarter wave plate (QWP), and two detectors and provides a standard Stokes measurement. With a HWP oriented at 22.5°, the difference of the detectors' signals corresponded to the second Stokes is S_2, while with a QWP oriented at 45°, the same measurement is S_3. All surfaces of the optical elements had a standard broadband antireflection coating. The angular spectrum of the detected light is restricted by an aperture to be 0.8°, and the wavelength range is only restricted by the phase matching and is 130 nm broad with the central wavelength 709 nm. The detectors are Hamamatsu S3883 *p-i-n* diodes and the pulsed charge-sensitive amplifiers are Amptek A250 and A275 chips, with peaking time 2.77 μs. They have a quantum efficiency of 90% and an electronic noise of 180 electrons/pulse rms. At the outputs, they produced pulses with the duration 8 μs and the amplitude proportional to the integral number of photons per light pulse. The phase between the states generated in the two crystals can be adjusted by tilting two quartz plates (l_1 = 532 μm and l_1 = 523 μm), which are placed in the pump beam path and having the optical axes oriented vertically.

The output of the detectors is measured by means of an analog-digital card integrating the electronic pulses over time. The resulting integrals (up to the amplification factor A) coincide with the photon numbers incidented on the detectors during a light pulse. The amplification factors for detectors 1 and 2 are independently calibrated to be $A_1 = 9.96 \times 10^{-3}$ nV s/photon and $A_2 = 9.96 \times 10^{-3}$ nV s/photon. The difference between the amplification factors is eliminated numerically by multiplying the result of the measurement of detector 2 by a factor of

0.9–0.92, depending on the alignment. As a result, the output signals of the detectors are balanced to an accuracy of 0.1%. From the data set obtained from 30,000 pulses, the mean photon numbers per pulse are measured as well as the variances of the photon number difference and photon-number sum for the two detectors. Since the electronic noise is comparable to the shot-noise level, it has to be subtracted. The shot-noise is measured independently by using a shot-noise limited source and corresponds to a standard deviation of about 250 photons per pulse. The degree of two-mode squeezing is characterized by the noise reduction factor (NRF), the ratio of the photon-number difference variance to the mean photon-number sum.

9. Conclusion

By introducing the basic transmission theory of pump and signal lights in fibers, the principle of PA is interrupted which includes the properties of phase sensitivity, gain saturation, and noise. The systems for the parametric amplification, the Sagnac interferometer and directly generation in HNLF, are presented. Its applications for phase and amplitude regeneration of differential phase-shift keyed signals and for the generation of squeezed state are also introduced.

As the transmission system has to accommodate all types of modulation formats, the field of PA investigation attracts much attention again and it is worth paying more attention in the future.

Author details

Jing Huang

Address all correspondence to: huanggesheng@tom.com

Physics Department, South China University of Technology, Guangzhou, China

References

[1] Karlsson M. Transmission systems with low noise phase-sensitive parametric amplifiers. IEEE Journal of Lightwave Technology. 2016;**34**:1411-1423. DOI: 10.1109/JLT.2015.2507866

[2] Pocholle JP, Raffy J, Papuchon M, Desurvire E. Raman and four photon mixing amplification in single mode fibers. Optical Engineering. 1985;**24**:244600-244608. DOI: 10.1117/12.7973536

[3] Bar-Joseph I, Friesem AA, Waarts RG, Yaffe HH. Parametric interaction of a modulated wave in a single-mode fiber. Optics Letters. 1986;**11**:534-536. DOI: 10.1364/OL.11.000534

[4] Levenson JA, Grangier P, Abram I, Rivera T. Reduction of quantum noise in optical parametric amplification. Journal of the Optical Society of America B. 1993;**10**:2233-2238. DOI: 10.1364/JOSAB.10.002233

[5] Marhic ME, Hsia CH, Jeong JM. Optical amplification in a nonlinear fibre interferometer. Electronics Letters. 1991;**27**:210-211. DOI: 10.1049/el:19910136

[6] Imajuku W, Takada A, Yamabayashi Y. Low-noise amplification under the 3 dB noise figure in high-gain phase-sensitive fibre amplifier. Electronics Letters. 1999;**35**:1954-1955. DOI: 10.1049/el:19991343

[7] Lundstrom C, Malik R, Gruner-Nielsen L, Corcoran B, Olsson SLI, Karlsson M, Andrekson PA. Fiber optic parametric amplifier with 10-dB net gain without pump dithering. IEEE Photonics Technology Letters. 2013;**25**:234-237. DOI: 10.1109/LPT.2012.2230160

[8] Tang R, Lasri J, Devgan PS, Grigoryan V, Kumar P, Vasilyev M. Gain characteristics of a frequency nondegenerate phase-sensitive fiberoptic parametric amplifier with phase self-stabilized input. Optics Express. 2005;**13**:10483-10493. DOI: 10.1364/OPEX.13.010483

[9] McKinstrie CJ, Radic S. Phase-sensitive amplification in a fiber. Optics Express. 2004;**12**: 4973-4979. DOI: 10.1109/LEOSWT.2008.4444389

[10] McKinstrie CJ, Yu M, Raymer MG, Radic S. Quantum noise properties of parametric processes. Optics Express. 2005;**13**:4986-5012. DOI: /10.1364/OPEX.13.004986

[11] McKinstrie CJ, Raymer MG, Radic S, Vasilyev M. Quantum mechanics of phase-sensitive amplification in a fiber. Optical Communications. 2006;**257**:146-163. DOI: 10.1016/j.optcom.2005.07.023

[12] Marhic ME, Kagi N, Chiang T-K, Kazovsky LG. Broadband fiber optical parametric amplifiers. Optics Letters. 1996;**21**:573-575. DOI: 10.1364/OL.21.000573

[13] Marhic ME, Wong KK-Y, Kazovsky LG. Wide-band tuning of the gain spectra of one-pump fiber optical parametric amplifiers. IEEE Journal of Selected Topics in Quantum Electronics. 2004;**10**:1133-1141. DOI: 10.1109/JSTQE.2004.835298

[14] Marhic ME. Fiber Optical Parametric Amplifiers, Oscillators and Related Devices. Cambridge, UK: Cambridge University Press; 2008. DOI: 10.1109/jstqe.2008.920032

[15] Croussore K, Kim C, Li G. All-optical regeneration of differential phase-shift keying signals based on phase-sensitive amplification. Optics Letters. 2004;**29**:2357-2359. DOI: 10.1364/OL.29.002357

[16] Croussore K, Kim I, Han Y, Kim C, Li G, Radic S. Demonstration of phase-regeneration of DPSK signals based on phase-sensitive amplification. Optics Express. 2005;**13**:3945-3950. DOI: 10.1364/OPEX.13.003945

[17] Croussore K, Li G. Phase and amplitude regeneration of differential phase-shift keyed signals using phase-sensitive amplification. IEEE Journal of Selected Topics in Quantum Electronics. 2008;**14**:648-658. DOI: 10.1109/JSTQE.2007.915397

[18] Karlsson M. Four-wave mixing in fibers with randomly varying zero dispersion wavelength. Journal of the Optical Society of America B. 1998;**15**:2269-2275. DOI: 10.1364/JOSAB.15.002269

[19] Farahmand M, de Sterke M. Parametric amplification in presence of dispersion fluctuations. Optics Express. 2004;**12**:136-142. DOI: 10.1364/OPEX.12.000136

[20] Ferrini G, Fsaifes I, Labidi T, Goldfarb F, Treps N, Bretenaker F. Symplectic approach to the amplification process in a nonlinear fiber: Role of signal-idler correlations and application to loss management. Journal of the Optical Society of America B. 2014;**31**:1627-1641. DOI: 10.1364/JOSAB.31.001627

[21] Kakande J, Lundstrom C, Andrekson PA, Tong Z, Karlsson M, Petropoulos P, Parmigiani F, Richardson DJ. Detailed characterization of a fiber-optic parametric amplifier in phase-sensitive and phase-insensitive operation. Optics Express. 2010;**18**:4130-4137. DOI: 10.1364/OE.18.004130

[22] Richter T, Corcoran B, Olsson SL, Lundstrom C, Karlsson M, Schubert C, Andrekson PA. Experimental characterization of a phase-sensitive four-mode fiber-optic parametric amplifier. In: European Conf. Exhib. Optical Communication (ECOC). Amsterdam, Netherlands; 2012. Paper Th.1.F.1. DOI: 10.1364/ECEOC.2012.Th.1.F.1

[23] McKinstrie CJ. Schmidt decompositions of parametric processes III: Simultaneous amplification and conversion. Optics Express. 2015;**23**:16949-16966. DOI: 10.1364/OE.23.016949

[24] Kylemark P, Sunnerud H, Karlsson M, Andrekson PA. Semi-analytic saturation theory of fiber optical parametric amplifiers. IEEE Journal of Lightwave Technology. 2006;**24**:3471-3479. DOI: 10.1109/JLT.2006.880158

[25] Tong Z, Lundstrom C, Andrekson PA, Karlsson M, Bogris A. Ultralow noise, broadband phase-sensitive optical amplifiers, and their applications. IEEE Journal of Selected Topics in Quantum Electronics. 2011;**18**:1016-1032. DOI: 10.1109/JSTQE.2011.2136330

[26] Yamamoto Y, Haus H. Preparation, measurement and information capacity of optical quantum states. Reviews of Modern Physics. 1986;**58**:1001. DOI: 10.1103/RevModPhys.58.1001

[27] Shirasaki M, Haus HA. Squeezing of pulses in a nonlinear interferometer. Journal of the Optical Society of America B. 1990;**7**:30-34. DOI: 10.1364/JOSAB.7.000030

[28] Kylemark P, Ren J, Karlsson M, Radic S, McKinstrie CJ, Andrekson PA. Noise in dual-pumped fiber-optical parametric amplifiers: Theory and experiments. IEEE Journal of Lightwave Technology. 2007;**25**:2837-2846. DOI: 10.1109/JLT.2007.902098

[29] Rudd JV, Law RJ, Luk TS, Cameron SM. High-power optical parametric chirped-pulse amplifier system with a 1.55μm signal and a 1.064 μm pump. Optics Letters. 2005;**30**:1974-1976. DOI: 10.1364/OL.30.001974

[30] Nicholson JW, Yablon AD, Westbrook PS, Feder KS, Yan MF. High power, single mode, all-fiber source of femtosecond pulses at 1550 nm and its use in supercontinuum generation. Optics Express. 2004;**12**:3025-3034. DOI: 10.1364/OPEX.12.003025

[31] Yang S, Cheung KKY, Zhou Y, Wong KKY. Tunable single-longitudinal-mode fiber optical parametric oscillator. Optics Letters. 2010;**35**:481-483. DOI: 10.1364/OL.35.000481

[32] Tang R, Devgan P, Voss PL, Grigoryan VS, Kumar P. In-line frequency—Nondegenerate phase-sensitive fiber-optical parametric amplifier. IEEE Photonics Technology Letters. 2005;**17**:1845-1847. DOI: 10.1109/LPT.2005.853226

[33] Tong Z, Lundstrom C, Andrekson PA, McKinstrie CJ, Karlsson M, Blessing DJ, Tipsuwannakul E, Puttnam BJ, Toda H, Gruner-Nielsen L. Towards ultrasensitive optical links enabled by low-noise phase-sensitive amplifiers. Nature Photonics. 2011;**5**:430-436. DOI: 10.1038/nphoton.2011.79

[34] McKinstrie CJ, Alic N, Karlsson M, Tong Z. Higher-capacity communication links based on two-mode phase-sensitive amplifiers. Optics Express. 2011;**19**:11977-11991. DOI: 10.1364/OE.19.011977

[35] Liu X, Chraplyvy AR, Winzer PJ, Tkach RW, Chandrasekhar S. Phase-conjugated twin waves for communication beyond the Kerr nonlinearity limit. Nature Photonics. 2013;**7**: 560-568. DOI: 10.1038/nphoton.2013.109

[36] Olsson SLI, Corcoran B, Lundstrom C, Eriksson TA, Karlsson M, Andrekson PA. Phase-sensitive amplified transmission links for improved sensitivity and nonlinearity tolerance. IEEE Journal of Lightwave Technology. 2015;**33**:710-721. DOI: 10.1109/JLT.2014.2367096

[37] Marhic ME. Polarization independence and phase-sensitive parametric amplification. Journal of the Optical Society of America B. 2011;**28**:2685-2689. DOI: 10.1364/JOSAB.28.002685

[38] Corcoran B, Olsson SLI, Lundstrom C, Karlsson M, Andrekson PA. Phase-sensitive optical pre-amplifier implemented in an 80 km DQPSK link. Optical Fiber Communication Conference. Los Angeles, CA, USA; Mar. 2012. Paper PDP5A.4. DOI: 10.1364/OFC.2012.PDP5A.4

[39] Umeki T, Asobe M, Takara H, Miyamoto Y, Takenouchi H. Multispan transmission using phase and amplitude regeneration in PPLN-based PSA. Optics Express. 2013;**21**:18170-18177. DOI: 10.1364/OE.21.018170

[40] Umeki T, Asobe M, Takenouchi H. In-line phase sensitive amplifier based on PPLN waveguides. Optics Express. 2013;**21**:12077-12084. DOI: 10.1364/OE.21.012077

[41] Umeki T, Kazama T, Tadanaga O, Enbutsu K, Asobe M, Miyamoto Y, Takenouchi H. PDM signal amplification using PPLN-based polarization-independent phase-sensitive amplifier. IEEE Journal of Lightwave Technology. 2015;**33**:1326-1332. DOI: 10.1109/JLT.2014.2385867

[42] Olsson SLI, Lundström C, Karlsson M, Andrekson PA. Long haul (3465 km) transmission of a 10 GBd QPSK signal with low noise phase-sensitive in-line amplification. European Conf. Exhib. Optical Communication, Cannes, France; Sep. 2014. Paper PD.2.2. DOI: 10.1109/ECOC.2014.6964278

[43] Malik R, Olsson SLI, Andrekson P, Lundström C, Karlsson M. Record-high sensitivity receiver using phase sensitive fiber optical parametric amplification. Optical Fiber Communication Conf.; San Francisco, CA, USA; Mar. 2014. Paper Th2A.54. DOI: 10.1364/OFC.2014.Th2A.54

[44] Iskhakov T, Chekhova MV, Leuchs G. Generation and direct detection of broadband mesoscopic polarization-squeezed vacuum. Physics Review Letters. 2009;**102**:183602. DOI: 10.1103/PhysRevLett.102.183602

[45] Heersink J, Gaber T, Lorenz S, Glöckl O, Korolkova N, Leuchs G. Polarization squeezing of intense pulses with a fiber-optic Sagnac interferometer. Physics Review A. 2003;**68**:013815. DOI: 10.1103/PhysRevA.68.013815

Chapter 4

Raman Fiber Laser–Based Amplification in Telecommunications

Mingming Tan

Additional information is available at the end of the chapter

http://dx.doi.org/10.5772/intechopen.73632

Abstract

The chapter demonstrates a detailed study of Raman fiber laser (RFL)-based amplification techniques and their applications in long-haul/unrepeatered coherent transmission systems. RFL-based amplification techniques are investigated from signal/noise power distributions, relative intensity noise (RIN), and fiber laser mode structures. RFL-based amplification techniques can be divided into two categories according to the fiber laser generation mechanism: cavity Raman fiber laser with two fiber Bragg gratings (FBGs) and random distributed feedback (DFB) Raman fiber laser using one FBG. In addition, in cavity fiber laser–based amplification, reducing the reflectivity near the input helps mitigate the signal RIN, thanks to the reduced efficiency of the Stokes shift from the second-order pump. To evaluate the transmission performance, different RFL-based amplifiers were optimized in long-haul coherent transmission systems. Cavity fiber laser–based amplifier introduces >4.15 dB Q factor penalty, because the signal RIN is transferred from the second-order pump. However, random DFB fiber laser–based amplifier prevents the RIN transfer and therefore enables bidirectional second-order pumping, which gives the longest transmission distance up to 7915 km. In addition, using random DFB laser-based amplification achieves the distance of >350 km single mode fiber in unrepeatered DP-QPSK transmission.

Keywords: Raman amplification, Raman fiber laser, coherent transmission, random fiber laser, cavity fiber laser

1. Introduction

In this chapter, we focus on the novel Raman fiber laser (RFL)-based amplification techniques enabled by second-order pumping and fiber Bragg gratings (FBGs) at first-order pumping wavelengths [1], which is different from the conventional first-order or dual-order pumping schemes [2–4]. In first-order distributed Raman amplification, the signal is amplified by multiple first-order depolarized laser diodes to achieve flat gain profile. However, the signal gain can only occur near the fiber output, resulting in larger signal power profile and higher amplifier noise figure, which becomes the limiting factor of its performance in long-haul or unrepeatered transmission systems [2, 4]. In conventional dual-order Raman amplification, more uniform signal power distribution can be achieved, thanks to the Raman gain that occurs in the middle of the fiber. However, both first-order and second-order pump sources are also required. Particularly, to minimize the amplifier noise figure, the first-order pump power should be very small to enable higher second-order pump power, which requires multiple current and temperature controllers for the pump lasers [5]. Thus, the Raman fiber laser–based amplification reduces the high cost of dual-order pumping and improves the amplifier performance in comparison with first-order pumping, as it uses only second-order pumping with passive FBGs [1, 5].

In general, second-order RFL-based amplification is a distributed Raman amplification scheme, requiring depolarized second-order pumps (~1360 nm assuming the amplified signal is in C band, thanks to the two Stokes shift) and passive FBGs to generate first-order ultra-long Raman fiber laser when the transmission fiber is used as the gain medium. The induced Raman fiber laser together with the residual second-order pump is to amplify the signal in C and/or L band [6, 7]. However, due to different generation mechanisms of induced Raman fiber laser, there are two fiber laser regimes [8]. The first scheme is cavity fiber laser, in other words, Fabry-Perot cavity, where the transmission fiber between two end reflectors forms an ultra-long fiber laser cavity [9, 10]. This can be done with two high reflectivity FBGs or alternatively an FBG with weak Fresnel reflection [11, 12]. Random distributed feedback (DFB) Raman fiber laser is the other laser regime [13]. This is generated because the lasing threshold is overcome in the cavity formed by a distributed feedback (fiber Rayleigh scattering) and high reflective FBG [5, 14, 15].

RFL-based amplification schemes have different impacts on the coherent transmission systems, depending on the pumping schemes. Cavity fiber laser–based amplification can introduce a significant Q factor penalty, limiting the maximum reach to only 1500 km [2, 3, 8, 16], which means that that using forward (FW)-propagated pumping introduced a Q factor penalty, regardless of the reduction in the amplifier noise figure. However, random fiber laser–based amplification mitigates the signal relative intensity noise (RIN), reveals the benefit of the lower noise figure brought by FW-pumping, and effectively extends the maximum reach of the long-haul transmission system [5]. Such random fiber laser–based amplification technique can be applied in unrepeatered transmission systems and achieve a record transmission distance of over 350 km standard single mode fiber (SSMF) using 22 × 100 Gbits DP-QPSK WDM transmitter [17].

RFL-based amplification techniques are characterized from different perspectives, including signal/noise power distributions, relative intensity noise (RIN), and the mode structures of fiber laser. These results help give a better understanding of RFL-based amplification and also support the long-haul and unrepeatered coherent transmission performances demonstrated in this chapter.

2. Raman fiber laser–based amplification

2.1. Cavity Raman fiber laser amplification

2.1.1. Experimental setup

Figure 1 shows the schematic diagram of cavity fiber laser–based amplification using two FBGs. Two high reflectivity (>~95%) FBGs at 1455 nm with 3 dB bandwidths of ~0.5 nm were used at both ends of an 83 km SSMF. When the pump power of depolarized continuous wave second-order pumps at 1366 nm was high enough to overcome the lasing threshold, an ultra-long Fabry-Perot cavity (83 km was the cavity length) fiber laser was generated at 1455 nm [1, 5, 14, 15]. Therefore, the generated first-order fiber laser at 1455 nm and the second-order pump at 1366 nm amplified the signals in the C band [7].

The FW pump and BW pump powers used in the experiment were demonstrated in (**Figure 2**) and only used to compensate the ~16.5 dB loss from the 83.32 km fiber. The FW pump power ratio means the percentage of the FW pump power out of total pump power.

2.1.2. Signal and noise power distributions along the fiber

Signal power distributions along the transmission fiber with different pump powers were measured at 1545.32 nm using a modified optical time-domain reflectometer (OTDR) setup [6]. The OTDR instrument was used to monitor the signal power traces along the fiber. The built-in pulsed Fabry-Perot semiconductor laser at 1550 nm was transferred into the RF pulses which modulated an externally tunable laser through an acoustic optical modulator (AOM). The pulsed tunable laser was then transmitted into the fiber under test (Raman amplified), and the reflections were fed into the OTDR instrument. In this way, the signal power profile along the Raman-amplified fiber span was acquired.

Figure 3 shows both the experimental (solid) and simulated (dotted) signal power profiles [8, 18, 19]. The simulations use a set of equations to describe the power evolution [1]. The signal power profiles were the mutual effect of second-order pump power profiles at 1366 nm and first-order Raman fiber laser power profiles at 1455 nm [8]. For different pump-power combinations, signal power variation (SPV) was calculated as the difference between the maximum and minimum power value along the span, which was used as a metric to compare different pumping schemes. The lowest SPV of ~1.6 dB (+/−0.8 dB) over 83 km SSMF was done by

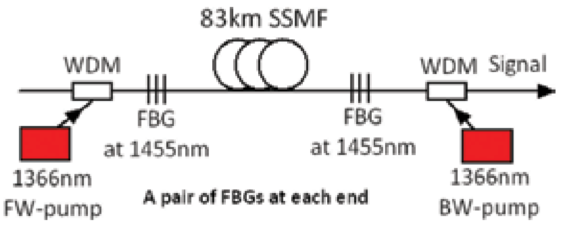

Figure 1. Cavity fiber laser–based amplification with two FBGs.

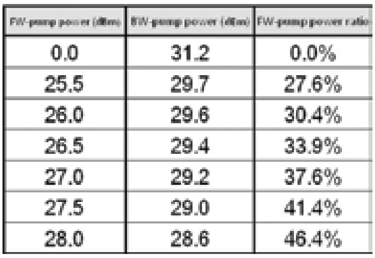

FW-pump power (dBm)	BW-pump power (dBm)	FW-pump power ratio
0.0	31.2	0.0%
25.5	29.7	27.6%
26.0	29.6	30.4%
26.5	29.4	33.9%
27.0	29.2	37.6%
27.5	29.0	41.4%
28.0	28.6	46.4%

Figure 2. The pump power used in the cavity fiber laser–based amplification.

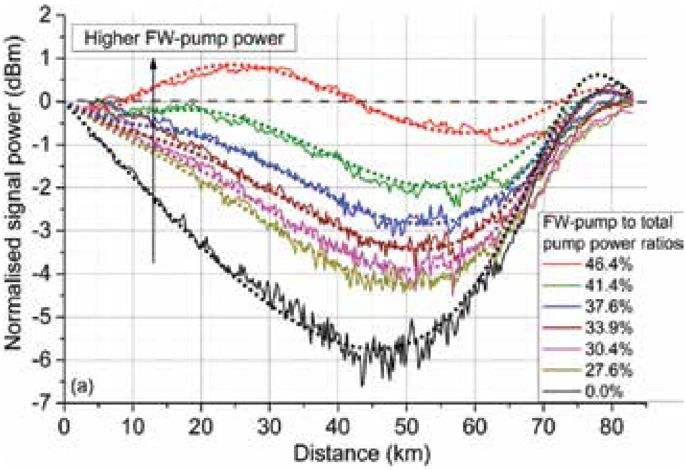

Figure 3. Measured (solid) and simulated (dotted) signal power distributions.

bidirectional pumping with the similar pump powers from both directions. The SPV was increased to ~5.6 dB using BW-pumping only. This means that the second-order FW-pumping reduced the power variation and increased the average signal power relatively, so the noise figure of a distributed Raman amplifier was reduced [4]. **Figure 4** shows the simulated noise power profiles. Compared with BW-pumping only, the noise power was decreased up to ~4 dB using bidirectional pumping. Considering the ASE noise only, the more the FW pump power, the less the ASE noise (the lower the amplifier noise figure). However, when the distributed Raman amplification is evaluated in the long-haul transmission system, the optimum signal launch power depends on the best trade-off between the ASE noise and the nonlinearity (if the RIN-induced penalty from the forward propagated pump is not taken into account). This means that the flat signal power profiles (the smallest power variation) are the key to achieve the best transmission performance using high-order symmetric bidirectional pumping instead of FW-pumping only [5].

2.1.3. Relative intensity noise

Relative intensity noise (RIN) is essentially the intensity variations from the pump source [16]. As the process of the Raman gain is extremely fast, the noise from the pump can affect the

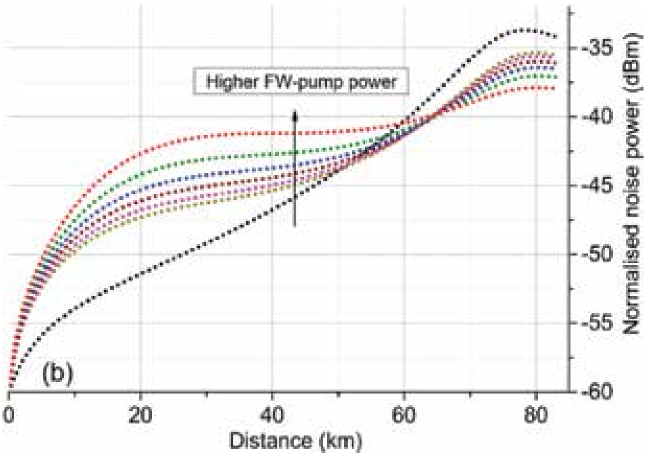

Figure 4. Simulated noise power distributions.

signal. When the pump and the signal travel in the same directions (usually called FW-pumping or co-pumping), the pump noise is more likely to transfer to the signal [3, 16, 20]. When the pump and the signal travel in the reverse, as the pump noise is attenuated and averaged by the transmission fiber [3, 21], BW-pumping is more tolerant to the RIN. FW-pumping can improve the noise figure but increase the signal RIN at the same time. For long-haul transmission, as the RIN is accumulated over the number of spans, the RIN penalty would be very severe. The schematic design of the RIN measurement is illustrated in [8]. The setup for the RIN measurement was based on an ultra-low-noise receiver and an electrical spectrum analyzer (ESA) ranging from 1 up to 160 MHz. The measured RIN of the second-order pump at 1366 nm is ~−120 dB/Hz, which is likely to be the lowest on the market for fiber laser–based pumps. The RIN of the output signal at 1545.32 nm was measured after one span from a CW low RIN (~−145 dB/Hz RIN) tunable laser source, and the FW-propagated Fabry-Perot fiber laser through a 5% splitter was measured.

Figure 5 shows the measured signal RIN in cavity fiber laser–based amplifier using different pump power combinations. When the FW pump power ratio was increased to 46.4%, the signal RIN was 18 dB higher, compared with BW-pumping only. The RIN increase was 9 dB using a 27.6% FW-pumping ratio. **Figure 6** shows the RIN for the first-order-induced fiber laser. The fiber laser RIN was similar for all the pump powers used, except that the fiber laser RIN with BW-pumping only was lower within the range of below 40 MHz. Overall, there were significant differences in RIN between the BW-pumping scheme and all the other schemes using FW-pumping.

2.1.4. Fiber laser mode structures

Figure 7 shows the measured intra-cavity electrical spectra of the FW-propagated fiber laser at 1455 nm for different FW pump powers. Note that the traces in **Figure 7** are deliberately offset to aid the comparison. It indicates that there were two different fiber lasing regimes. Using FW-pumping, a ~1.2 kHz mode spacing was acquired which corresponded to an 83 km

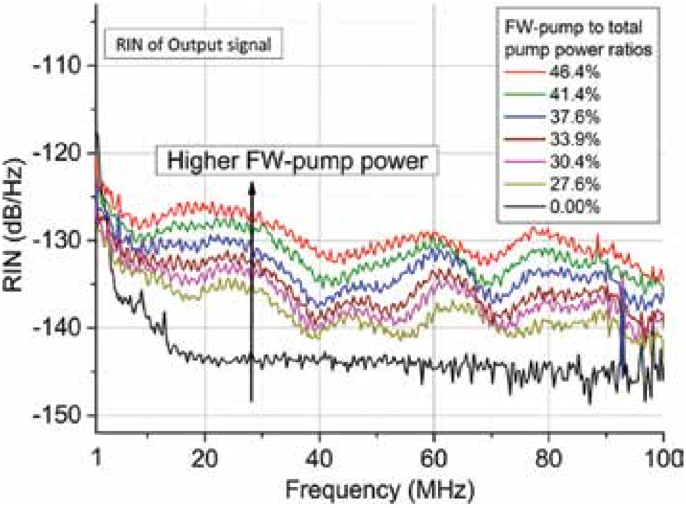

Figure 5. RIN of the output signal using different pump powers in cavity fiber laser–based amplification technique.

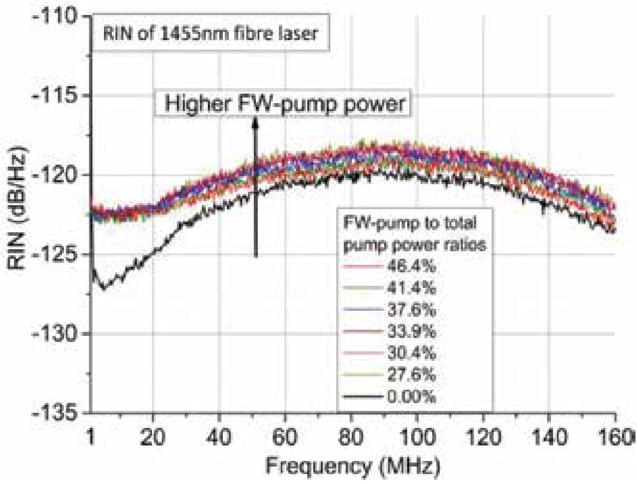

Figure 6. RIN of the induced fiber laser using different pump powers in cavity fiber laser–based amplification technique.

Fabry-Perot cavity. This mode spacing did not depend on the FW pump power used, because it was determined by the cavity length and the refractive index [10], as demonstrated in Eq. (1). Δv is the mode spacing, c is the speed of the light, n is the fiber refractive index, and L is the length of the cavity.

$$\Delta v = \frac{c}{2nL} \tag{1}$$

No mode structure ("modeless" fiber laser) can be seen in BW-pumping only. This was because although a high reflectivity FBG was placed on one side of the cavity, distributed fiber Rayleigh scattering formed on the other side of the cavity, which generated a half-open

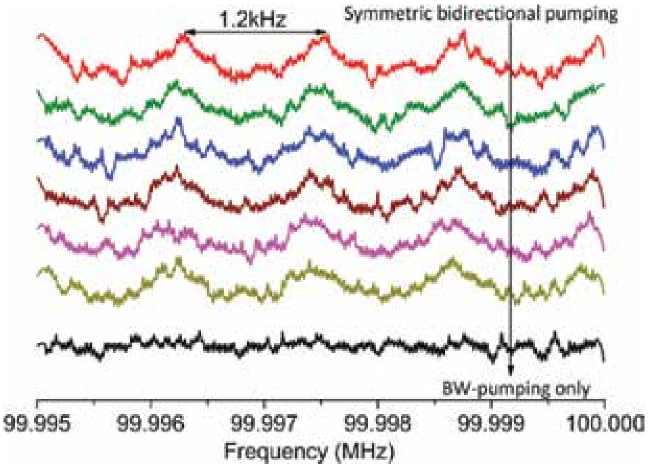

Figure 7. Mode structures of the induced fiber laser using different pump powers in cavity fiber laser–based amplification technique.

fiber laser cavity [15, 22]. Thus, the cavity length of this fiber laser was not fixed due to the randomly distributed Rayleigh backscattering from the fiber [22]. Overall, these results show that with closed cavity with two FBGs, a random DFB fiber laser can be still achieved, which is different from the usual Fabry-Perot fiber laser with bidirectional pumping.

Figure 7 shows that in the fiber span of 83 km, using bidirectional pumping forms a Fabry-Perot cavity fiber laser. On the other hand, using BW-pumping only forms a random DFB fiber laser. However, when the fiber in between FBGs is too long (i.e. >270 km) [10], even with bidirectional pumping, the induced fiber laser is still random DFB fiber laser. This is because due to the high fiber attenuation, the pumps are "isolated" from each other, not powerful enough to reach the FBG on the other side. Instead, similar to the BW-pumping only over 83 km, the fiber Rayleigh backscattering reflects the pump and therefore generates a random fiber laser. Using bidirectional pumping over a very long fiber span generates two separate random fiber lasers at the input and the output [17]. This can be used in unrepeatered transmission systems.

2.2. Random distributed feedback Raman fiber laser–based amplification

2.2.1. Experimental setup

The reflectivity near the input section was close to zero (measured result of 0.04%), achieved by replacing it with an angled connector instead. The schematic diagram of such an amplifier is illustrated in **Figure 8**. The FW pump and BW pump powers are demonstrated in **Figure 9**. Note that the pump powers were only to compensate the loss of 83 km SSMF.

2.2.2. Signal and noise power distributions along the fiber

The signal and noise power distributions along the fiber were shown experimentally (solid line) and theoretically (dotted line) in **Figure 10** [5]. Using the BW-pumping only, the SPV was

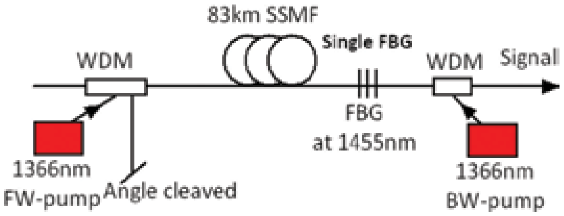

Figure 8. Random fiber laser–based amplification with one FBG.

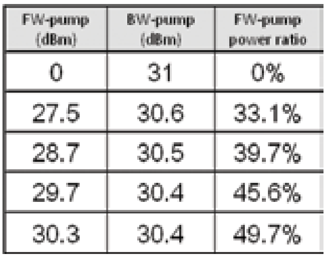

FW-pump (dBm)	BW-pump (dBm)	FW-pump power ratio
0	31	0%
27.5	30.6	33.1%
28.7	30.5	39.7%
29.7	30.4	45.6%
30.3	30.4	49.7%

Figure 9. The pump power used in random fiber laser–based amplification.

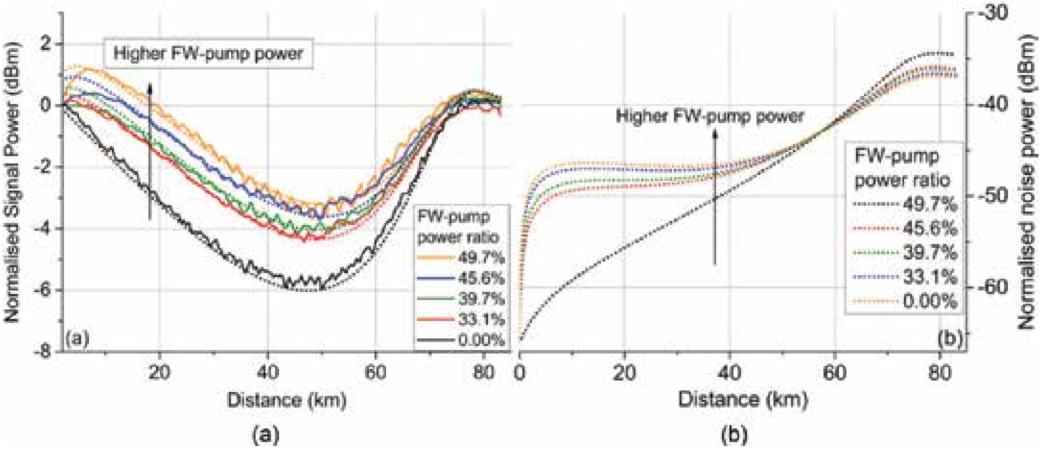

Figure 10. Measured (solid) and simulated (dotted) signal (a) and noise power profiles (b) using random fiber laser–based amplification scheme.

the highest (~6 dB). Using 45.6 or 39.7% FW-pumping ratios, the lowest SPV was reduced to just below 4 dB. However, for the FW pump power ratio of 45.6%, a rapid power increase was seen within the first 10 km near the input end. This was particularly undesired for long-haul transmission systems because this was limited to the maximum signal launch power in order to avoid the Kerr nonlinear impairment [23].

In addition, random DFB fiber laser–based amplification is a good candidate for long-haul transmission system using mid-link optical phase conjugation (OPC) to combat the nonlinearity,

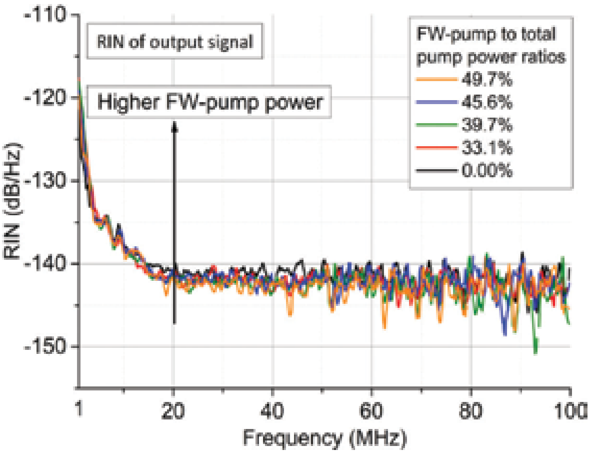

Figure 11. Signal RIN using different pump powers in random fiber laser–based amplification technique.

given the good signal power symmetry of the link [24, 25]. As illustrated in [24], more than 97% symmetry level can be achieved using this amplification technique over 62 km SMF. There are several generation mechanisms of random DFB fiber lasers, but here only the half-opened mechanism is discussed due to the highest Raman gain efficiency [26].

2.2.3. Relative intensity noise

The RIN of the signal at the output end was shown in **Figure 11**. The signal RIN remained the same with the FW pump power over the whole frequency range. This means that the transmission performance can only depend on the balance between the ASE noise and nonlinearity without the RIN-induced penalty being considered [23].

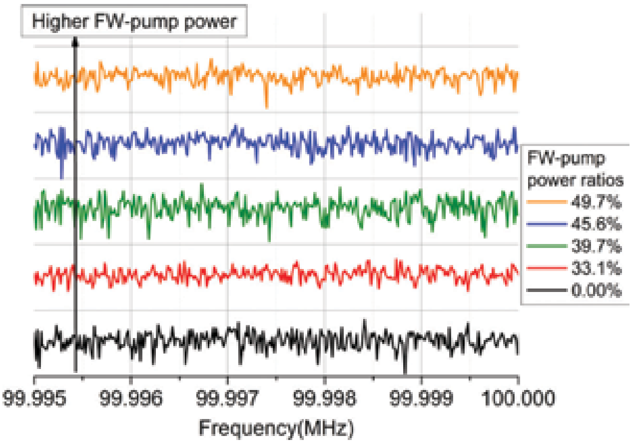

Figure 12. Mode structures of the induced fiber laser using different pump powers in random fiber laser–based amplification technique.

2.2.4. Fiber laser mode structure

Figure 12 shows the mode structure of induced fiber laser with different pump powers. No mode was observed using BW-pumping only or bidirectional pumping, which confirms that it was random DFB fiber laser [8, 15]. The fiber laser was generated due to the resonant mode overcoming the lasing threshold in a distributed cavity formed by the fiber Rayleigh scattering and an FBG.

3. Raman fiber laser–based amplification in telecommunications

3.1. The application in long-haul coherent transmission system

To evaluate different RFL-based amplification schemes, a long-haul recirculating loop experiment was conducted using the setup demonstrated in **Figure 13**. The test signals consisted of 10,120 Gb/s DP-QPSK channels with 100 GHz spacing, while a 100 kHz linewidth tunable laser was used as the "channel under test." The multiplexed signals were QPSK modulated with normal and inverse 2^{31}–1 PRBS patterns at 30 Gb/s with a relative delay of 18 bits between I (in-phase) and Q (quadrature). A polarization multiplexer with a delay of 300 bits between the two polarization states gave the resultant 10 × 120 Gb/s DP-QPSK signals [24]. The transmission span in the recirculating loop was 17.6 dB loss in total, including 16.5 dB from 83.32 km SSMF and 1.1 dB from pump-signal combiners. The loop specific loss was ~12 dB from the AOM, 3 dB coupler, gain flattening filter (GFF), and the passive components from the Raman amplified span. An EDFA was used to compensate the loop loss. The receiver was a standard coherent detection setup and digital signal processing (DSP) was used offline with standard algorithms. Q factors were calculated from bit-wise error rates.

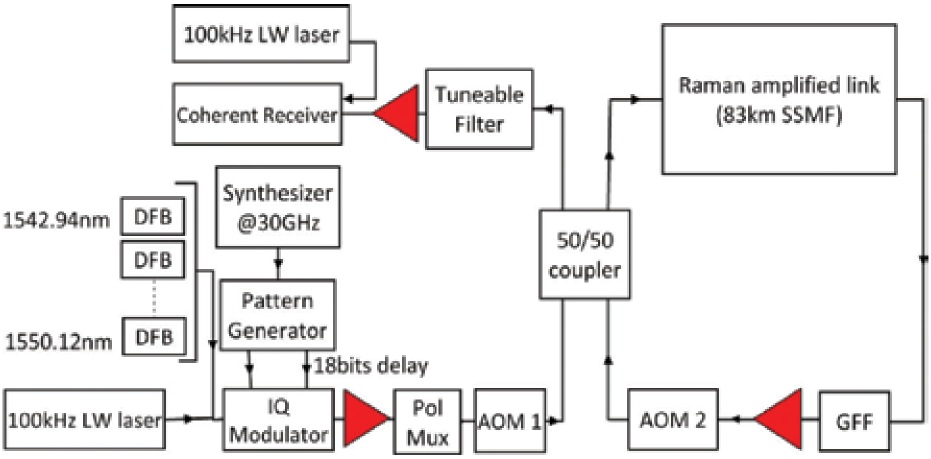

Figure 13. Schematic diagram of long-haul repeatered transmission systems.

As cavity fiber laser–based amplification in **Figure 1** was used in the long-haul transmission, as shown in **Figure 14(a)**; the Q factor at 1666 km was 13.1 dB (BW-pumping only) but decreased to 9 dB (symmetric bidirectional pumping). Using higher FW pump power reduced the Q factor due to the RIN penalty, regardless of the noise figure reduction [8]. The optimum launch power was reduced when the FW pump power was increased. This was because the flatter signal power profile resulted in a higher averaged signal power and therefore the optimum signal launch power was decreased to avoid the Kerr nonlinearity. The degradation in Q factor occurred in all the launch power levels, which indicates that it was not because of the nonlinearity. However, in random fiber laser–based amplification scheme (**Figure 8**) as the FBG near the input was removed, the Q factor at 3333 km (**Figure 14(b)**) with FW pump power ratio of 33% was 0.6 dB better than BW-pumping only, and even using ~50% FW pump power ratio had a similar Q factor to BW-pumping only. This means that using this scheme, the RIN penalty introduced by FW-pumping was minimized, which indicates that the uniform signal power distribution led to effective performance improvement in long-haul transmission systems.

Figure 15 shows the Q factors versus transmission distances using both the amplification schemes. Using random fiber laser–based amplification had similar or better transmission performance (up to 7915 km maximum reach) than the BW-pumping-only scheme, but using cavity fiber laser–based scheme had a significant penalty. An important application of this RIN penalty-free random fiber laser–based amplification scheme was in the nonlinearity mitigation using mid-link OPC because using the scheme had a very symmetrical signal power profile and could maximize the benefit of nonlinearity compensation using mid-link OPC. The details of this work can be found in [24, 25].

3.2. The application in unrepeatered coherent transmission system

In unrepeatered transmissions, distributed Raman amplification offers enhanced noise performance leading to higher OSNR, compared with EDFA [16, 27]. By using higher order distributed

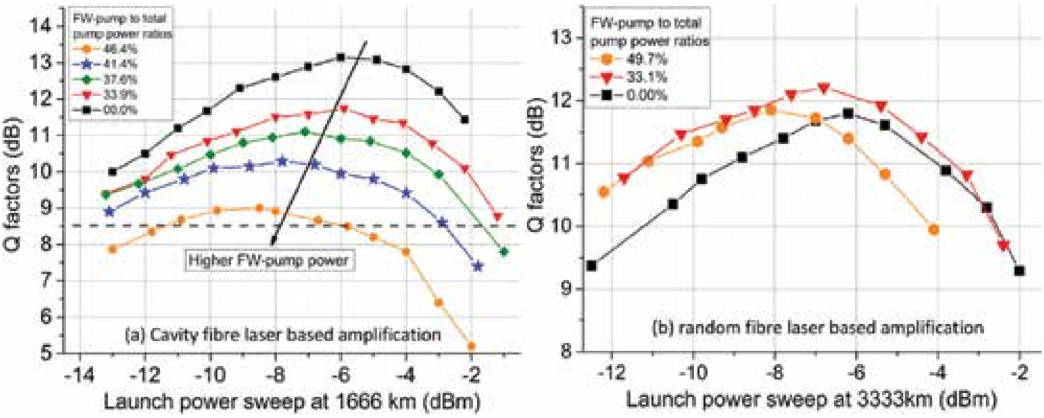

Figure 14. (a) Q factors versus signal launch power using cavity fiber laser–based amplification and (b) Q factors versus signal launch power using random fiber laser–based amplification.

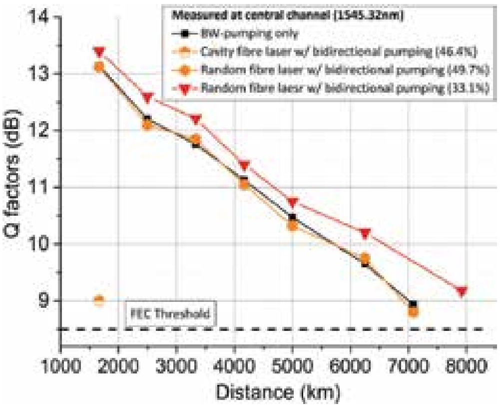

Figure 15. Q factors versus signal launch power using BW-pumping only, cavity fiber laser–based amplification scheme, and random fiber laser–based amplification scheme.

Raman amplifications, the signal power variation can be reduced leading to highly uniform signal power profiles, better trade-offs between ASE noise and nonlinearity, and better transmission performance. Here, based on the RFL-based amplification, the transmission performance using 100G DP-QPSK WDM signals over 352.8 km SMF has been shown without using remote optically pumped amplifier (ROPA) or any specialty fiber [17].

Figure 16 shows the schematic diagram of the unrepeatered transmission system using DP-QPSK WDM signals and random fiber laser–based amplification technique. An important difference of RFL-based amplifier in unrepeatered and repeatered systems is that due to the fiber length of the unrepeatered system (i.e. 300 km), the generated Raman fiber laser at 1455 nm was actually two separate random DFB fiber lasers located near each side of the span and had no interaction with each other [5, 17]. **Figure 17(a)** shows the Q factor versus signal launch power per channel, and **Figure 17(b)** shows the Q factors of all the measured channels at 327.6 and 352.8 km. At 327.6 km, the maximum number of channels was limited to the number of lasers we had. At 352.8 km, 14 channels were transmitted at the FEC threshold

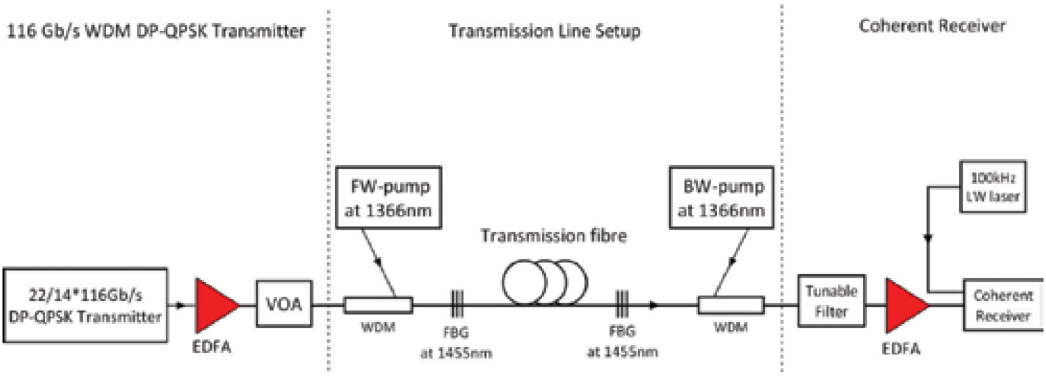

Figure 16. A schematic diagram of random fiber laser–based amplification scheme in unrepeatered transmission.

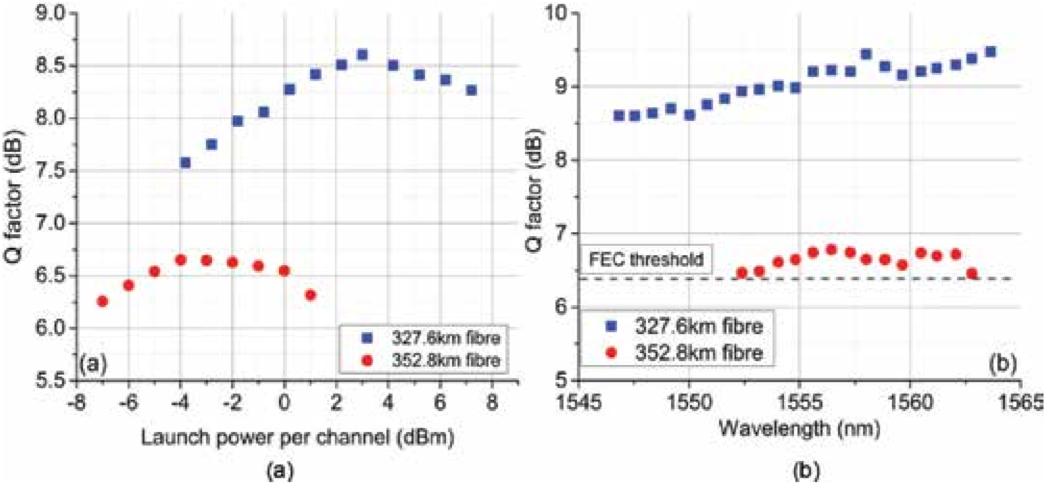

Figure 17. (a) Q factors versus launch power per channel at 327.6 and 352.8 km and (b) Q factors of all the measured channels at 327.6 and 352.8 km.

of 6.4 dB. This was achieved without ROPA and low-loss fiber, which indicates that our proposed setup can be used to readily upgrade the existing SSMF legacy link without the installation of the new fiber. In addition, our proposed setup is compatible with ROPA by adding the seed pump at 1480 nm, which can simultaneously improve the transmission distance and the amplification bandwidth [28-30].

4. Conclusion

In conclusion, Raman fiber laser–based amplification techniques have been characterized as standalone amplifiers, and its performances have been analyzed and optimized in long-haul repeatered and unrepeatered coherent transmission systems. Based on random DFB fiber laser–based Raman amplification, the signal RIN can be successfully mitigated, and bidirectional second-order pumping would not suffer from the RIN penalty. Thus, it provides the best trade-off between ASE noise and nonlinearity and therefore offers the best transmission performance. The scheme is highly flexible and the signal power distributions can be adjusted to meet specific link requirements. This scheme is potentially to be highly effective to compensate the nonlinear impairment and enhance the transmission distance using different nonlinearity compensation techniques, that is, mid-link optical phase conjugation and nonlinear Fourier transform-based transmitter.

Acknowledgements

This work was funded by UK EPSRC Programme Grant PEACE (EP/L000091/1), UNLOC (EP/J017582/1), FP7 ITN programme ICONE (608099), and MSCA IF grant SIMFREE (748767).

We would like to thank the support and contribution from Andrew Ellis, Paul Harper, Sergei Turitsyn, Paweł Rosa, Son Thai Le, Ian Phillips, Juan Diego Ania-Castanon, Md Asif Iqbal, and thank Changle Wang, Zhongyuan Sun, and Lin Zhang for providing the FBGs.

Author details

Mingming Tan

Address all correspondence to: m.tan1@aston.ac.uk

Aston Institute of Photonic Technologies, Aston University, Birmingham, UK

References

[1] Ania-Castañón JD. Quasi-lossless transmission using second-order Raman amplification and fiber Bragg gratings. Optics Express. 2004;**12**:4372-4377

[2] Bromage J. Raman amplification for fiber communications systems. Journal of Lightwave Technology. 2004;**22**:79-93

[3] Fludger CRS, Handerek V, Mears RJ. Pump to signal RIN transfer in Raman fiber amplifiers. Journal of Lightwave Technology. 2001;**19**:1140-1148

[4] Bouteiller J-C, Brar K, Headley C. Quasi-constant signal power transmission. In: ECOC. 2002. pp. 1-2

[5] Tan M, Rosa P, Le ST, Md A, Iqbal IDP, Harper P. Transmission performance improvement using random DFB laser based Raman amplification and bidirectional second-order pumping. Optics Express. 2016;**24**:2215-2221

[6] Ania-Castañón JD, Karalekas V, Harper P, Turitsyn SK. Simultaneous spatial and spectral transparency in ultralong fiber lasers. Physics Review Letters. 2008;**101**:123903

[7] Ellingham TJ, Ania-Castañón JD, Ibbotson R, Chen X, Zhang L, Turitsyn SK. Quasi-lossless optical links for broad-band transmission and data processing. IEEE Photonics Technology Letters. 2006;**18**(1):268-270

[8] Tan M, Rosa P, Le ST, Phillips ID, Harper P. Evaluation of 100G DP-QPSK long-haul transmission performance using second order co-pumped Raman laser based amplification. Optics Express. 2015;**23**:22181-22189

[9] Ania-Castañón JD, Ellingham TJ, Ibbotson R, Chen X, Zhang L, Turitsyn SK. Ultralong Raman fiber lasers as virtually lossless optical media. Physical Review Letters. 2006; **96**(2):023902

[10] Turitsyn SK, Ania-Castañón JD, Babin SA, Karalekas V, Harper P, Churkin D, Kablukov SI, ElTaher AE, Podivilov EV, Mezentsev VK. 270-km ultralong Raman fiber laser. Physical Review Letters. 2009;**103**(13):133901

[11] Gallazzi F, Rizzelli G, Md A, Iqbal MT, Harper P, Ania-Castañón JD. Performance optimization in ultra-long Raman laser amplified 10×30 GBaud DP-QPSK transmission: Balancing RIN and ASE noise. Optics Express. 2017;**25**:21454-21459

[12] Rizzelli G, Iqbal MA, Gallazzi F, Rosa P, Tan M, Ania-Castañón JD, Krzczanowicz L, Corredera P, Phillips I, Forysiak W, Harper P. Impact of input FBG reflectivity and forward pump power on RIN transfer in ultralong Raman laser amplifiers. Optics Express. 2016;**24**:29170-29175

[13] Turitsyn SK, Babin SA, El-Taher AE, Harper P, Churkin DV, Kablukov SI, Ania-Castañón JD, Karalekas V, Podivilov EV. Random distributed feedback fibre laser. Nature Photonics. 2010;**4**:231-235

[14] Papernyi SB, Karpov VI, Clements WRL. Third-order cascaded Raman amplification. In: Optical Fiber Communications Conference (Optical Society of America, 2002), Paper FB4

[15] Zhang WL, Rao YJ, Zhu JM, Yang ZX, Wang ZN, Jia XH. Low threshold 2nd-order random lasing of a fiber laser with a half-opened cavity. Optics Express. 2012;**20**:14400-14405

[16] Pelouch WS. Raman amplification: An enabling technology for high-capacity, long-haul transmission. In: OFC 2015, Paper. W1C.1

[17] Rosa P, Tan M, Le ST, Philips ID, Ania-Castañon JD, Sygletos S, Harper P. Unrepeatered DP-QPSK transmission over 352.8 km SMF using random DFB fiber laser amplification. Photonics Technology Letters. 2015;**27**(11):1041-1135

[18] Rosa P, Rizzelli G, Tan M, Harper P, Ania-Castañòn JD. Characterisation of random DFB Raman laser amplifier for WDM transmission. Optics Express. 2015;**23**:28634-28639

[19] Rosa P, Le ST, Rizzelli G, Tan M, Ania-Castañón JD. Signal power asymmetry optimisation for optical phase conjugation using Raman amplification. Optics Express. 2015;**23**: 31772-31778

[20] Ohki Y, Hayamizu N, Irino S, Shimizu H, Yoshida J, Tsukiji N. Pump laser module for co-propagating Raman amplifier. Furukawa Review. 2003;**24**:6-12

[21] Bromage J, Bouteiller J-C, Thiele HJ, Brar K, Nelson LE, Stulz S, Headley C, Boneck R, Kim J, Klein A, Baynham G, Jorgensen LV, Gruner-Nielsen L, Lingle RL, DiGiovanni DJ. WDM transmission over multiple long spans with bidirectional Raman pumping. Journal of Lightwave Technology. 2004;**22**(1):225-232

[22] Churkin DV, Babin SA, El-Taher AE, Harper P, Kablukov SI, Karalekas V, Ania-Castañón JD, Podivilov EV, Turitsyn SK. Raman fiber lasers with a random distributed feedback based on Rayleigh scattering. Physics Reviews A. 2010;**82**:033828

[23] Tan M, Rosa P, Iqbal MdA, Phillips ID, Nuno J, Ania-Castanon JD, Harper P. RIN mitigation in second-order pumped Raman fibre laser based amplification. In: ACP 2015, Paper. AM2E.6

[24] Phillips I, Tan M, Stephens MF, McCarthy M, Giacoumidis E, Sygletos S, Rosa P, Fabbri S, Le ST, Kanesan T, Turitsyn SK, Doran NJ, Harper P, Ellis AD. Exceeding the nonlinear-shannon limit using raman laser based amplification and optical phase conjugation. In: Optical Fiber Communication Conference, OSA Technical Digest (online) (Optical Society of America, 2014), Paper M3C.1

[25] Ellis AD, Tan M, Iqbal MA, Al-Khateeb MAZ, Gordienko V, Saavedra Mondaca G, Fabbri S, Stephens MFC, McCarthy ME, Perentos A, Phillips ID, Lavery D, Liga G, Maher R, Harper P, Doran N, Turitsyn SK, Sygletos S, Bayvel P. 4 Tb/s transmission reach enhancement using 10 × 400 Gb/s super-channels and polarization insensitive dual band optical phase conjugation. Journal of Lightwave Technology. 2016;**34**:1717-1723

[26] Churkin DV, Sugavanam S, Vatnik ID, Wang Z, Podivilov EV, Babin SA, Rao Y, Turitsyn SK. Recent advances in fundamentals and applications of random fiber lasers. Advances in Optics and Photonics. 2015;**7**:516-569

[27] Chang D, Pelouch WS, Burtesv S, Perrier P, Fevrier H. Unrepeatered high-speed transmission systems. In: Optical Fiber Communication Conference, OSA Technical Digest (Online) (Optical Society of America, 2015), Paper. W4E.3

[28] Rosa P. Quasi-lossless data tranmission with ultra-long Raman fibre laser based amplification [PhD thesis]. Aston University. 2013

[29] Cheng J, Tang M, Lau APT, Lu C, Wang L, Dong Z, Bilal SM, Fu S, Shum PP, Liu D. Pump RIN-induced impairments in unrepeatered transmission systems using distributed Raman amplifier. Optics Express. 2015;**23**(9):11838-11854

[30] Alcon-Camas M, Ania-Castañón JD. RIN transfer in 2nd-order distributed amplification with ultralong fiber lasers. Optics Express. 2010;**18**(23):23569-23575

Chapter 5

Fiber Lasers and Their Medical Applications

Amira Tandirovic Gursel

Additional information is available at the end of the chapter

http://dx.doi.org/10.5772/intechopen.76610

Abstract

Advancing of photonics, aided with fruitful and abundant experimental and theoretical studies, over the last four decades has brought about the invention of a large variety of lasers. Among them one of the most popular types is a fiber laser, which is a variation of the standard solid-state laser, with the medium being a clad fiber waveguide structure and different dopants inside core serve as a gain media. They were derived from erbium-doped fiber amplifiers, which are still important component for telecommunications. Since discovery, fiber laser has become a natural choice for many uses, primarily because of the physical characteristics of fiber waveguide structure. Their rapid progress may show how excellent they really are. Although fiber lasers are today widely used in various research and industrial areas, one of the most meaningful applications of fiber laser technology has been through its use in medicine. A wide variety of wavelengths generated by fiber lasers as well as the diversity of physical mechanisms employed in pulse generation also additionally underpins the flexibility of fiber laser technology. This study is devoted to background technology of fiber lasers in the light of medical applications. Basic physics and theories of optical fibers and their important properties are introduced.

Keywords: fiber lasers, resonators, pumping, temporal regimes, non-ablative fiber lasers, ablative fiber lasers, host, active media

1. Introduction

From the historical point of view, it can be said that the first working optical fiber laser was developed by Snitzer and his colleagues in the early 1960s [1], as a combination of earlier work on solid-state laser with his novel work on optical fibers [2]. Although this brilliant idea of combining these two then-young technologies was many years ahead of its time, the proving of its substantiality still took a long time. However, it became almost forgotten in the next several years until 1985, when it was rekindled at Stanford University by Payne and co-workers, who worked on Erbium-doped amplifiers [3].

In the early years, relatively low output powers as well as low brightness of the fiber sources delimited areas of usage, preventing their use in a number of important applications requiring high average or peak powers. Likewise, not only the small diameter but also the small acceptance angle of the fiber core limited these devices and consequently made them convenient just for laboratory work. These limitations were overtaken thanks to the breakthrough technology of the double-cladding concept in 1988 [4]. Despite beginning difficulties, this new laser technology has been adopted swiftly by the relatively conservative laser community, primarily due to promising performance level as well as flexible configuration.

The fiber laser field continued to grow in 1990s, aided with fruitful and abundant experimental and theoretical results, gave rise to a large variety of fiber lasers, not only emitting at different wavelengths and with different pulse duration and energies, but also exploiting different physical mechanisms of pulse generation. The revolution was accelerated after the fabrication of optical fibers doped with rare-earth elements such as Ytterbium, Erbium, Holmium, and Thulium that are used to make amplifiers and lasers [1]. However, major advances in laser performance came to light after discovery of new mode-locking regimes, envisaged mainly for improving its limitations with respect to pulse energy and duration, which led to production of pulses of light with extremely short duration, on the order of picoseconds or femtoseconds [5]. Their biggest drawback was the limitation to peak power by nonlinear effects, which were enforced by the large product of intensity and interaction length inside the fiber core. Although most efforts were focused on weakening these effects, being constrained with an important drawback such as significant reduction of the pulse quality, soon it was become aware of the fact that they can overcome using large-mode-area fiber designs (LMA's) instead of conventional small mode-field diameter fibers. Since LMA's have reduced numerical aperture to maintain single-mode guidance, which is more appropriate for robust power operation, the invention of LMA's was followed by adoption of the technique related to pump-coupling [4]. However, introducing several mode-locking mechanisms such as self-similariton, dispersive soliton, and soliton-similariton regimes, demonstrated in recent years, and idea of managing nonlinearities are likely to surpass many of previously noted limitations in a better way [6].

Considering the ongoing evolution of average output power, which is a key performance parameter determining the applicability on any laser, over the past 25 years it can be said that the ultrafast fiber lasers have been reached from a few mW by 1996 and to almost 1 kW by 2009 [7]. It is to be notified that, being pushed roughly by demand for increasingly shorter pulses, the development in ultrafast fiber laser technology has brought about a variety of temporal output properties that can be encouraged especially in terms of pulse duration and pulse repetition frequency [8]. Otherwise, for continuous-wave fiber lasers, the average output powers would have been reached from just 4 W in the early 1990s to till multi-kilowatt and even more than megawatt today [2].

The revolution established on the desire for inventing a way or ways to guide light has had consequences that no one expected. An increase in the output average power, diversity of mode-locking regimes and active medium as well as highly adaptable design of the fiber lasers have unlocked their potential usage. Certainly, the major contributor of this intensive progress was the continually growing telecommunication market [9]. However, various intrinsic advantages of fiber lasers, such as excellent beam quality, high efficiency, simplicity of optical cavity construction, micro joule-level energies at high repetition rates that boost processing speed, and above all relatively low cost, have recently brought about set up of a new branch of industry. Nowadays, they are fundamental building blocks of many contemporarily photonic systems, used for scientific researches as well as in a wide range of industrial and medical applications [10].

Especially from the medical point of view, fiber lasers are deployed in almost all spheres of this field, from diagnosis, noninvasive therapeutic procedures and surgery to micro-cutting applications for the medical device industry. Specifically, ~2 μm pulses have superiority in arthroscopy, urology, and spinal surgery, while ~3 μm pulses are prospering in brain tissue treatment, bone and cutaneous surgery, and ophthalmology [11]. Likewise, fiber lasers seem to be quite convenient light sources for spectroscopic methods, such as Infrared, Raman, and Photothermal spectroscopies, which are excellent methods for both chemical and biological analyses. In particular, spectroscopy combined with microscopy has become a powerful diagnostic tool in the biomedical applications.

Before specifying the particular applications of fiber lasers in medicine, it is instructive to briefly discuss general concepts common to all-fiber lasers especially, such as the nature of light fundamentals of lasing process, and spectroscopic properties of the prominent rare-earth dopant elements, related ions, and amplification theory for two-, three-, and four-level ions and host media.

2. Basic concepts of fiber lasers

2.1. Structure and double-clad concept

In the context of laser physics, the active laser medium, also known as gain medium or lasing medium, is a medium in which the power of light can amplified in order to compensate for the resonator losses. The active laser medium is the source of optical gain within a laser the physical origin of which is stimulated emission process and refers to the amount of amplification.

According to classification of lasers with respect to gain media, a fiber laser is a special type of solid-state laser which uses a doped fiber as an active gain medium [12, 13]. An optical fiber is transformed into active by doping its core with one of the rare-earth materials or their mixture, bound up with doped fiber amplifiers, providing light amplification without lasing [11]. That is to say, a fiber-amplifier, which is commonly used to restore optical signals and overcome their transmission losses, can be transformed into a fiber laser by placing it inside the cavity designed to obtain feedback [13, 14].

From a layout standpoint, a fiber laser is a light-guiding strand of silica or a fluoride glass that is only a few times as thin as the thickness of a hair [14]. Its tiny core, just of sub-millimeter diameter, is doped with trivalent rare-earth elements ions [15]. **Figure 1** shows a rudimentary form of the fiber laser. Launching of the pump light into the core of the doped fiber is ensured

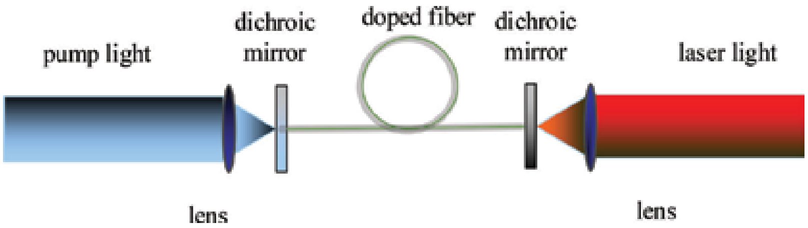

Figure 1. A schematic setup of a basic fiber laser.

via a dichotic mirror placed the left-hand side. Optical pump power is absorbed by dopant ions through the process of stimulated emission at the signal wavelength. Finally, the generated light is extracted on the right-hand side [13, 15].

A huge advancement in fiber lasers technology can be attributed doubtlessly to certain depictive characteristics, coming out by virtue of their waveguide geometry. These are mainly related on double-clad geometry refers to high power fiber lasers. As it is shown in **Figure 2a**, a double-clad fiber is a fiber with a relatively small diameter actively doped core, possessing the highest refractive index, two undoped cladding layers of a large diameter, and polymer coating for protecting from environmental influences [16, 17]. Typically, the single-mode core is surrounded by a second waveguide, called inner cladding. It is highly multimode, refractive index of which is higher than the outer cladding, as shown in **Figure 2b**. This difference between refractive indexes, based on total internal reflection principle, allows the inner cladding to guide light in the same way the core does, provided that wavelength ranges are different. In other words, the inner cladding acts as a waveguide of the pump light concurrently confines the signal light propagating through the core [18].

As the core is located within the inner cladding, it is also a part of the pump waveguide. Thus, it can be deduced that the pump light can also interact with the ions in the core so as to produce optical gain for signal propagation. Besides the various advantages of this configuration, converting a low brightness light source into the high brightness, high power one is, definitely, one

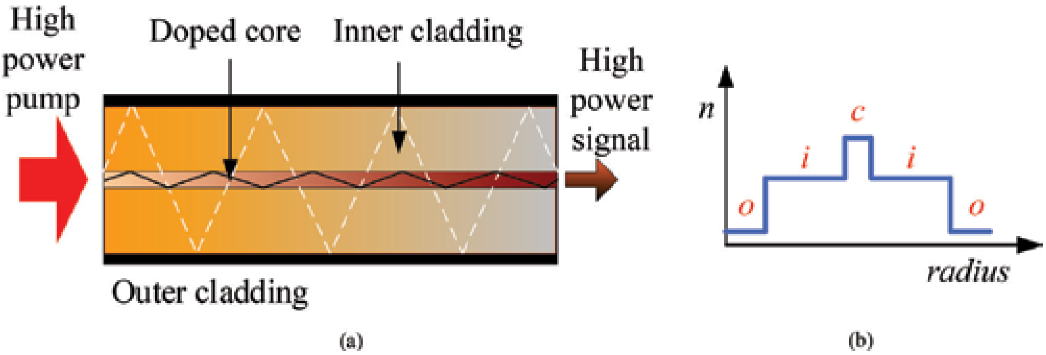

Figure 2. (a) The double-clad fiber concept of high power fiber lasers. (b) Refractive index profile. c: core, i: inner cladding, o: outer cladding.

of those to be mentioned separately [16]. In spite of pumping with low beam quality sources such as diode bars or stacks, the output beam guided through the core has the diffraction-limited beam quality. It is to be noted that this very efficient brightness improvement technique together with continuing advancement of pumping technologies has been the primary driving force not only for the increase of fiber laser powers but also for the decrease of the cost per watt [19].

It is to be pointed out that a larger core not only improves the pump absorption but also provides better energy storage that is of especially important for high energy Q switched pulses. However, robust single-mode operation requires the core of a diameter in the range of 2–10 μm [17].

The inner cladding diameter may vary in the range of 200–400 μm. Its circular shape often leads to weak overlap between the core and pump modes due to the fact that the overlap is also different for different modes, resulting in such weak pump absorption that only 10–30% of the power is delivered into the core [20]. Some of these modes have such little overlap that exhibit only very weak pump absorption resulting in substantial pump power may be left no matter whether some of the pump cladding modes are absorbed better than the average [21]. The absorption efficiency can be significantly improved by breaking the cylindrical symmetry when the rays are forced to follow more irregular or even chaotic paths [21]. Noncircular shapes, especially D and rectangular ones are proposed to thwart the propagation of such unwanted intensity distributions. **Figure 3** shows various designs of inner claddings.

Similarly to all solid-state lasers, there are three principal elements inducing the gain in a fiber laser. They are: the dopant ions with their distinctive free-ion electronic configurations and charge states; the host material in terms of its optical, macroscopic, thermal, mechanical, and

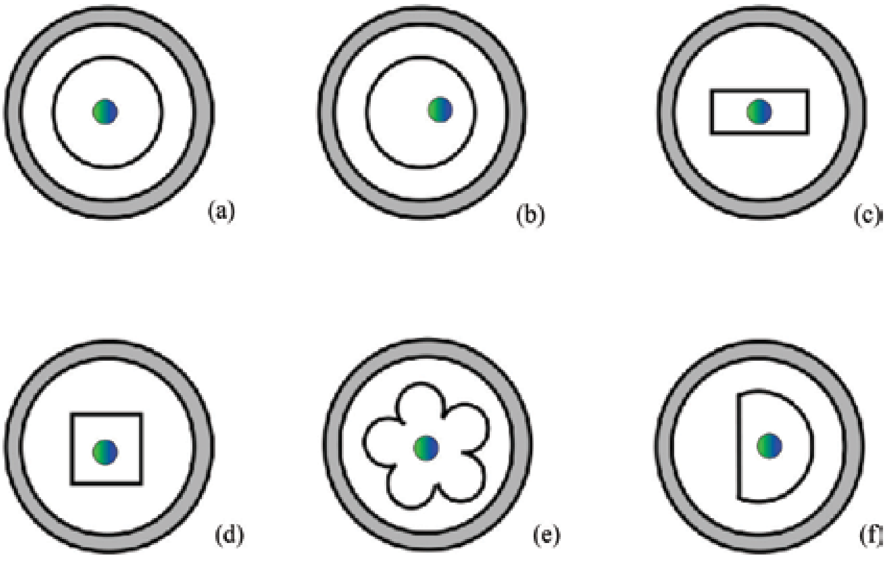

Figure 3. Common cladding-pumped structures: (a) centered core, (b) off-centered core, (c) rectangular inner cladding, (d) square inner cladding, (e) flower inner cladding, and (f) D-shape inner cladding [12].

lattice properties; and the optical pump source taking its temporal characteristic into account, spectral irradiance, and particular geometry. These elements are interrelated and have to be chosen self-consistently [22].

2.2. Fiber resonators and pumping process

An optical resonator, an optical counterpart of an electronic resonant circuit, a major component of the laser that surrounds the gain medium, is an arrangement of optical components that allows the laser light to circulate in a closed path forming standing waves for certain resonance frequencies and incorporating feedback for the light. The frequency selectivity is an important property of the optical resonators since it makes them useful as optical filters, spectrum analyzers, or, the most important, confining/storing of light at specific resonant frequencies.

The physics of optical resonators used for fiber lasers is almost similar to the traditional laser resonators with some differences related to the tolerance for optical damages and fiber coupling of the intracavity components and length of the laser medium. Although optical resonators can be made in very different forms to meet many different criteria, this section briefly reviews three fundamental types that have been exploited in fiber laser technology, taking to account some important advantages and disadvantages. These are: linear laser resonator, all-fiber ring resonator, and Fox–Smith resonator, illustrated in **Figure 4**.

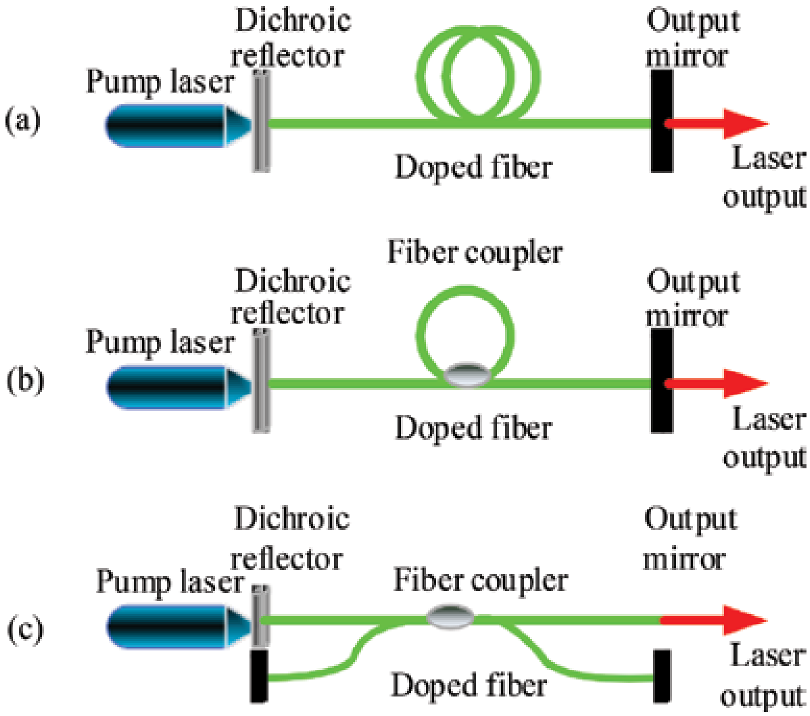

Figure 4. Resonator types: (a) Fabry-Perot with dielectric reflectors; (b) all-fiber resonator; and (c) Fox-Smith resonator.

Pumping is a process that is utilized in lasers and amplifiers with doped gain media, an example of which are fiber lasers for energy transfer from the external source into the active medium. The energy which is can be provided in the form of light, electric current, or as result of chemical or nuclear reactions, is absorbed by the medium directs its atoms to get through excited states and when the majority of the atoms are in excited states population inversion is achieved and the medium acts as a laser or an optical amplifier. It is to be noted that common of all implemented pump power must be higher than the threshold power essential for lasing process of the media.

Fiber lasers utilize optical pumping, generally used for lasers possessing transparent active medium. The most widely used optical pump sources for CW fiber lasers are arc lamps, lasers diodes, or more often some other fiber laser. Depending on required power, the laser diode sources used in pumping process can be fabricated as single-emitter diodes, broad area laser diodes, diode bars, diode laser stack of bars, or fiber-coupled diode laser [22, 23]. To achieve high pumping efficiency and avoid high thermal load, characteristic for high power fiber lasers, the laser diode sources have the spectrum that is as narrow as to be mostly within the absorption region of the gain medium. Furthermore, for the same reason, the wavelength is also kept near the absorption peak of the gain medium over the operation temperature and condition [24]. Several different types of diode lasers are illustrated in **Figure 12**. Single-emitter diodes are very compact battery-powered systems, whose output power does not exceed 1watt. Broad area laser diodes, which can be treated as very efficient laser light sources due to their electro-optical efficiency, exceed 70%, typically generate several watts and are suitable for pumping solid-state lasers. Diode bars are formed with multiple emitters side by side in a single substrate that can provide tens of watts [25]. Laser stack of bars are often used for the highest powers and emit multiple kilowatts. In contrast to the previous types of laser diode, fiber-coupled diode lasers can be treated as a different kind of pump optics, which provide separation of the actual laser head from another package containing the pump diodes, so that the laser head can become very compact [26].

Fiber lasers are optically pumped not only with diode sources but also with other fiber lasers and this pumping method is known as tandem pumping [27]. In tandem pumping method, the output of several double-clad fiber lasers is combined into a single high brightness beam to pump the main amplifier fiber. This strategy provides pumping closer to the emission wavelength, which reduces the quantum defect heating what in turn reduces thermal load. In addition, the high brightness of this pump source can also allow the length of the main amplifier fiber to be reduced, therefore helping to mitigate one of the main limitations of fiber lasers systems nonlinear effects [10]. Although tandem pumping allows for the highest output powers, the vast majority of fiber lasers are pumped directly by laser diodes as they are simpler, cheaper, and also have higher wall plug efficiency [23].

However, the output beam quality and the brightness of the source decrease with increasing power, which can sometimes result in very strong asymmetric and fairly poor beam quality followed by brightness that is much lower than some lower power diodes that requires the use of beam shapers. Although they are utilized to symmetrize the beam quality, they make it easier either to pump a bulk laser or to couple the light into the fiber [17].

Double-clad fiber lasers are conventionally categorized as being either end-pumped or side pumped and both of techniques are illustrated in **Figure 5** [28, 29]. In end-pumping, the light from one or many pump sources is coupled via an optical coupling system through a front surface. Additionally, end-pumping can be provided by pumping through either backward surface or both end sides of the fiber laser. On the other hand, in side-pumping the pump source is connected through a side surface.

2.3. Temporal regimes of fiber lasers

On the basis of temporal regimes, radiation of fiber lasers may be is provided in continuous-wave (CW) or ultrashort optical pulse form depending of temporal regime used [30]. There are three main temporal regimes to provide laser action: continuous-wave and free-running, mode-locking, and Q-switching.

Even through laser light is perhaps the purest form of light, it is not of a single, pure wavelength, but of some natural bandwidth or range of frequencies, which is determined by the gain of laser medium as well as optical cavity or resonant cavity of the laser. Bounced between the mirrors of the cavity, the light constructively and destructively interferes with itself, which leads to the formation of standing waves of discrete set of frequencies between the mirrors. These discrete set of frequencies, known as the longitudinal modes, are self-regenerating and allowed to oscillate by the resonant cavity. Each of these modes oscillates independently, with no fixed relationship between each other. Consequently, the laser acts as a set of independent

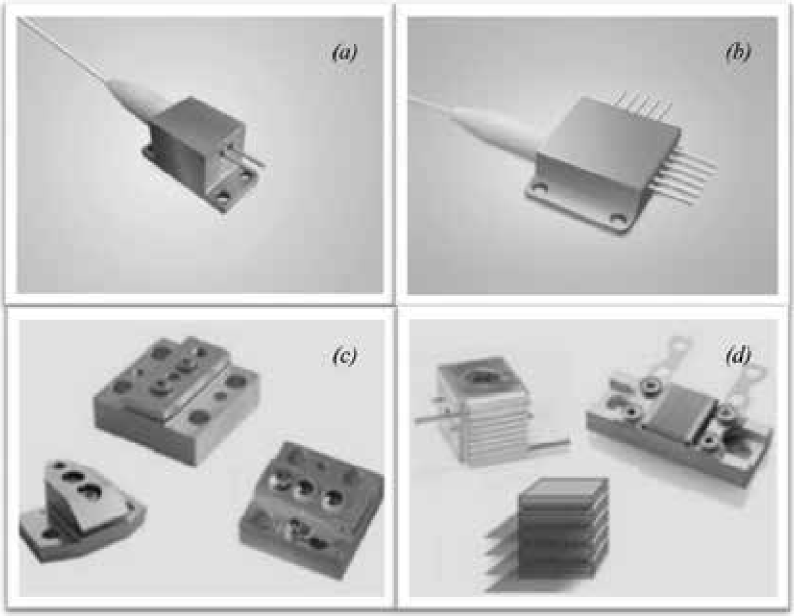

Figure 5. Different types of diode lasers: (a) Fiber-coupled diode laser; (b) 808 nm 4 W single-emitter diode laser; (c) power diode bars; (d) high power vertical diode laser Stac.

lasers, all emitting light at slightly different frequencies. An increase in the number of modes causes near-constant output intensity because interference effects tend to average, and, than, the laser is said to operate as continuous wave [31].

Instead of oscillating independently, each mode can operate with a fixed interconnected phase. In other words, the phase relations among a large number of neighboring longitudinal modes of the laser cavity are locked. As a result, the modes of the laser will mutually interfere, producing a periodic variation in the laser output in form of intense burst or pulse of light of extremely short duration (10^{-12}–10^{-15} s), having a significantly larger peak power than the average power of the laser. Such a laser is said to be mode-locked or phase-locked [8]. These pulses occur separated in time by $\Delta t = 2\ L/c$, where Δt is the time taken for the light to make exactly one round trip of the laser cavity and L is the cavity length (**Figure 6**).

Refers to the way of gain modulation, mode-locking methods can be classified as active and passive. Active methods typically involve using an external signal to induce a modulation of the intracavity light, but, rely on placing some element into the laser cavity which causes self-modulation of the light. Passive methods, on the other hand, do not need any external signal to produce pulses. Rather, they use the light in the cavity to cause a change in some intracavity element, which will then itself produce a change in the intracavity light [8]. A saturable absorber is an optical device that exhibits an intensity-dependent transmission. What this means is that the device behaves differently depending on the intensity of the light passing through it. For passive mode-locking, ideally a saturable absorber will selectively absorb low intensity light, and transmit light which is of sufficiently high intensity.

There are also passive mode-locking schemes that do not rely on materials that directly display an intensity-dependent absorption. In these methods, nonlinear optical effects in intracavity components are used to provide a method of selectively amplifying high intensity light in the cavity, and attenuation of low intensity light. One of the most successful schemes is called Kerr-lens mode-locking (KLM), also sometimes called "self mode-locking" [22]. This uses a nonlinear optical process, the optical Kerr effect, which results in high intensity light

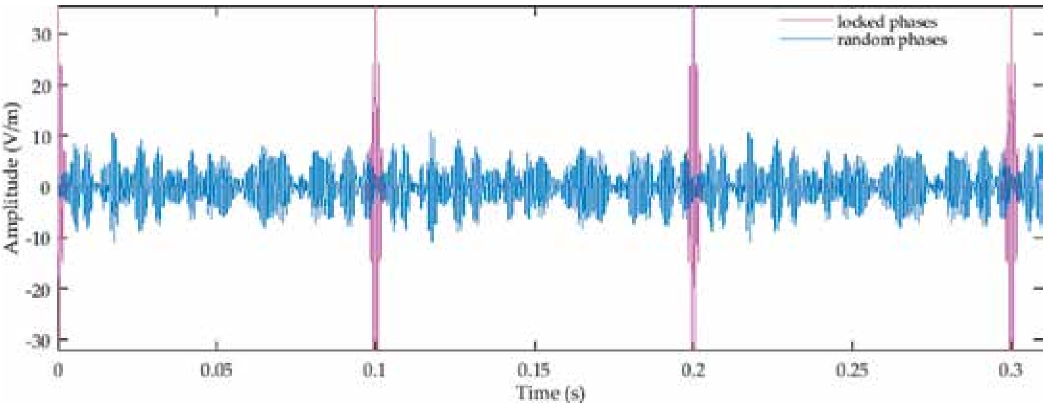

Figure 6. Mode-locking technique. Temporal evolution in a laser with random and locked phases.

being focused differently than low intensity light. By careful arrangement of an aperture in the laser cavity, this effect can be exploited to produce the equivalent of an ultrafast response time saturable absorber.

Q-switching is widely used technique in generating of energetic pulses in the picosecond to nanosecond regime [10]. These short pulses are achieved by rapidly increasing and decreasing of the laser resonator Q factor. In a low Q sate, the cavity loss, controlled by intracavity loss modulators, is such a high that lasing cannot be inhibited. Consequently, pump power builds up the inversion population, pumped several times above the threshold inversion up to its peak value, when the laser cavity Q factor switches to its high value. Because of removed intracavity loss, manifesting itself by the large gain, a high energy pulse is quickly produced and in the meantime the population is drained by the pulse [32].

The resonator losses can be switched in different ways: actively, by an active control element driven by an external electrical generator, typically either an electro-optic or an acousto-optic modulator [33], or passively [34] by some kind of saturable absorber, such as semiconductor saturable absorber mirrors (SESAM), graphene [35], quantum dots [36], carbon nanotubes (CNT) [37], and topological insulator [38].

Q switched fiber lasers are widely applied in microsurgery of soft biological tissues [34], biomedical diagnostics [35], surgery [36], and chemical bond spectroscopy [39]. Short and ultrashort pulses possess specific advantages over continuous-wave (cw) operation, enabling cleaner ablation of materials in medical surgeries.

It should also be pointed out that creating of ever-shorter optical pulses has been a topic of extensive research since the advent of pulsed laser sources. However, motivated primarily by scientific curiosity, ultrashort pulses have been put forward because of some important benefits for technical and industrial applications. For now, passive mode locking is one of the key methods of ultrashort pulse generation. Today's ultrafast light sources devices produce pulses of peak output powers on the order of a megawatt, directly from a simple laser. For many experiments, however, a peak power of a megawatt is not sufficient, making it necessary to increase the energy of these pulses. On the other hand, achieving short duration and high energy of the pulses, at the same time, is undoubtedly more striving than improving one of these parameters independently because both of those are associated with high field intensity that often makes physical system nonlinear [8]. One of the challenging ways to obtain the higher energy levels of these pulses is Q switched mode-locked (QML) method. QML is the combined Q-switching and mode locking in one cavity and it has also been successfully employed for generation of high energy pulses.

3. Classification of fiber lasers for medical purposes

As it was pointed out before, medicine is an eminent consumer of fiber laser technology from surgery and therapy to diagnostics and imaging. Driven by the huge demand, based primarily on the recognition of the need for better healthcare, fiber laser technology has shown tremendous growth in advancement and innovations in recent years. Nowadays, fiber lasers are widely recognized as unique light sources for many medical applications due to advanced features such as high beam quality, superior performance, and extreme power efficiency concurrently with low cost of ownership.

Broad-scale research has led to a wide diversification of fiber lasers in their operating modes, wavelengths, and energy levels. Consequently, in medical science, fiber lasers are no longer in their initial stages of development. They should be rather considered as promising tools for modernization in medicine, because every invention in this field may be a valuable step toward achieving less invasive or less painful medical technologies.

Medical fiber lasers can be classified according to several criteria, such as, output characteristics, safety, the reaction of the organic tissue, host media, gain media, emission wavelength, etc. The first classification refers to temporary regimes, which have been adequately explained in the previous section, while the second one categorizes fiber lasers according to potential risk of adverse health effects and it can be quite helpful in selection of appropriate control measures to minimize the risks [40]. However, it is to be pointed out that, in practice, the risk also depends upon the conditions of use, exposure time, and the environment.

3.1. Ablative versus non-ablative fiber lasers

The interaction of the laser beam with leaving tissue is manifested through several important effects, which are summarized in **Table 1**.

In this context, fiber lasers can be categorized in the basis of those effects. In spite of a far greater number of groups, for practical reasons, two groups, referring to the optical and the thermal responses, are widely accepted by medical authorities. According to the categorization is shown in **Diagram 1**, the first group of fiber lasers employs optical processes such as selective resonant absorption, fluorescence, reflection, elastic scattering, inelastic scattering, and transmission. In subsequent studies, the fiber lasers are designated with a term non-ablative. The thermal effect of laser irradiation is so small that could not damage or destroy the irradiated tissue. Such fiber

Temperature	**37–60°C**	**60–65°C**	**90–100°C**	**37–60°C**	**~100°C**	**Beyond 100°C**	
Chemical and physical effects	Heat/ increased diffusion	Denaturisation Coagulation	Phase change	Carbonization		Vaporization Verbrennung	Shockwave plasma
Optical effects	Scattering refraction reversible	whitening Scattering Destruction of structures	Scattering Shrinking	Darkening Increased Absorption		Gases vapor	Vapor debrises
Biological results	Stimulation	Demage	Shrinking		Heavy demage		Mechanical Demage

Table 1. Effects of the interaction of the laser beam with leaving tissue.

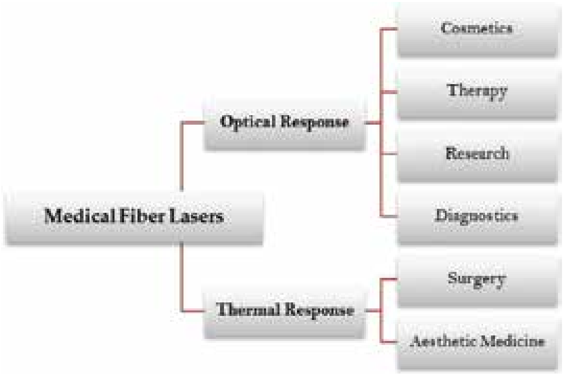

Diagram 1. A classification of fiber lasers depending upon the reaction of the tissue.

lasers are widely used in therapy [41–43], diagnostics [44–46], cosmetics [40, 42], and research [47, 48]. The second group refers to the thermal response and members of this group are often called ablative fiber lasers. According to applications, the group is sub-divided into two classes: the first one is used in various types of surgery [49–51], while the second one is used in esthetic medicine such as skin rejuvenation or resurfacing [52, 53].

Before classifying fiber lasers, according to active medium, the chapter will be continued with discussion of most prominent host media, which has an important role in medical applications. In this context, it could be very helpful to explain what the host media is as well as what the criteria for selecting appropriate host media are.

3.2. Host media

As the chapter will be continued with discussion of most prominent rare-earth elements and prominent host media, which are of crucial role in medical applications, it could be very helpful to explain what the host media is as well as what the criteria for selecting appropriate host media are.

As it is said before, the population inversion that is essential for the stimulated emission of photons cannot be produced without presence of the dopant atoms placed in some of host media. The host media can be defined as a laser gain media doped with rare-earth ions. In the host medium, the rare-earth ions replace host ions which have a similar size and the same valence. The pump and laser transitions of all rare-earth-doped gain media have fairly small oscillator strength and are known as weakly allowed transitions. So, the host media removes the limits regarding the stabilization or the coherence of the pumping source what means that the pumping source does not need to be of a single frequency [25]. Their upper state lifetime, which provides the storage of the substantial amounts of energy in some media, is consequently long. This distinguishing property makes rare-earth-doped media convenient for mode-locking and Q-switching.

The strong demand in optical communication has triggered the successful development of the host materials and increased their diversity. Nowadays, the most challenging host media are crystals or glasses, and there is ongoing development in testing and fabrications of new ones. Although silicate glasses remain the most prosper media, the majority of silicate glasses seem to be unsuitable for lasing at long wavelengths. Tellurite, Chalcogenide, and Fluoride (especially ZBLAN) glass are largely employed in the field of optical sources could in the mid-infrared region [9].

3.3. Active media

An understanding of a laser and optical amplification process is closely related to understanding of the nature of light and the interaction between electromagnetic radiation and matter, which is the basis for studies of more complex quantum mechanical systems, including those of fiber lasers [54]. The operation of laser process is based on amplification of light stems from absorption, spontaneous, and stimulated emission of radiation as the fundamental mechanisms common for all laser actions. During the lasing process, stimulated photons promote further stimulated photons in a cascade, resulting in sustained gain, if several conditions are met. The first condition is achieved at population inversion, which is an important term closely related to the operation of laser. Under thermal equilibrium conditions, emission process which competes with stimulated absorption so weak that it cannot provide amplification of a beam of light is stimulated. Amplification is carried out when the rate of the stimulated emission is so increased that the number of atoms in the upper level is larger than that of atoms in the ground level. The requirement for population inversion imposes other two conditions: adequate pumping process by an external energy source, which has higher energy than the upper energy level, and minimum two participating energy levels where the process can take place. Although the two-level system appears as the most simple and straight-forward method to establish the population inversion, it is not useful as it does not lead to laser action [31]. Consequently, the other pumping schemes become more important and widely employed. According to the arrangement of those energy levels within dopant ions, lasing schemes are typically classified as a two, three, quasi-three, and four-level schemes [55].

Fiber lasers can amplify incident light via stimulated emission, provided by the optically pumping in order to obtain population inversion that caters for the optical gain. The population inversion, essential for the stimulated emission of photons, can be brought forth by electrons of the dopant atoms, obtained from one or more luminescent rare-earth metals [12]. Attractiveness of those elements lies in their distinguishable optical characteristics refers to emitting and absorbing processes over narrow wavelength ranges, which are relatively insensitive to host material, longer lifetime of metastable states, and higher quantum efficiencies. Although the rare-earth group consists of 2 groups of 14 elements each, the rare-earth ions referred to as lanthanides that fill the 4f shell and occupy the atomic number 58–71 of the periodic table. The most common rare-earth elements with some of its basic atomic properties, common host media, and important operating wavelengths are explained in short below.

3.3.1. Erbium-doped fiber lasers

Erbium, mainly involved by Er^{3+} ions, has optical fluorescent properties that are particularly convenient for some laser applications. Er-doped fiber laser application technology has seen substantial progress since its invention in the late 1980s. Refers to hosting media, it can be said that different glass hosts are preferable for different purposes. Silica glass is the most widely used host material in telecom, while Tellurite and ZBLAN glasses, are preferable in mid-IR region, where Er^{3+}-doped fiber lasers utilized in the field of optical sources, applied in various areas among of which is an optical coherence tomography [9]. Similarly, absorption region between 2.5 and 4 μm, where Er-doped fiber lasers have sparked a huge interest, due to evident opportunities for sensing and the highly precise modification of biomedical and industrial material [56, 57]. There are some evidences that Er-doped fiber lasers at used in medical endoscopy [58] and surgery [58, 59]. Phosphate glasses also regarded as better ones due to their higher phonon energy and better solubility of Er^{3+} ions [60].

Emission and absorption cross sections for erbium in phosphate glass host media [15] are illustrated in **Figure 7a**, while an energy level diagram of some common optical transitions of Er^{3+} is shown in **Figure 7b** [12, 13]. In the optical amplification media, made from erbium-doped crystals or glasses, electrons of Er^{3+} ions are optically pumped at the vicinity of 980 or 1480 nm and excites into the $^4I_{11/2}$ or $^4I_{13/2}$ states, respectively. Then, light can be amplified in ranges from 1530 to 1560 nm, via stimulated emission, where the ions show strong three-level state behavior and the maximum gain is reached [61].

It is to be noted that it is difficult to realize an efficient pump absorption on the $^4I_{15/2}$–$^4I_{11/2}$ transition due to relatively small absorption cross sections and limited doping concentration that is confined by quenching processes. This problem is commonly solved by co-doping with Yb^{3+} sensitizer ions. In those co-doped systems, pumping is absorbed via Yb^{3+} ions that provide subsequent energy transfer to Er^{3+} ions that support stimulated emission in 1520–1650 nm spectral range [11, 23]. It is to be pointed out that 1550 nm wavelength, which is of especially importance for optical communications as loss of the standard single mode for optical fibers is minimal at this particular wavelength [27], is also used for the removal of café-au-lait macules (CALMs) for darker skin phototypes [62] as well as fractional resurfacing [63]. Moreover, 2000–3000 nm range seems very encouraging for microsurgery applications such as glaucoma surgery, vitreoretinal surgery, and myringotomies [64]. Microjoule femtosecond fiber laser at

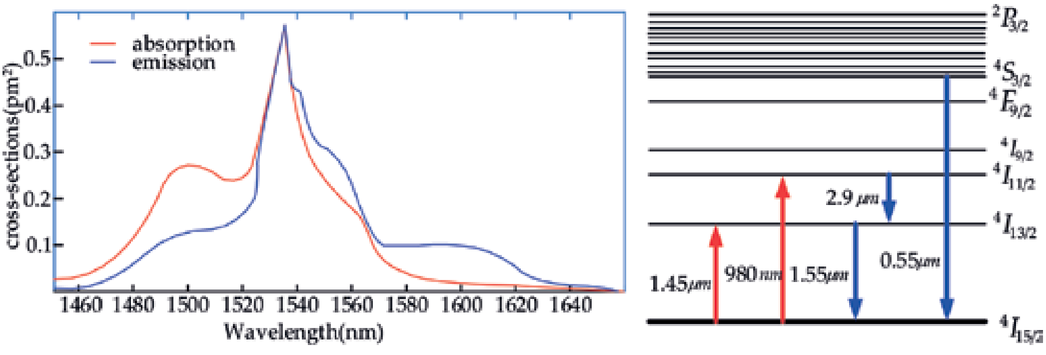

(a) (b)

Figure 7. (a) Emission and absorption cross section for erbium in phosphate glass host media [61]. (b) Energy level structure of Er^{+3} ions and some of the common optical transitions.

1600 nm are used in corneal surgery [65]. Er-doped fiber lasers at 1565 nm wavelength can be used for cosmetic treatments. Particularly, they are appropriate for effective treatment of facial wrinkles [66].

There are two important particular wavelengths for medical proposes at 2800 nm, which is useful for spectroscopy applications [67], and 2940 nm emission, where the erbium ions that is highly absorbed in water [68]. On the other hand, CW and pulsed Er,Pr-ZBLAN and a coupled Yb,Er-silica fiber lasers have been widely researched as a short-coherence-length light source for optical coherence tomography (OCT) between the range of 1000–3000 nm [64].

3.3.2. Thulium-doped fiber lasers

There are several important reasons why Tm-doped fibers lasers are more promising at present. One of them is the possibility of pumping the Tm^{3+} ions at around 790 nm or at 915–975 nm, where efficient high brightness diodes are readily available. Another advantage is the laser operation between 1470 and 1800 nm among wide gain spectrum ranging from 1400 to 2700 nm, which is so-called eye-safe spectral range of optical wavelengths as it can be highly absorbed by water in the eye before reaching the retina [69].

Tm-doped fiber lasers, operating beyond 2 μm would benefit diverse applications. They are good candidates for spectroscopy in mid-IR region, often labeled the molecular fingerprint region, containing the spectral signature of many molecules. For this reason, this spectral region is important for many applications that require high quality laser cutting and welding, such as remote sensing and specific surgical procedures known generically as microsurgery [13, 70]. Although there are a lot of emission bands of Nd^{3+} and Er^{3+} in the same gain spectrum, much of the interest in Tm^{3+} stems from its emission that occurs in the gaps of these bends.

Figure 8a shows an energy level diagram of the most important optical transitions of Tm^{3+}, while its absorption spectra in fluoro-tellurite bulk glass is shown in **Figure 8b** [71]. It is to be noted that around 1900 nm $^3F_4 \rightarrow {}^3H_4$ transition is a quasi-three-level transition but as wavelength draws close 2100 nm transition is turned to a four-level one [23].

Tm has three important extremely broad absorption bands: $^3H_6 \rightarrow {}^3F_4$, $^3H_6 \rightarrow {}^3H_4$, and $^3H_6 \rightarrow {}^3F_4$. 790 nm pump sources, which are more widely used, pump Tm^{3+} ions from $^3H_6$ to $^3H_4$ state, 1064 and 1319 nm pump sources are used for $^3H_5$ band pumping, while 1570 nm pump sources excite Tm^{3+} ions to $^3F_4$ the main metastable level. Although the highest theoretical slope efficiency, with respect to absorbed power, is expected for 1570 nm sources due to the lower quantum defect, the reality is quite different. That is to say, 790 nm pump sources have much higher theoretical slope efficiency, of 82%, due to doubling through a cross-relaxation process. This phenomenon, known as "two-for–one" occurs as a result of one pumping photon excites two Tm ions [23].

All Tm-doped silica fibers, yet reported, have been utilizing $^3H_4 \rightarrow {}^3F_4$ at transitions at 1487 nm followed by $^3F_4 \rightarrow {}^3H_6$ at 1800 nm. The first transition is of special importance for resonant pumping of Er-doped lasers and amplifiers. Tm has enormous bandwidth with wavelength between 1700 and 2100 nm ranges that makes Tm good candidate for source for generation

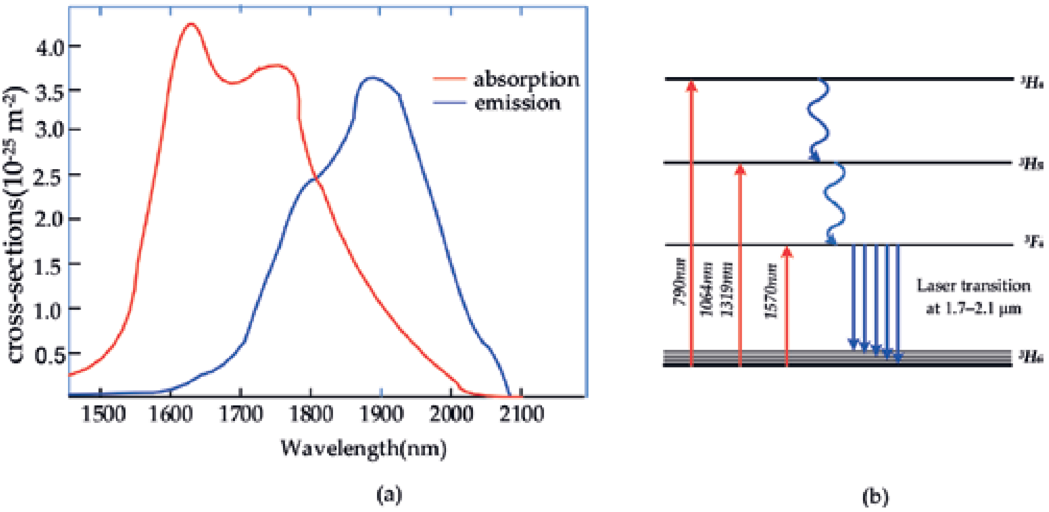

(a) (b)

Figure 8. (a) Measured absorption and emission cross-section spectra of the Tm^{3+}-doped silicate fiber. (b) Energy level structure of Tm^{+3} ions and some of the common optical transitions [71].

of femtosecond pulses [72]. Emission band around 1900 nm is not only appropriate for spectroscopic and chemical sensing applications but it is also very attractive in tissue welding and ablation [73], while 1940 nm is thought to be a good scalpel for precise soft tissue surgery [74].

The power output and efficiency of the fiber lasers steadily have risen since 1998. Moreover, this progress has been speeded up with the realization that the Tm doping level could be increased with the addition of Al co-doping of the core. Although the efficiency of Tm-doped lasers not yet compete with the efficiency of Yb-doped lasers, applications at mid-IR wavelengths as well as pulsed applications appear to be key advantages for further improvements.

3.3.3. Holmium-doped fiber lasers

Holmium (Ho) and Ho-doped fiber lasers have attracted tremendous interests in scientific community due to potential operation with high power levels at wavelengths beyond 2.1 μm in addition to wide spectral tunability, which make them an ideal choice for a variety of medical lasers and promising tools for applications in spectroscopy [75].

The effective gain cross section as a function of inversion and relevant energy levels of Ho^{3+}-doped silica are illustrated in **Figure 9a** and **b**, respectively [76]. The most commonly used pump bands are: 1.15 μm, and 2.046 μm, and 2.1 μm, which are absorbed $^5I_8 \rightarrow {}^5I_6$, $^5I_8 \rightarrow {}^5I_7$, and $^5I_8 \rightarrow {}^5I_6$ transitions, respectively. Important emission transitions are labeled in **Figure 8a**. The two of them deserve special attention. These are: $^5I_7 \rightarrow {}^5I_8$ and $^5I_6 \rightarrow {}^5I_7$ transitions produce radiation in the range of 2050–2850 nm, respectively. At 2860 nm Ho^{3+}-doped fiber lasers overlap more strongly than their counterparts. Hence, they are thought to be a more practical tool for interaction with biological tissues [77].

Comparing to $^5I_7$ level, short lifetime of $^5I_6$ level is considerable obstacle for population inversion. According to research, the stimulated emission from this transition state can be achieved in two ways: by simultaneously allowing the lower transition ($^5I_7 \rightarrow {}^5I_8$) at 2.1 μm to also

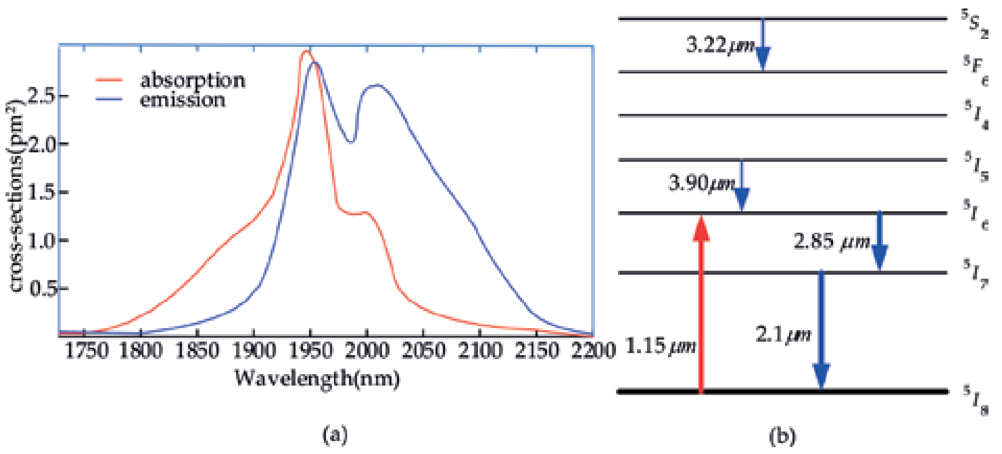

Figure 9. (a) Measured absorption and emission cross-section spectra of the Ho^{3+}-ions. (b) Energy level structure of Ho^{3+} ions and some of the common optical transitions [3].

emit light or by co-doping by another dopant (typically Pr^{3+}) to hold the $^5I_7$ level depopulated through energy transfer processes. The first one provides the possibility of dual wavelength pulsing in ~2 μm and ~3 μm emission bands [76].

Besides that, Ho-doped fiber lasers are appropriate for ureteroscopy and stone treatment because of quite efficient stone fragmenting regardless of the composition [78]. About 2-μm CW Ho-doped fiber lasers are proposed for surgery because of using the contact method [79].

3.3.4. Ytterbium-doped fiber lasers

The absorption and emission cross sections and spectra of Yb^{3+} for silica host media are illustrated in **Figure 10a**, while pumping and amplification involve transitions between different sublevels of the manifolds are shown in **Figure 10b**. An abnormally high emission cross section, combined with diversity of the available pumping sources, resulting from broad absorption band and especially the narrow absorption peak at 975 nm, provides generation of many wavelengths of general interest. Exciting of the electrons to the higher energy achieved by interaction with near-infrared or visible photons [81]. Another advantage of Yb^{3+} ions is a remarkable simplicity of the electronic level structure, in comparison with other rare-earth ions. Yb^{3+} ions have two relevant manifolds: a ground-state, $^2F_{7/2}$, with four sublevels, and a metastable state, $^2F_{5/2}$, consists of three sublevel [82].

For short wavelengths around 990 nm, Yb^{3+} ions show three-level system behavior, whereas, at wavelengths between 1000 and 1200 nm, they behave as nearly pure quasi-four-level systems [15]. These combined features are of crucial importance for very short fiber lasers with high pump absorption. Some research show that, at 1070 nm, pulsed fiber laser could be very useful in oral surgery due to superiority related to thermal elevation in the irradiated tissues [83].

In regard to medical applications, although it usage in femtosecond laser micromachining, from waveguide fabrication to cell ablation, should not be underestimated, it is rather utilized as a sensitizer in co-doping of Er^{3+}-, Tm^{3+}-, or Ho^{3+}-doped fiber lasers to demonstrate near and

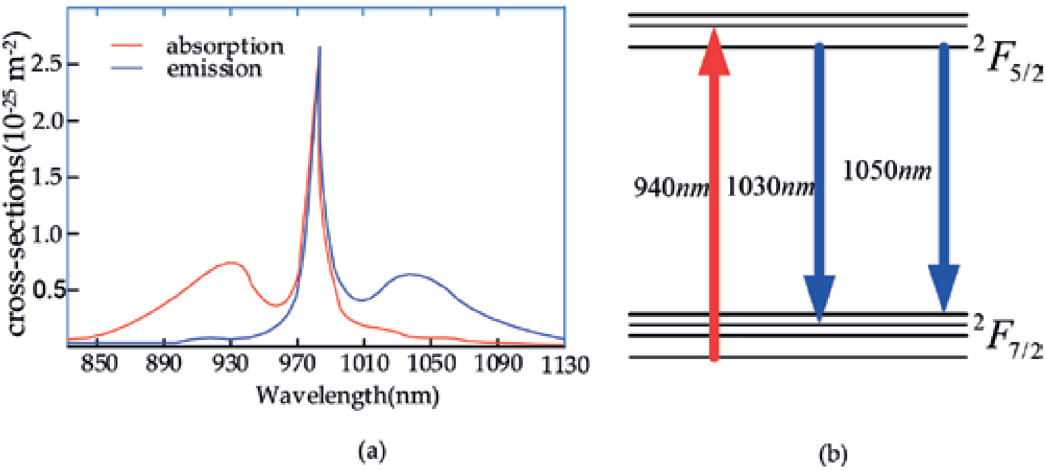

Figure 10. (a) Ground-state absorption and emission cross-sections and spectra of Yb^{3+} in silica. (b) some common optical transitions of Yb^{3+} ions [80].

mid- infrared emissions at around 1.545, 2.05 and 2.9 µm wavelengths, respectively, appropriate for chemical sensing [2]. Moreover, there is some evidence that, at a wavelength of around 1000 nm, Yb^{3+}-doped fiber lasers can be used as short coherence light sources is in optical coherent tomography, used for ophthalmology [84]. Additionally, according to reports by scientists from Ultrafast Optics & Lasers Laboratory, Bilkent, there are some already developed Yb-doped fiber laser configurations, appropriate for high precision processing of both hard and soft tissue. The hard tissue experiments were performed on dentine (human toot sample), while the soft tissue experiments were focused on brain tissue removal and corneal flap cutting. It has been pointed out that the operation of the custom-developed fiber laser is provided through either uniform repetition rate pulse or ultrafast burst-mode regimes [85].

In the recent years, Yb-doped fiber lasers have been also widely used in MOPA configuration with various pulse duration and repetition rates for creating novel laser configurations, which can be attractive solutions for many medical applications, such as fluorescence analysis of biological molecules [86] and photoacoustic microscopy [87]. It is to be pointed out that MOPA configurations have been also under research for photoacoustic imaging (PAI), in order to substitute currently available Nd:YAG laser, targeting 150 times faster imaging [88]. Femtosecond Yb-fiber laser with MOPA configuration at 1035 nm can be a part of widely tunable Cherenkov fiber lasers used in both confocal and super-resolution microscopy [89].

4. Some examples of medical applications

4.1. Fiber lasers in photodynamic therapy

Photodynamic therapy (PDT), a simple scheme of which is illustrated in **Figure 11**, also referred to as blue light therapy, is a treatment modality that utilizes light sensitive molecules, photosensitizers, activated by adequate kind of light, commonly generated by laser

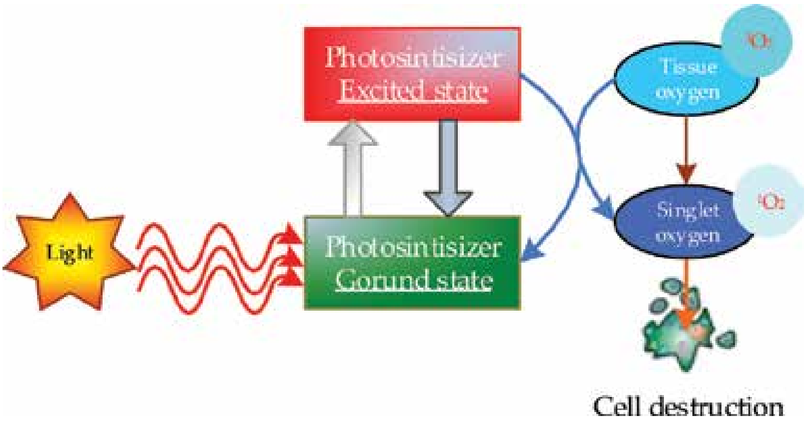

Figure 11. Photodynamic therapy.

sources, to cause the formation of singlet oxygen, producing peroxidative reactions that can cause damage and death of abnormal or neoplastic cells [90]. In addition, PDT is currently used in cosmetic surgery, oncology, oral medicine, and ophthalmology [91]. Although being primarily developed for cancer treatment, at the outset, usage in oncology usage was confined to a few specific cancer kinds, such as non-small cell lung cancer and esophageal cancer. However, further investigation has revealed that PDT can be quite convenient for general oncology for conditions including cancers of the peritoneal cavity, prostate gland, cervix, and brain [92].

PDT is a noninvasive or minimal invasive alternative techniques for conventional, more systematic, treatment of tumors, consists of surgical resection, radiotherapy and/or chemotherapy, which is developed to target tumor itself by light-induced activation of a photosensitizer that selectively accumulates within neoplastic tissue. As a promising treatment for selective tissue destruction, PDT has attracted widespread attention from the entire scientific community since, comparing to radiation therapy, it offers more patient-comfortable cancer treatment without cumulative long-term complications. PTD is a dynamic process, which requires careful administration of interaction of all principal components. The distribution of light, determined by the light source characteristics and the tissue optical properties, is in interaction with photosensitizer and oxygen concentrations since they influence the tissue optical properties. On the other hand, the distribution of oxygen is in closely relation with the photodynamic process since the photodynamic process is an oxygen consummator, which is, in turn, influenced by the distribution of photosensitizer. That is to say, well-administrated PTD requires optimal photosensitizers, smart transport strategies, and activation by adequate light source [93].

Over the last several decades, research focused on better understanding of the basic biophysical mechanisms of light transport and delivery in tissue, has led to diversification of photosensitizing agents, and light sources as well, which in turn has brought about a valuable progress in PDT in terms of the light penetration depth in the skin tissue. Hence, it seems that poor skin penetration depth of around 1 cm that diminish ability of the light to target deeper cells could be overcame.

In PDT, light sources, which are used as a spatially and temporally precise stimulus, typically operate in the 600–800 nm range. This visible and NIR spectral zone, also known as the therapeutic window, has the advantages in light transport and delivery in tissue. The other superiorities of aforementioned region are reducing pain, inflammation, and edemas as well as preventing tissue damage. Although nowadays there is diversified amount of light sources that can be used, lasers are quite prominent ones because obtained monochromatic light could be easily coupled into optical fibers in order to get up to deeper regions. At this point, practical advantages that fiber lasers offer over other types of lasers, such as inherently more efficient coupling, compactness, flexibility, and high beam quality as well as lower running costs, may overcome key clinical limitations of PDT related to delivery of optical energy and afford new opportunities for PDT. It is to be pointed out that early lasers were based on argon laser, gas vapor laser-pumped dye laser, or Nd:YAG solid-state lasers. Nowadays, they are replaced by diode-pumped fiber lasers, 1540 nm non-ablative fractional erbium-doped fiber laser [94, 95], 1927-nm thulium fiber lasers, and quantum dot (QD) fiber laser [43, 96, 97].

4.2. Fiber lasers in biomedical sensing—mid-infrared spectroscopy

Quite a few diseases can be detected by monitoring consequential metabolic abnormalities through the quantification of the serum biochemical components, such as urea, globulins, enzymes, glucose, cholesterol, triglyceride, and albumin. Hence, numerous biochemical methods have been developed to quantify, and more rarely characterize, specific serum components. However, most of those offer information on a particular component rather than a combination of several biochemical parameters. In this context, identifying serum fingerprints via MIR spectroscopy, from a rather small amount of sample, can provide more extensive view on the serum biochemical species levels, which, in turn, can facilitate diagnostic procedure.

The middle-infrared (MIR) region spanning 2500–10,000 nm of electromagnetic spectrum is proved to be very useful in spectroscopy, for quantification of the composition of the sample by means of light, particularly in clinical chemistry [98]. Broad spectral coverage of the region provides opportunity for sensing a great deal of molecules, including molecules of biological tissues, where they can be recognized with great sensitivity. Until recently, challenges, such as poor coherence of light sources, troublesome sensing due to highly attenuated backscattered sign as well as a luck of low noise MIR detectors were insurmountable obstacles especially in vivo spectroscopy [99]. However, over the last few years, advances in material science, in addition to diversifying and miniaturizing of photonic components have paved the way for enhancing novel light sources, with previously unattainable performance capabilities, which have improved accuracy of measurements to a great extent. As result, MIR spectroscopy has been consolidated and put on center stage again.

Refers to the physical principle, MIR spectroscopy utilizes fundamental molecular vibrations, such as bending and stretching, of a specific bond or bonds within the molecule under study generally caused by matching quantized energy difference of transitions between the ground state and the first excited state. Its high sensitivity to polar groups is the result of the same oscillation frequency of the molecular dipole moment and electric field vector of the source light [147]. Furthermore, the “fingerprint” region has a quite strong absorbance, with numerous and well resolved absorbance peaks, differing in position, width, and intensity providing unique absorption patterns for each constituent, which enable direct constituent identification at a molecular level. The MIR region is quite suitable for identifying C-C, C-O-H, and C-H groups for asymmetrical and symmetrical stretching's [100]. However, MIR light only penetrates up to 100 μm into human skin due to the strong water absorption [97]. Problem of limited penetration has been partially avoided by application of multivariate data-analysis techniques.

The basic setup of the MIR measuring instrument consists of a light source, an optical assembly and a light detector unit. A high spectral brightness, tight focusing characteristic for a spatially coherent, laser-like beam as well as high average power is common requirement for the all spectroscopy schemes. Until the last decade, the most preferred laser sources were CO_2 laser and vertical-cavity semiconductor laser (VCSEL) [101]. However, their complexity and high costs got research to charge direction toward tunable semiconductor lasers, such as: quantum cascade laser (QCL) and external cavity quantum cascade laser (Eq-QCL) [102]. In the last years, in several researches, it has been pointed out that supercontinuum generation light sources and some mode-locked oscillators can be quite encouraging as they span exceedingly MIR region [103]. Refers to light detection unit, there are several kinds of photodetectors widely used in this region, chosen depending on measuring technique. Lately, the most remarkable sensor types have been small fiber-based on attenuated total reflectance (ATR), and photoacoustic sensors. ATR has still been a monopoly technique in analyzing the sample.

Figure 12 shows example setup used by Liakat and colleagues, where glucose MIR spectra are collected from wrist skin. Hollow core fiber, particularly suited for delivery of picosecond pulses with high average and high peak power, is used for both delivery of QC laser light and collection of backscattered light, coupled directly to a MCT detector. The lock-in amplifier, which provides amplifying and measuring of phase and frequency locked output, has reference frequency of 55 kHz. Finally, the output of lock-in amplifier is recorded by computer, where date is processed.

Up to now, most of drawbacks refer to MIR spectroscopy have been in large part overcome. Although some of them, such as high sensitivity to external factors and sudden drop in available energy with increasing wavelength, still remain important challenges keeping ahead more strongly reconsideration and practical implementation, there is a strong believe that MIR spectroscopic techniques is one of the forefront candidates for a viable future solution

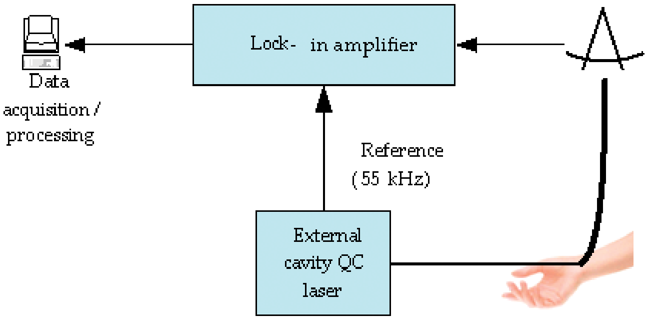

Figure 12. Setup used for collecting data from human skin [104].

with a few advancements and adaptations. In this sense, it has been pointed out that possible step toward could lay in fortifying MIR spectroscopy with some other technique or using alternative measuring technique with MIR light source.

4.3. Fiber lasers in dentistry

Comparing to other areas of medicine, the introduction of lasers into dentistry lagged mainly due to some skepticism by a majority of dentists and correspondingly predominance of long-standing clinical dogma of clinical techniques. Hence, although the original Nd:YAG was launched as a soft tissue laser primarily for dental purposes, the real expansion in laser usage began when professionals began recognizing a need for a hard tissue laser, so that, the laser technology in dentistry emerged with introduction of the Er: YAG laser, as an alternative to the rotary drill.

In the last decades, lasers have become more and more important in dentistry. From a patient point of view, the treatment performed by lasers are very beneficial primarily because of quicker and more efficient dental care accompanied with notably reduced pain during the treatment, less need of anesthesia, reduced post-treatment pain, and shorter post-treatment recovery period. Refers to the practitioner, one of the main arguments in favor of laser-assisted dental surgery is better efficiency due to generally shorter treatment procedures as well as less complex and time consuming pre and post-procedure protocols. The requirements of the output from lasers used for dental applications are manifold. Besides the essential attributes such as the pulse energy, output power, and wavelength, laser must have some other practical qualities such as the size, input power, tightness of the focus of the output, and maintenance level.

Lasers used in dental practice are usually classified according to tissue applicability into: hard tissue and soft tissue lasers. Er: YAG and diode lasers have proven their value for many dental procedures, both as surgical and therapy tools, with added benefits in a wide range of applications. In spite of high price, the Er:YAG is still one step ahead because of its elevated absorption in water, which makes it adequate for both treatment of dental hard tissues and soft tissue ablation. On the other hand, diode lasers having several advantages, such as reduced size, reduced cost, and possibility to beam delivering by optical fibers, are more appropriate for the soft tissue treatments.

According to research, fiber laser technology has been trying to break up Er:YAG and diode lasers' monopolies in the dentistry market, for almost two decades. In spite of is a growing trend in usage of fiber lasers in oral surgery, expected outcome has not been reached yet. However, there is no depth that benefits, such as compactness, high reliability, low cost, high beam quality, and power efficiency could pave the way for fiber lasers to compete with Er:YAG and diode lasers in terms of pulse energy. In this context, ex vivo study for 1070 nm fiber lasers, carried out on both tissues and materials, could be one of the promising results due to reduced thermal elevation in the irradiated tissues, thanks to the possibility of emission in ns pulse duration, limiting the collateral damage due to the overheating of the target [41]. Custom-developed laser system, developed by UFOLAB, Bilkent, illustrated in **Figure 13**, is another encouraging

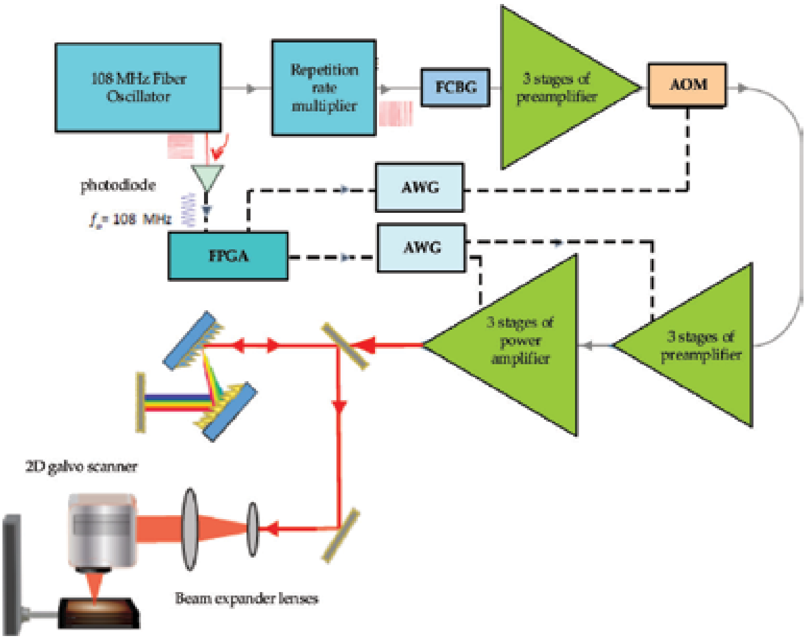

Figure 13. Laser, optical scanning, and sample positioning setup custom-built for the hard tissue and piezoelectric ceramic cutting experiments [105].

study, in which an in-house developed Yb-doped fiber burst-mode laser amplifier system with an adjustable in-burst repetition rate is seeded by an all-normal dispersion laser oscillator generating a mode-locked signal at a repetition rate of 108 MHz as the seed source. The system with central wavelength of 1035 nm is set up for hard and soft tissue treatment [106].

However, it is to be pointed that usage of lasers in daily dentistry is not confined to tissue treatment; it is also extended to anti-bacterial applications as well as surface texturing or coating for modification of surface properties of various materials, such as titanium-based dental implants and disilicate ceramics. Although the dental industry is not the largest industry to be using fiber lasers, their biggest impact on this industry might be the way in which the tools and equipment used by dental surgeries can be manufactured.

5. Conclusion

The purpose of this chapter is not only to provide an overview on theoretical basis but also revise existing classification schemes of fiber laser technology for medical purposes. It is to be stressed that our theoretical framework is concerned with basic concepts that are relevant for fiber laser technology in medical field. The second part of the chapter is devoted to classification of medical fiber lasers according to several criteria, the most prominent of which is host media and with relevant emitting wavelengths of special proposes.

The idea of using light in therapeutic purposes is not a new one. It is widely believed that sunlight was used as a therapy by the ancient Greeks and Egyptians. However, the idea has become reality since laser invention. In the past two decades, lasers have gradually found a place in the practice in many areas of medicine and biomedical research. Recently, they have already found their way into cosmetic surgery and oncology. Now, they are becoming important tools for a large number of applications with microscale accuracy, in branches such as nanosurgery and ophthalmology. Fiber lasers have also unique places in family of coherent light sources and they make their presence felt in vivo sensing. As example, applications of mid-IR light to noninvasive in vivo sensing systems yield robust and clinically accurate ones that got rid of boundaries set in the past. It has been highlighted that in near future it will be possible to achieve immense amount of cellular-related information. Recently, improved cancer diagnosis via lasers that illuminate cellular activity has been reported. Additionally, in near future, light will play a very important role in solving energy life sciences challenges. Fiber laser technology seems to come to take medical market share away from their merged counterparts.

Thanks

I am extending my thanks to Hamit Kalaycıoğlu and other scientists from Ultrafast Optics & Lasers Laboratory, Bilkent, for sharing their researches as well as invaluable feedback during the preparing of this chapter.

Author details

Amira Tandirovic Gursel

Address all correspondence to: agursel@adanabtu.edu.tr

Adana Science and Technology University, Electrical and Electronics Engineering,
Adana, Turkey

References

[1] Agrawal G. Applications of Nonlinear Fiber Optics. Academic Press; 2001

[2] Balaji S, Gupta G, Biswas K, Ghosh D, Annapurna K. Role of Yb 3+ ions on enhanced ~2.9 µm emission from Ho 3+ ions in low phonon oxide glass system. Scientific Reports. 2016;**6**:29203

[3] Azooz SM. Development of Dual-Wavelength and Pulsed Fiber Lasers Based on Thulium-Doped Fibers. University of Malaya; 2015

[4] Agrawal GP. Fiber-Optic Communication Systems. Vol. 222. John Wiley & Sons; 2012

[5] Csele M. Fundamentals of Light Sources and Lasers. John Wiley & Sons; 2011

[6] Fermann ME, Hartl I. Ultrafast fibre lasers. Nature Photonics. 2013;**7**:868

[7] Duarte FJ. Tunable Laser Applications. Vol. 150. CRC Press; 2008

[8] Hudson DD. Mode-Locked Fiber Lasers: Development and Application. University of Colorado at Boulder; 2009

[9] Falconi MC, Laneve D, Prudenzano F. Advances in mid-IR fiber lasers: Tellurite, fluoride and chalcogenide. Fibers. 2017;**5**:23

[10] Dong L, Samson B. Fiber Lasers: Basics, Technology, and Applications. CRC Press; 2016

[11] Koester CJ, Snitzer E. Amplification in a fiber laser. Applied Optics. 1964;**3**:1182-1186

[12] Digonnet MJ. Rare-Earth-Doped Fiber Lasers and Amplifiers, Revised and Expanded. CRC press; 2001

[13] Urquhart P. Review of rare earth doped fibre lasers and amplifiers. IEE Proceedings J (Optoelectronics). 1988;**135**:385-407

[14] Zervas MN, Codemard CA. High power fiber lasers: A review. IEEE Journal of Selected Topics in Quantum Electronics. 2014;**20**:219-241

[15] Paschotta R. Encyclopedia of Laser Physics and Technology. Vol. 1. Wiley-vch Berlin; 2008

[16] Tünnermann A, Schreiber T, Röser F, Liem A, Höfer S, Zellmer H, et al. The renaissance and bright future of fibre lasers. Journal of Physics B: Atomic, Molecular and Optical Physics. 2005;**38**:S681

[17] Tünnermann A, Schreiber T, Limpert J. Fiber lasers and amplifiers: An ultrafast performance evolution. Applied Optics. 2010;**49**:F71-F78

[18] Jeong Y, Nilsson J, Sahu JK, Dupriez P, Codemard CA, Soh DBS, Payne DN. High power fiber lasers. Presented at the Optical Fiber Communication; 2005

[19] Samson B, Carter A, Tankala K. Doped fibres: Rare-earth fibres power up. Nature Photonics. 2011;**5**:466

[20] Limpert J, Roser F, Klingebiel S, Schreiber T, Wirth C, Peschel T, et al. The rising power of fiber lasers and amplifiers. IEEE Journal of Selected Topics in Quantum Electronics. 2007;**13**:537-545

[21] Kouznetsov D, Moloney JV. Efficiency of pump absorption in double-clad fiber amplifiers. II. Broken circular symmetry. JOSA B. 2002;**19**:1259-1263

[22] Koechner W, Bass M. Solid-State Lasers: A Graduate Text. Springer Science & Business Media; 2006

[23] Ter-Mikirtychev V. Fundamentals of Fiber Lasers and Fiber Amplifiers. Springer; 2014

[24] LiuXEA. Development of diode lasers for pumping high power ultrashort pulse lasers. Presented at the IEEE CLEO/PACIFIC RIM'09 Lasers and Electro-Optics Conference; 2009

[25] Prajzler V, Lyutakov O, Huttel I, Oswald J, Jerabek V. Optical and spectroscopic properties of polymer layers doped with rare earth ions. In: Advances in Lasers and Electro Optics. Rijeka: InTech; 2010

[26] Maini AK. Lasers and Optoelectronics: Fundamentals, Devices and Applications. John Wiley & Sons; 2013

[27] Nilsson J, Payne DN. High-power fiber lasers. Science. 2011;**332**:921-922

[28] Esser M. Diode-end-Pumped Solid-State Lasers. Stellenbosch: University of Stellenbosch; 2005

[29] Polynkin P, Temyanko V, Mansuripur M, Peyghambarian N. Efficient and scalable side pumping scheme for short high-power optical fiber lasers and amplifiers. IEEE Photonics Technology Letters. 2004;**16**:2024-2026

[30] Svelto O. Principles of Lasers. 5th edition. Springer; 2010

[31] Jeong Y-C, Boyland AJ, Sahu JK, Chung S-H, Nilsson J, Payne DN. Multi-kilowatt single-mode ytterbium-doped large-core fiber laser. Journal of the Optical Society of Korea. 2009;**13**:416-422

[32] Quimby RS. Photonics and Lasers: An Introduction. John Wiley & Sons; 2006

[33] Li F, Zhu H, Zhang Y. High-power widely tunable Q-switched thulium fiber lasers. Laser Physics Letters. 2015;**12**:095102

[34] Skorczakowski M, Swiderski J, Pichola W, Nyga P, Zajac A, Maciejewska M, et al. Mid-infrared Q-switched Er: YAG laser for medical applications. Laser Physics Letters. 2010;**7**:498

[35] Popa D, Sun Z, Hasan T, Torrisi F, Wang F, Ferrari A. Graphene Q-switched, tunable fiber laser. Applied Physics Letters. 2011;**98**:073106

[36] Lee Y-W, Chen C-M, Huang C-W, Chen S-K, Jiang J-R. Passively Q-switched Er 3+–doped fiber lasers using colloidal PbS quantum dot saturable absorber. Optics Express. 2016;**24**:10675-10681

[37] Chernysheva M, Mou C, Arif R, AlAraimi M, Rümmeli M, Turitsyn S, et al. High power Q-switched thulium doped fibre laser using carbon nanotube polymer composite saturable absorber. Scientific Reports. 2016;**6**:24220

[38] Luo Z, Liu C, Huang Y, Wu D, Wu J, Xu H, et al. Topological-insulator passively Q-switched double-clad Fiber laser at 2$\mu $ m wavelength. IEEE Journal of Selected Topics in Quantum Electronics. 2014;**20**:1-8

[39] Li J, Luo H, Wang L, Zhai B, Li H, Liu Y. Tunable Fe 2+: ZnSe passively Q-switched Ho 3+–doped ZBLAN fiber laser around 3 μm. Optics Express. 2015;**23**:22362-22370

[40] Gupta P. Laser safety: Recommendations for lasers in healthcare. Professional Safety. 2018;**63**:59-60

[41] Fornaini C, Poli F, Merigo E, Brulat-Bouchard N, El Gamal A, Rocca J-P, et al. Disilicate dental ceramic surface preparation by 1070 nm fiber laser: Thermal and ultrastructural analysis. Bioengineering. 2018;**5**:10

[42] Yoo SW, Park H-J, Oh G, Hwang S, Yun M, Wang T, et al. Non-ablative fractional thulium laser irradiation suppresses early tumor growth. Current Optics and Photonics. 2017;**1**:51-59

[43] Mercuri SR, Brianti P, Foti A, Bartolucci M, Dattola A, Nisticò SP. Penile lichen Sclerosus treated with 1927 nm thulium fiber laser and photodynamic therapy: A new possible therapeutic approach. Photomedicine and Laser Surgery. Jan 3, 2018. DOI: 10.1089/pho.2017.4386. [Epub ahead of print]

[44] Taccheo S. Fiber lasers for medical diagnostics and treatments: State of the art, challenges and future perspectives. In: SPIE BiOS. 2017. p. 6

[45] Wang CY, Yu TW, Sung KB. In vivo measurements of optical properties of human muscles with visible and near infrared reflectance spectroscopy. In: SPIE BiOS. 2018. p. 6

[46] Kim J, Campbell AS, Wang J. Wearable non-invasive epidermal glucose sensors: A review. Talanta. 2018;**177**:163-170

[47] Yu H, Rahim NAA. Imaging in Cellular and Tissue Engineering. CRC Press; 2013

[48] Bai Y, Zhang D, Li C, Liu C, Cheng J-X. "Bond-selective imaging of cells by mid-infrared Photothermal microscopy in high wavenumber region," The Journal of Physical Chemistry B, vol. 121, pp. 10249-10255, 2017/11/09 2017

[49] Fornaini C, Merigo E, Poli F, Cavatorta C, Rocca J-P, Selleri S, et al. Use of 1070 nm fiber lasers in oral surgery: Preliminary ex vivo study with FBG temperature monitoring. Laser Therapy. 2017;**26**:311-318

[50] Katta N, Mcelroy A, Estrada A, Milner TE. Optical coherence tomography (OCT) guided smart laser knife for cancer surgery (conference presentation). In: SPIE BiOS. 2017. p. 1

[51] Elahi P, Kalaycioğlu H, Akçaalan Ö, Şenel Ç, Ilday FÖ. Burst-mode thulium all-fiber laser delivering femtosecond pulses at a 1 GHz intra-burst repetition rate. Optics Letters. 2017;**42**:3808-3811

[52] Boen M, Wilson MJV, Goldman MP, Wu DC. Rejuvenation of the male scalp using 1,927 nm non-ablative fractional thulium fiber laser. Lasers in Surgery and Medicine. 2017;**49**:475-479

[53] Overton G, Nogee A, Belforte D, Holton C. Annual laser market review & forecast: Where have all the lasers gone? Laser Focus World. 2017;**53**:1-24

[54] Saleh BE, Teich MC, Saleh BE. Fundamentals of Photonics. Vol. 22. Wiley New York; 1991

[55] M.-B. E. Rare-earth doped optical fibers. In: Selected Topics on Optical Fiber Technology. Rijeka: InTech; 2012

[56] Wang W, Yuan J, Li L, Chen D, Qian Q, Zhang Q. Broadband 2.7 μm amplified spontaneous emission of Er 3+ doped tellurite fibers for mid-infrared laser applications. Optical Materials Express. 2015;**5**:2964-2977

[57] Henderson-Sapir O, Jackson SD, Ottaway DJ. Versatile and widely tunable mid-infrared erbium doped ZBLAN fiber laser. Optics Letters. 2016;**41**:1676-1679

[58] Zhu W, Qian L, Helmy AS. Implementation of three functional devices using erbium-doped fibers: An advanced photonics lab. Laser. 2007;**1520**:1570

[59] FM. Fiber Lasers at the Cutting Edge of Survey. Photonıcs Spectra; 2013

[60] Becker PC, Olsson NA, Simpson JR. Erbium-Doped Fiber Amplifiers: Fundamentals and Technology. Academic Press; 1999

[61] Giles CR, Desurvire E. Modeling erbium-doped fiber amplifiers. Journal of Lightwave Technology. 1991;**9**:271-283

[62] Balaraman B, Ravanfar-Jordan P, Friedman PM. Novel use of non-ablative fractional photothermolysis for café-au-lait macules in darker skin types. Lasers in Surgery and Medicine. 2017;**49**:84-87

[63] Wat H, Wu DC, Chan HHL. Fractional resurfacing in the Asian patient: Current state of the art. Lasers in Surgery and Medicine. 2017;**49**:45-59

[64] KINCADE K. Optoelectronics applications: Biophotonics fiber lasers find new opportunities in medical applications. Laser Focus World. 2005;**41**(9):76-80

[65] Morin F, Druon F, Hanna M, Georges P. Microjoule femtosecond fiber laser at 1.6 μm for corneal surgery applications. Optics Letters. 2009;**34**:1991-1993, 2009/07/01

[66] Friedmann DP, Tzu JE, Kauvar ANB, Goldman MP. Treatment of facial photodamage and rhytides using a novel 1,565 nm non-ablative fractional erbium-doped fiber laser. Lasers in Surgery and Medicine. 2016;**48**:174-180

[67] Aydin YO, Fortin V, Maes F, Jobin F, Jackson SD, Vallée R, et al. High efficiency cascade fiber laser at 2.8 μm. In: Lasers and Electro-Optics Europe & European Quantum Electronics Conference (CLEO/Europe-EQEC, 2017 Conference on). 2017. pp. 1-1

[68] Jelínková H. Lasers for Medical Applications: Diagnostics, Therapy and Surgery. Elsevier; 2013

[69] Moulton PF, Rines GA, Slobodtchikov EV, Wall KF, Frith G, Samson B, et al. Tm-doped fiber lasers: Fundamentals and power scaling. IEEE Journal of Selected Topics in Quantum Electronics. 2009;**15**:85-92

[70] Fortin V, Bernier M, Caron N, Faucher D, El-Amraoui M, Messaddeq Y, et al. Towards the development of fiber lasers for the 2 to 4 μm spectral region. Optical Engineering. 2013;**52**:054202

[71] Xu J, Tang Y, Yang Y, Hang Y. High power tunable tm 3+–fiber lasers and its application in pumping Cr 2+: ZnSe lasers. In: Lasers and Electro-Optics, 2008 and 2008 Conference on Quantum Electronics and Laser Science. CLEO/QELS 2008. Conference on. 2008. pp. 1-2

[72] Lee Y-W, Chien H-W, Cho C-H, Chen J-Z, Chang J-S, Jiang S. Heavily Tm3+–doped silicate fiber for high-gain fiber amplifiers. Fibers. 2013;**1**:82-92

[73] Cankaya H, Gorgulu A, Kurt A, Speghini A, Bettinelli M, Sennaroglu A. Comparative spectroscopic investigation of Tm3+:Tellurite glasses for 2-μm lasing applications. Applied Sciences. 2018;**8**:333

[74] Pal A, Pal D, Chowdhury SD, Sen R. All-fiber laser at 1.94 μm: Effect on soft tissue. In: SPIE BiOS. 2017. p. 4

[75] Jackson SD, King TA, Pollnau M. Diode-pumped 1.7-W erbium 3-μm fiber laser. Optics Letters. 1999;**24**:1133-1135

[76] Hu T. Ultrafast Mid-Infrared Fibre Lasers; 2015

[77] Antipov S, Jackson SD, Withford MJ, Fürbach A. A passively mode-locked sub-picosecond Ho3+,Pr3+–doped fluoride fiber laser operating at 2.86 μm(conference presentation). In: SPIE LASE. 2017. p. 1

[78] Haddad M, Emiliani E, Rouchausse Y, Coste F, Berthe L, Doizi S, et al. Impact of laser fiber tip cleavage on power output for ureteroscopy and stone treatment. World Journal of Urology. 2017;**35**:1765-1770

[79] Filatova S, Skobeltsin A, Shcherbakov I, Tsvetkov V. Study of contact method of 2-mm laser radiation impact on biological tissues. In: Lasers and Electro-Optics Europe & European Quantum Electronics Conference (CLEO/Europe-EQEC, 2017 Conference on). 2017. pp. 1-1

[80] Richardson DJ, Nilsson J, Clarkson WA. High power fiber lasers: Current status and future perspectives [invited]. Journal of the Optical Society of America B. 2010;**27**:B63-B92, 2010/11/01

[81] Ponsoda MI, Joan J. Analysis of photodarkening effects in ytterbium-doped laser fibers; 2013

[82] R Photonics. Ytterbium-doped gain media. ed; 2015

[83] Fornaini C, Poli F, Merigo E, Selleri S, Cavatorta C, Cucinotta A. 1070 nm Fiber laser and soft tissues oral surgery: Ex vivo study with FBG temperature recording. In: Lasers and Electro-Optics Europe & European Quantum Electronics Conference (CLEO/Europe-EQEC, 2017 Conference on). 2017. pp. 1-1

[84] Suzuki M, Ganeev RA, Yoneya S, Kuroda H. Generation of broadband noise-like pulse from Yb-doped fiber laser ring cavity. Optics Letters. 2015;**40**:804-807, 2015/03/01

[85] Kerse C, Yavaş S, Kalaycıoğlu H, Aşık MD, Akçaalan Ö, Ilday FÖ. High-speed, thermal damage-free ablation of brain tissue with femtosecond pulse bursts. In: 2015 Conference on Lasers and Electro-Optics Pacific Rim, Busan. 2015. p. 25H3_3

[86] He J, Lin D, Xu L, Beresna M, Zervas MN, Alam S-u, et al. 5.6 kW peak power, nanosecond pulses at 274 nm from a frequency quadrupled Yb-doped fiber MOPA. Optics Express. 2018;**26**:6554-6559, 2018/03/19

[87] Aytac-Kipergil E, Demirkiran A, Uluc N, Yavas S, Kayikcioglu T, Salman S, et al. Development of a fiber laser with independently adjustable properties for optical resolution photoacoustic microscopy. Scientific Reports. 2016;**6**:38674

[88] Lee Y-J, Ahn J-T, Jeong E-J, Song H-W, Ahn C-G, Noh HW, et al. MOPA fiber laser for photoacoustic imaging using arrayed ultrasound transducer. In: 25th International Conference on Optical Fiber Sensors. 2017. p. 4

[89] Liu X, Laegsgaard J, Iegorov R, Svane AS, Ilday FÖ, Tu H, et al. Nonlinearity-tailored fiber laser technology for low-noise, ultra-wideband tunable femtosecond light generation. Photonics Research. 2017;**5**:750-761, 2017/12/01

[90] Shafirstein G, Bellnier D, Oakley E, Hamilton S, Potasek M, Beeson K, et al. Interstitial photodynamic therapy—A focused review. Cancer. 2017;**9**(12)

[91] Kim M, Jung HY, Park HJ. Topical PDT in the treatment of benign skin diseases: Principles and new applications. International Journal of Molecular Sciences. 2015;**16**:23259-23278

[92] Moghissi K, Dixon K, Gibbins S. A surgical view of photodynamic therapy in oncology: A review. The Surgery Journal. 2015;**1**:e1

[93] van Straten D, Mashayekhi V, de Bruijn HS, Oliveira S, Robinson DJ. Oncologic photodynamic therapy: Basic principles, current clinical status and future directions. Cancer. 2017;**9**:19

[94] Friedmann DP, Tzu JE, Kauvar AN, Goldman MP. Treatment of facial photodamage and rhytides using a novel 1,565 nm non-ablative fractional erbium-doped fiber laser. Lasers in Surgery and Medicine. 2016;**48**:174-180

[95] Keiser G. Fundamentals of light SourcesLight sources. In: Biophotonics. Springer; 2016. pp. 91-118

[96] Boucher D. PDT light sources and PDT devices: The necessary tools for performing good photodynamic therapy treatments. Photodiagnosis and Photodynamic Therapy. 2017;**17**:A5

[97] Aird GA, Sitenga JL, Nguyen AH, Vaudreuil A, Huerter CJ. Light and laser treatment modalities for disseminated superficial actinic porokeratosis: A systematic review. Lasers in Medical Science. 2017;**32**:945-952

[98] Samadarsinee S. Multisensor Noninvasive Blood Glucose Monitoring System. Wichita State University; 2015

[99] Haas J, Mizaikoff B. Advances in mid-infrared spectroscopy for chemical analysis. Annual Review of Analytical Chemistry. 2016;**9**:45-68

[100] Wang L, Mizaikoff B. Application of multivariate data-analysis techniques to biomedical diagnostics based on mid-infrared spectroscopy. Analytical and Bioanalytical Chemistry. 2008;**391**:1641-1654

[101] Ikyo A, Marko I, Hild K, Adams A, Arafin S, Amann M-C, et al. Temperature stable mid-infrared GaInAsSb/GaSb vertical cavity surface emitting lasers (VCSELs). Scientific Reports. 2016;**6**:19595

[102] Kottmann J, Rey JM, Sigrist MW. Mid-infrared photoacoustic detection of glucose in human skin: Towards non-invasive diagnostics. Sensors. 2016;**16**:1663

[103] Yu Y, Gai X, Wang T, Ma P, Wang R, Yang Z, et al. Mid-infrared supercontinuum generation in chalcogenides. Optical Materials Express. 2013;**3**:1075-1086

[104] Liakat S, Bors KA, Xu L, Woods CM, Doyle J, Gmachl CF. Noninvasive in vivo glucose sensing on human subjects using mid-infrared light. Biomedical Optics Express. 2014;**5**:2397-2404, 2014/07/01

[105] Kerse C, Yavaş S, Kalaycıoğlu H, Aşık MD, Akçaalan Ö, Ilday FÖ. High-speed, thermal damage-free ablation of brain tissue with femtosecond pulse bursts. In: Conference on Lasers and Electro-Optics/Pacific Rim. 2015. p. 25H3_3

[106] Kerse C, Kalaycıoğlu H, Elahi P, Akçaalan Ö, Ilday FÖ. 3.5-GHz intra-burst repetition rate ultrafast Yb-doped fiber laser. Optics Communications. 2016;**366**:404-409

Chapter 6

Quantum Noise in Optical Amplifiers

Kyo Inoue

Additional information is available at the end of the chapter

http://dx.doi.org/10.5772/intechopen.72992

Abstract

Noise is one of the basic characteristics of optical amplifiers. Whereas there are various noise sources, the intrinsic one is quantum noise that originates from Heisenberg's uncertainty principle. This chapter describes quantum noise in optical amplifiers, including population-inversion–based amplifiers such as an Erbium-doped fiber amplifier and a semiconductor optical amplifier, and optical parametric amplifiers. A full quantum mechanical treatment is developed based on Heisenberg equation of motion for quantum mechanical operators. The results provide the quantum mechanical basis for a classical picture of amplifier noise widely used in the optical communication field.

Keywords: quantum noise, noise figure, quantum mechanics, population-inversion–based amplifier, optical parametric amplifier

1. Introduction

Noise is one of the important properties in optical amplifiers [1]. The intrinsic noise characteristic is determined by quantum mechanics, especially Heisenberg's uncertainty principle. This chapter describes quantum noise in optical amplifiers in terms of quantum mechanics. After brief introduction of a classical treatment usually used in the optical communication field, properties of an optically amplified light, such as the mean amplitude, the mean photon number, and their variances, are derived based on first principles of quantum mechanics. Two kinds of optical amplifiers are treated: amplifiers based on two-level interaction in a population-inverted medium, i.e., an Erbium-doped fiber amplifier and a semiconductor optical amplifier, and those based on parametric interaction in an optical nonlinear medium. The results presented here provide the quantum mechanical basis to a phenomenological classical treatment conventionally employed for describing amplifier noise.

2. Classical treatment

A classical treatment of amplifier noise is widely employed in the optical communication field [1, 2], whereas it originates from quantum mechanics. Before presenting a quantum mechanical treatment, we briefly introduce the classical treatment. We first consider the light intensity or the photon number outputted from an amplifier. A photon-number rate equation for light propagating through a population-inverted medium can be expressed as

$$\frac{dn}{dz} = gN_2 n - gN_1 n + gN_2, \tag{1}$$

where n is the number of photons, N_2 and N_1 are the numbers of atoms at the higher and lower energy states in the medium, respectively, and g is a constant representing the photon emission/absorption efficiency. The first, second, and third terms represent stimulated emission, absorption, and spontaneous emission, respectively. The efficiency g is common in this phenomenon in a simple two-level model [3]. Assuming that N_1 and N_2 are uniform along the medium length, the photon number at the output is calculated from Eq. (1) as

$$n_{\mathrm{out}} = n_{\mathrm{in}} e^{g(N_2 - N_1)L} + \frac{N_2}{N_2 - N_1} \left\{ e^{g(N_2 - N_1)L} - 1 \right\}, \tag{2}$$

where L is the medium length. The first term represents amplified signal photons with a signal gain of $\exp[g(N_2 - N_1)L] \equiv G$. The second term represents amplified spontaneous emission (ASE) photons, which can be rewritten as $n_{\mathrm{sp}}(G - 1)$ with $n_{\mathrm{sp}} \equiv N_2/(N_2 - N_1)$. The parameter n_{sp} is called "population inversion parameter" or "noise factor." Note that the above equations are for the photon number in one mode in terms of the frequency and the polarization.

Eq. (2) shows that the output photon number is composed of amplified signal photons and ASE photons. Accordingly, the output amplitude is supposed to be a summation of amplitudes of amplified signal and ASE lights as

$$E_{\mathrm{out}} = \sqrt{G} E_{\mathrm{in}} + E_{\mathrm{ASE}}, \tag{3}$$

where E_{out}, E_{in}, and E_{ASE} are the amplitudes of the output light, the input signal light, and ASE light, respectively. The second term provides the ASE power as $\langle |E_{\mathrm{ASE}}|^2 \rangle = n_{\mathrm{sp}}(G - 1)hf\Delta f$, where $\langle\ \rangle$ denotes the mean value, hf is one photon energy, and Δf is the ASE bandwidth. Regarding the ASE phase, it is supposed to be completely random because spontaneous emission occurs randomly. Thus, the average of the ASE amplitude is supposed to be zero: $\langle E_{\mathrm{ASE}} \rangle = 0$. Here, we decompose E_{ASE} into the real and imaginary parts, which are supposed to be isotropic because the phase is random: $\langle \{\mathrm{Re}[E_{\mathrm{ASE}}]\}^2 \rangle = \langle \{\mathrm{Im}[E_{\mathrm{ASE}}]\}^2 \rangle = \langle |E_{\mathrm{ASE}}|^2 \rangle/2 = n_{\mathrm{sp}}(G - 1)hf\Delta f/2$. Subsequently, the variance of each amplitude component is $\langle \{\mathrm{Re}[E_{\mathrm{ASE}}]\}^2 \rangle - \langle \mathrm{Re}[E_{\mathrm{ASE}}] \rangle^2 = \langle \{\mathrm{Im}[E_{\mathrm{ASE}}]\}^2 \rangle - \langle \mathrm{Im}[E_{\mathrm{ASE}}] \rangle^2 = n_{\mathrm{sp}}(G - 1)hf\Delta f/2$.

Intensity noise is evaluated using Eq. (3). The output intensity is given by $I_{\mathrm{out}} = |E_{\mathrm{out}}|^2$, and its fluctuation is evaluated by the variance of I_{out} as

$$< I_{\text{out}}^2 > - < I_{\text{out}}>^2 =< |E_{\text{out}}|^4 > - < |E_{\text{out}}|^2>^2 = 2G|E_{\text{in}}|^2 < |E_{\text{ASE}}|^2 > + < |E_{\text{ASE}}|^4 > - < |E_{\text{ASE}}|^2>^2, \tag{4}$$

where the postulate of the ASE light phase being random is used in averaging. The first term represents 2 × <signal output intensity> × <ASE intensity>, which is called the "signal-spontaneous beat noise." The second and third terms represent the intensity variance of the ASE light, which is called the "spontaneous-spontaneous beat noise."

As an indicator for the amplifier noise performance, the "noise figure (NF)" is usually used. It is defined as the ratio of the signal-to-noise ratios (SNRs) at the input and output of an amplifier in terms of the optical intensity: NF $\equiv$ $(\text{SNR})_{\text{in}}/(\text{SNR})_{\text{out}}$ where SNR $\equiv$ (mean intensity)^2/(variance of the intensity) in the signal mode. The square of the mean intensity at the output is calculated from Eq. (3) as $<|E_{\text{out}}|^2> = G|E_{\text{in}}|^2 + <|E_{\text{ASE}}|^2>$, and the output variance is expressed as Eq. (4); thus the output SNR is expressed as

$$(\text{SNR})_{\text{out}} = \frac{G^2|E_{\text{in}}|^2 + 2G|E_{\text{in}}|^2 < |E_{\text{ASE}}|^2 > + < |E_{\text{ASE}}|^2>^2}{2G|E_{\text{in}}|^2 < |E_{\text{ASE}}|^2 > + < |E_{\text{ASE}}|^4 > - < |E_{\text{ASE}}|^2>^2}. \tag{5}$$

On the other hand, the input SNR is evaluated for pure monochromatic light in the definition of the noise figure. In quantum mechanics, such a light is called "coherent state," whose photon-number variance is equal to the mean photon number: $<n^2> - <n>^2 = <n>$. Thus, $<|E_{\text{in}}|^4> - <|E_{\text{in}}|^2>^2 = |E_{\text{in}}|^2 hf$ where hf is attached for the dimension to be matched. Subsequently, the input SNR is given by $<|E_{\text{in}}|^2>^2/(<|E_{\text{in}}|^4> - <|E_{\text{in}}|^2>^2) = |E_{\text{in}}|^2/hf$. Therefore, the NF is expressed as

$$\text{NF} = \frac{(\text{SNR})_{\text{in}}}{(\text{SNR})_{\text{out}}} \approx \frac{|E_{\text{in}}|^2}{hf} \cdot \frac{2G|E_{\text{in}}|^2 < |E_{\text{ASE}}|^2 >}{G^2|E_{\text{in}}|^4} = 2n_{\text{sp}}\frac{G-1}{G}, \tag{6}$$

where $G|E_{\text{in}}|^2 >> |E_{\text{ASE}}|^2$ is assumed, and $<|E_{\text{ASE}}|^2> = n_{\text{sp}}(G-1)hf$ is substituted because the signal mode is considered here.

The above-mentioned classical treatment is widely used for noise in optical amplifiers. However, it is based on phenomenological assumptions. (i) Eq. (3) is phenomenologically provided. Though the solution of the photon-number rate equation indicates that the output photon number is composed of amplified signal photons and ASE photons (Eq. (2)), this result does not logically conclude that the output amplitude is a linear summation of the amplified signal and the ASE amplitudes as Eq. (3). (ii) The phase of ASE light is assumed to be random, which is a phenomenological postulate, not logically derived from first principles. Although the above classical treatment is correct and useful in fact, we need quantum mechanics for theoretically confirming its validity, which is presented in the following sections.

3. Quantum mechanics

In this section, we briefly review quantum mechanics, especially the Heisenberg picture [4]. The basic concept of quantum mechanics is that a physical state is probabilistic and the theory only provides mean values of physical quantities, which is given by a quantum mechanical inner product of a physical quantity operator $\widehat{x}$ with respect to an objective state $|\Psi>$ as $<\Psi|\widehat{x}|\Psi>$. In the Heisenberg picture, an operator evolves according to the Heisenberg equation of motion as

$$\frac{d\widehat{x}}{dt}=\frac{1}{i\hbar}\left[\widehat{x},\widehat{H}\right], \tag{7}$$

where $\widehat{H}$ is the Hamiltonian (i.e., the energy operator) of a concerned system, $[\widehat{x},\widehat{y}]=\widehat{x}\widehat{y}-\widehat{y}\widehat{x}$ denotes a commutator, and $\hbar$ is Planck's constant. The mean value after the evolution is given by the inner product $<\Psi_0|\widehat{x}(t)|\Psi_0>$ where $|\Psi_0>$ is an initial state.

The most important operator in discussing quantum mechanical properties of light is the "annihilation operator," $\widehat{a}$, which corresponds to the complex amplitude of light and is also called as the "field operator." It has an eigenstate $|\alpha>$ and an eigenvalue α:$\widehat{a}|\alpha>=\alpha|\alpha>$. This eigenstate $|\alpha>$ is called "coherent state" and corresponds to pure monochromatic light in classical optics, and the eigenvalue α corresponds to its complex amplitude in the photon-number unit. The Hermitian conjugate of the annihilation operator $\widehat{a}^{\dagger}$ is called the "creation operator," which satisfies $<\alpha|\widehat{a}^{\dagger}=\alpha^{*}<\alpha|$. The annihilation and creation operators have a commutation relationship $\left[\widehat{a},\widehat{a}^{\dagger}\right]=1$, which comes from Heisenberg's uncertainty principle and is the origin of quantum noise. They also work to annihilate or create a photon as $\widehat{a}|n>=\sqrt{n}|n-1>$ and $\widehat{a}^{\dagger}|n>=\sqrt{n+1}|n+1>$, where $|n>$ is a photon number state having n photons. Another important operator is the photon-number operator defined as $\widehat{n}\equiv\widehat{a}^{\dagger}\widehat{a}$. Using the above eigenvalue/eigenstate equations, the mean photon number of a coherent state is given by $<\alpha|\widehat{n}|\alpha>=<\alpha|\widehat{a}^{\dagger}\widehat{a}|\alpha>=\alpha^{*}\alpha<\alpha|\alpha>=|\alpha|^{2}$, which corresponds to the classical picture that the absolute square of a complex amplitude represents the light intensity.

We discuss quantum noise of optical amplifiers in the following sections, using the above-mentioned framework of quantum mechanics. Note that the above operator $\widehat{a}$ is for one mode in terms of the frequency and the polarization state. Thus, the following discussions are for one optical mode.

4. Population-inversion–based amplifiers

Erbium-doped fiber amplifiers (EDFAs) are widely used in optical communications. Optical semiconductor amplifiers are also being developed for compact and integrated amplifying devices. They amplify signal light through interaction between light and a two-level atomic system with population inversion. This section discusses quantum noise in population-inversion-based amplifiers [5].

4.1. Heisenberg equation

The Hamiltonian for a light-atom interacting system can be expressed as [4]

$$\hat{H} = \hbar\omega\hat{a}^{\dagger}\hat{a} + \sum_j \hbar\omega_{\mathrm{a}}^{(j)}\hat{\pi}_j^{\dagger}\hat{\pi}_j + i\hbar\sum_j \kappa_j\left(\hat{\pi}_j^{\dagger}\hat{a} - \hat{\pi}_j\hat{a}^{\dagger}\right). \tag{8}$$

The first and second terms are the Hamiltonians of light and atoms without interaction, respectively, where $\hat{a}$ is the field operator; ω is the angular frequency of light; $\hat{\pi}_j^{\dagger} = |2><1|_j$ and $\hat{\pi}_j = |1><2|_j$ are the transition operators of an atom, with $|2>_j$ and $|1>_j$ denoting the upper and lower energy states, respectively, satisfying $<1|1>_{j,k} = <2|2>_{j,k} = \delta_{j,k}$ and $<1|2>_{j,k} = <2|1>_{j,k} = 0$; $\hbar\omega_{\mathrm{a}}^{(j)}$ is the energy difference between the upper and lower states; the subscript j indicates a specific atom. The third term is the interaction Hamiltonian between light and atoms, which represents energy exchange such that a photon is created while an atom transits from the upper to the lower states and vice versa, with κ_j being the coupling coefficient.

Applying the above Hamiltonian to the Heisenberg equations for $\hat{a}$ and $\hat{\pi}_j$, we obtain the following differential equations:

$$\frac{d\hat{a}}{dt} = \frac{1}{i\hbar}\left[\hat{a}, \hat{H}\right] = -i\omega\hat{a} - \sum_j \kappa_j\hat{\pi}_j, \tag{9a}$$

$$\frac{d\hat{\pi}_j}{dt} = \frac{1}{i\hbar}\left[\hat{\pi}_j, \hat{H}\right] = -i\omega_{\mathrm{a}}^{(j)}\hat{\pi}_j + \kappa_j\hat{a}\left(\hat{\pi}_j\hat{\pi}_j^{\dagger} - \hat{\pi}_j^{\dagger}\hat{\pi}_j\right). \tag{9b}$$

Employing the variable translations $\hat{a} \to \hat{a}\exp(-i\omega t)$ and $\hat{\pi}_j \to \hat{\pi}_j\exp\left(-i\omega_{\mathrm{a}}^{(j)}t\right)$, these equations are rewritten as

$$\frac{d\hat{a}}{dt} = -\sum_j \kappa_j\hat{\pi}_j e^{i\Delta\omega_j t}, \tag{10a}$$

$$\frac{d\hat{\pi}_j}{dt} = \kappa_j\hat{a}\left(\hat{\pi}_j\hat{\pi}_j^{\dagger} - \hat{\pi}_j^{\dagger}\hat{\pi}_j\right)e^{-i\Delta\omega_j t}, \tag{10b}$$

where $\Delta\omega_j \equiv \omega - {\omega_{\mathrm{a}}}^{(j)}$, i.e., the frequency detuning between light and a two-level system.

We solve Eq. (10) by an iterative approximation. First, the first-order solutions are derived by substituting the initial values $\{\hat{a}^{(0)}, \hat{\pi}_j^{(0)}\}$ into the right-hand side of the equations:

$$\frac{d\hat{a}^{(1)}}{dt} = -\sum_j \kappa_j\hat{\pi}_j^{(0)} e^{i\Delta\omega_j t}, \tag{11a}$$

$$\frac{d\hat{\pi}_j^{(1)}}{dt} = \kappa_j\hat{a}^{(0)}\left(\hat{\pi}_j^{(0)}\hat{\pi}_j^{(0)\dagger} - \hat{\pi}_j^{(0)\dagger}\hat{\pi}_j^{(0)}\right)e^{-i\Delta\omega_j t}. \tag{11b}$$

The solutions of these equations are

$$\hat{a}^{(1)} = \hat{a}^{(0)} + i\sum_j \kappa_j\hat{\pi}_j^{(0)}\frac{e^{i\Delta\omega_j t} - 1}{\Delta\omega_j}, \tag{12a}$$

$$\widehat{\pi}_j^{(1)} = \widehat{\pi}_j^{(0)} + i\kappa_j \widehat{a}^{(0)} \left(\widehat{\pi}_j^{(0)}\widehat{\pi}_j^{(0)\dagger} - \widehat{\pi}_j^{(0)\dagger}\widehat{\pi}_j^{(0)}\right)\frac{e^{-i\Delta\omega_j t}-1}{\Delta\omega_j}. \tag{12b}$$

Next, these first-order solutions are substituted into the right-hand side of Eq. (10a), and the second-order solution is calculated as

$$\widehat{a}^{(2)} = \widehat{a}^{(0)}\left\{1 - \sum_j \kappa_j^2\left(\widehat{\pi}_j^{(0)}\widehat{\pi}_j^{(0)\dagger} - \widehat{\pi}_j^{(0)\dagger}\widehat{\pi}_j^{(0)}\right)\frac{1 - e^{i\Delta\omega_j t} + i\Delta\omega_j t}{\left(\Delta\omega_j\right)^2}\right\} + i\sum_j \kappa_j \widehat{\pi}_j^{(0)}\frac{e^{i\Delta\omega_j t}-1}{\Delta\omega_j}. \tag{13}$$

We regard Eq. (13) as the time evolution of the field operator during a short time τ, and rewrite it as

$$\widehat{a}(t_0+\tau) = \widehat{a}(t_0)\left\{1 - \widehat{\Pi}(t_0)\right\} + \widehat{\mathrm{P}}(t_0), \tag{14}$$

where

$$\widehat{\Pi}(t_0) = \sum_j \kappa_j^2\left\{\widehat{\pi}_j(t_0)\widehat{\pi}_j^{\dagger}(t_0) - \widehat{\pi}_j^{\dagger}(t_0)\widehat{\pi}_j(t_0)\right\}\frac{2\sin^2\left(\Delta\omega_j\tau/2\right) + i\left\{\Delta\omega_j\tau - \sin\left(\Delta\omega_j\tau\right)\right\}}{\left(\Delta\omega_j\right)^2}, \tag{15a}$$

$$\widehat{\mathrm{P}}(t_0) = i\sum_j \kappa_j\widehat{\pi}_j(t_0)\frac{e^{i\Delta\omega_j\tau}-1}{\Delta\omega_j}. \tag{15b}$$

Eq. (14) is the basic expression for discussing quantum properties of light that travels through an amplifier. For the discussion, we also need an initial state of the system at t_0. It can be expressed as

$$|\Psi_0\rangle = |\Psi(t_0)\rangle \otimes |\Psi_\mathrm{a}(t_0)\rangle = |\Psi(t_0)\rangle \otimes \left\{\bigotimes_j \left(c_1|1\rangle + c_2|2\rangle\right)_j\right\}, \tag{16}$$

where $|\Psi(t_0)\rangle$ denotes the initial state of light, $|\Psi_\mathrm{a}(t_0)\rangle$ denotes that of atoms, and c_1 and c_2 are the probability amplitudes of an atom being in the lower and upper states, respectively, satisfying $|c_1|^2 + |c_2|^2 = 1$. We use Eqs. (14) and (16) in the following calculations.

4.2. Mean amplitude

We first discuss the mean amplitude. The mean amplitude, denoted as $\bar{a}$ hereafter, after a short-time interaction is expressed from Eq. (14) as

$$\begin{aligned}\bar{a}(t_0+\tau) &= \langle \Psi_0|\widehat{a}\,(t_0+\tau)|\Psi_0\rangle = \langle \Psi(t_0)|\widehat{a}(t_0+\tau)|\Psi(t_0)\rangle \\ &\quad \times\left\{1 - \langle \Psi_\mathrm{a}(t_0)|\widehat{\Pi}(t_0)|\Psi_\mathrm{a}(t_0)\rangle\right\} + \langle \Psi_\mathrm{a}(t_0)|\widehat{\mathrm{P}}(t_0)|\Psi_\mathrm{a}(t_0)\rangle\,.\end{aligned} \tag{17}$$

The average of the transition operator $\widehat{\Pi}$ is calculated, using Eqs. (15a) and (16), as

$$< \Psi_a(t_0)|\widehat{\Pi}(t_0)|\Psi_a(t_0) >= \sum_j \kappa_j^2\left(|c_1|^2 - |c_2|^2\right)_j \frac{2\sin^2(\Delta\omega_j\tau/2) + i\{\Delta\omega_j\tau - \sin(\Delta\omega_j\tau)\}}{(\Delta\omega_j)^2}. \quad (18)$$

Assuming that the energy levels of each atom are densely distributed, the summation in this equation can be replaced by an integral in the frequency domain, and the real part of Eq. (18) is further calculated as

$$\begin{aligned}\sum_j \kappa_j^2\left(|c_1|^2 - |c_2|^2\right)_j \frac{2\sin^2(\Delta\omega_j\tau/2)}{(\Delta\omega_j)^2} &= \int_{-\infty}^{\infty} \kappa^2\left(|c_1|^2 - |c_2|^2\right)_\Omega \frac{2\sin^2(\Omega\tau/2)}{\Omega^2}\rho(\Omega)d\Omega \\ = 2\kappa^2\left(|c_1|^2 - |c_2|^2\right)\int_{-\infty}^{\infty} \frac{\sin^2(\Omega\tau/2)}{\Omega^2}\rho(\Omega)d\Omega &= \kappa^2(N_1 - N_2)\pi\tau,\end{aligned} \quad (19)$$

where Ω is the frequency detuning; ρ is the density of atoms in the frequency domain and is assumed to be constant around a resonant frequency $\Omega = 0$ as ρ_0; $\{\kappa, |c_2|^2$, and $|c_1|^2\}$ are assumed to be identical for any atom; and $N_1 \equiv \rho_0|c_1|^2$ and $N_2 \equiv \rho_0|c_2|^2$ are the numbers of atoms at the lower and upper energy states, respectively. On the other hand, the imaginary part of Eq. (18) can be rewritten as

$$\sum_j \kappa_j^2\left(|c_1|^2 - |c_2|^2\right)_j \frac{\Delta\omega_j\tau - \sin(\Delta\omega_j\tau)}{(\Delta\omega_j)^2} = \int_{-\infty}^{\infty} \kappa^2\left(|c_1|^2 - |c_2|^2\right)_\Omega \frac{\Omega\tau - \sin(\Omega\tau)}{\Omega^2}\rho(\Omega)d\Omega. \quad (20)$$

In this expression, the contents of the integral is an odd function around the resonant frequency $\Omega = 0$. Thus, the imaginary part equals 0. Regarding the average of $\widehat{\mathrm{P}}$ in Eq. (17), it is calculated as $< \Psi_a(t_0)\left|\widehat{\mathrm{P}}\right|\Psi_a(t_0) >= i\sum_j \kappa_j\left(c_1^* c_2\right)_j\{\exp(i\Delta\omega_j\tau) - 1\}/\Delta\omega_j$. Here, the phases of the probability amplitudes are random in general, and $(c_1{}^*c_2)_j = 0$ on average. Subsequently, $< \Psi_a(t_0)\left|\widehat{\mathrm{P}}\right|\Psi_a(t_0) >= 0$. Substituting the averages evaluated as above, Eq. (17) can be rewritten as

$$\bar{a}(t_0 + \tau) = \bar{a}(t_0)\{1 + \kappa^2(N_2 - N_1)\pi\tau\}. \quad (21)$$

Eq. (21) describes the time evolution of the mean amplitude of light traveling through an amplifying medium, i.e., the time evolution in a frame moving along with the light, during a short time. This expression can be translated to the spatial evolution along the medium length as

$$\bar{a}(z_0 + \Delta z) = \bar{a}(z_0)\{1 + (g/2)(N_2 - N_1)\Delta z\}, \quad (22)$$

where $g \equiv 2\kappa^2\pi/v$ with v being the light velocity. Applying a Taylor expansion $x(z_0 + \Delta z) = x(z_0) + [dx/dz](z_0) \times \Delta z$ to this equation, we obtain the following differential equation:

$$\frac{d\bar{a}}{dz} = \frac{g}{2}(N_2 - N_1)\bar{a}. \quad (23)$$

Eq. (23) includes $(N_2 - N_1)$, which depends on the atoms' state at a local position. Here, we assume that the atoms' state is uniform along the medium length independent of z, and this condition is satisfied in uniformly pumped amplifiers with no gain saturation. With this assumption, Eq. (23) can be analytically solved, and the mean amplitude at the amplifier output is expressed as

$$\overline{a}_{\text{out}} = \sqrt{G}\overline{a}_{\text{in}}, \tag{24}$$

where $G \equiv \exp[g(N_2 - N_1)L]$ with L being the amplifier length. This result, derived from the Heisenberg equation, is equivalent to the classical expression, i.e., Eq. (3) with $<E_{\text{ASE}}> = 0$, and confirms that the mean amplitude of ASE light is zero.

4.3. Mean photon number

We next discuss the mean photon number. The short-time evolution of the photon-number operator is expressed from Eq. (14) as

$$\widehat{n}(t_0+\tau) = \left[\widehat{a}^{\dagger}(t_0)\left\{1-\widehat{\Pi}^{\dagger}(t_0)\right\} + \widehat{\mathrm{P}}^{\dagger}(t_0)\right]\left[\widehat{a}(t_0)\left\{1-\widehat{\Pi}(t_0)\right\} + \widehat{\mathrm{P}}(t_0)\right], \tag{25}$$

from which the short-time evolution of the mean photon number is obtained as

$$\overline{n}(t_0+\tau) =< \Psi_0|\widehat{n}(t_0+\tau)|\Psi_0 >= \overline{n}(t_0)\left\{1+2\kappa^2(N_2-N_1)\pi\tau\right\} + 2\kappa^2 N_2\pi\tau. \tag{26}$$

In deriving Eq. (26), higher-order interaction terms are neglected, because the short-time evolution is considered here. This short-time evolution is translated to the short-length evolution along the medium length as

$$\overline{n}(z_0+\Delta z) = \overline{n}(z_0)\{1+g(N_2-N_1)\Delta z\} + gN_2\Delta z, \tag{27}$$

from which the following spatial differential equation is obtained:

$$\frac{d\overline{n}}{dz} = g(N_2-N_1)\overline{n} + gN_2. \tag{28}$$

This equation is equivalent to the photon-number rate equation given in Eq. (1). Therefore, similar to Eq. (1), the output of the mean photon number is calculated as

$$\overline{n}(L) = G\overline{n}(0) + n_{\text{sp}}(G-1). \tag{29}$$

The first and second terms represent amplified signal photons and ASE photons, respectively. It is noted that ASE photons appear at the output even though there is no such light in the mean amplitude as shown in Eq. (24).

4.4. Amplitude fluctuation

We next discuss amplitude fluctuations or noise. The light amplitude has two quadratures, i.e., the real and imaginary components. The operators representing each component are

$\widehat{x}_1 = \left(\widehat{a} + \widehat{a}^\dagger\right)/2$ and $\widehat{x}_2 = \left(\widehat{a} - \widehat{a}^\dagger\right)/2i$, respectively, and their fluctuations are evaluated by $\sigma_{1,2}^2 =< \Psi_0|\widehat{x}_{1,2}^2|\Psi_0 > - < \Psi_0|\widehat{x}_{1,2}|\Psi_0>^2$.

From Eq. (14), the short-time evolution of the mean square of the real component is expressed as

$$\begin{aligned} < \Psi_0|\widehat{x}_1^2(t_0+\tau)|\Psi_0 > &= \frac{1}{4} < \Psi_0|\left\{\widehat{a}(t_0+\tau) + \widehat{a}^\dagger(t_0+\tau)\right\}^2|\Psi_0 > \\ &= < \Psi|\widehat{x}_1^2(t_0)|\Psi > \left\{1 + 2\kappa^2(N_2 - N_1)\pi\tau\right\} + \frac{1}{2}\kappa^2(N_2 + N_1)\pi\tau, \end{aligned} \tag{30}$$

where $O(\tau^2)$ terms are neglected. On the other hand, the square of the average of the real component is expressed as

$$\begin{aligned} < \Psi_0|\widehat{x}_1(t_0+\tau)|\Psi_0>^2 &= \frac{1}{4} < \Psi_0|\left\{\widehat{a}(t_0+\tau) + \widehat{a}^\dagger(t_0+\tau)\right\}|\Psi_0>^2 \\ &= \frac{1}{4}\Big[< \Psi|\widehat{a}(t_0)|\Psi > \left\{1 + \kappa^2(N_2 - N_1)\pi\tau\right\} + < \Psi|\widehat{a}^\dagger(t_0)|\Psi > \\ &\quad \left\{1 + \kappa^2(N_2 - N_1)\pi\tau\right\}\Big]^2 \approx < \Psi|\widehat{x}_1(t_0)|\Psi>^2\left\{1 + 2\kappa^2(N_2 - N_1)\pi\tau\right\}. \end{aligned} \tag{31}$$

From Eqs. (30) and (31), the short-time evolution of the variance of the real component is obtained as

$$\begin{aligned} \sigma_{x1}^2(t_0+\tau) &=< \Psi_0|\widehat{x}_1^2(t_0+\tau)|\Psi_0 > - < \Psi_0|\widehat{x}_1(t_0+\tau)|\Psi_0>^2 \\ &= \left\{< \Psi|\widehat{x}_1^2(t_0)|\Psi > - < \Psi|\widehat{x}_1(t_0)|\Psi>^2\right\}\left\{1 + 2\kappa^2(N_2 - N_1)\pi\tau\right\} \\ &\quad + \frac{1}{2}\kappa^2(N_2 + N_1)\pi\tau = \sigma_{x1}^2(t_0)\left\{1 + 2\kappa^2(N_2 - N_1)\pi\tau\right\} \\ &\quad + \frac{1}{2}\kappa^2(N_2 + N_1)\pi\tau. \end{aligned} \tag{32}$$

This equation is translated to the short-length evolution as

$$\sigma_{x1}^2(z_0 + \Delta z) = \sigma_{x1}^2(z_0)\{1 + g(N_2 - N_1)\Delta z\} + \frac{g}{4}(N_2 + N_1)\Delta z, \tag{33}$$

from which the following differential equation is obtained:

$$\frac{d\sigma_{x1}^2}{dz} = g(N_2 - N_1)\sigma_{x1}^2 + \frac{g}{4}(N_2 + N_1). \tag{34}$$

From Eq. (34), the variance of the real component at the output is calculated as

$$\sigma_{x1}^2(L) = G\sigma_{x1}^2(0) + \frac{1}{4}\left(2n_{\mathrm{sp}} - 1\right)(G - 1). \tag{35}$$

The variance of the imaginary component is similarly calculated as $\sigma_{x2}{}^2(L) = G\sigma_{x2}{}^2\ (0) + (1/4)(2n_{\mathrm{sp}} - 1)(G - 1)$. The first term in Eq. (35) represents amplified fluctuations from the incident light, with a gain G whose square root equals the amplitude gain [Eq. (24)], and the second term represents additional fluctuations that are superimposed onto the amplified fluctuation through the amplification process. This input and output relationship of amplitude fluctuations can be schematically illustrated in the complex amplitude space (constellation) as shown in **Figure 1**.

For a coherent incident state, i.e., whose amplitude variances is $\sigma_{x1}{}^2\ (0) = \sigma_{x2}{}^2\ (0) = 1/4$ [4], Eq. (35) is rewritten as

$$\sigma_{x1}^2(L) = \frac{1}{4}G + \frac{1}{4}\left(2n_{\mathrm{sp}} - 1\right)(G - 1) = \frac{1}{4} + \frac{1}{2}n_{\mathrm{sp}}(G - 1). \tag{36}$$

The first term 1/4 corresponds to the inherent quantum noise of a coherent state, and the second term represents amplitude fluctuations at the amplifier output in a classical picture. Recalling that the mean amplitude at the amplifier output is that amplified from the incident light with no addition mean field, as indicated in Eq. (24), Eq. (36) suggests that the amplifier output can be regarded as a summation of a clean signal light (i.e., coherent state), displaced from the initial mean amplitude position, and fluctuating light, whose mean value and variance are 0 and $n_{\mathrm{sp}}(G - 1)/2$, respectively, in one quadrature. **Figure 2** illustrates this output condition in the complex amplitude space. Noting that the variance of the fluctuating light equals half of the spontaneous photon number indicated in the second term in Eq. (28), we can say that the above picture illustrated in **Figure 2** is equivalent to the classical picture of amplitude noise described in Section 2, where the ASE power is given by $<|E_{\mathrm{ASE}}|^2> = n_{\mathrm{sp}}(G - 1)hf\Delta f$ and the variance of the real component of ASE light is given by $<\{\mathrm{Re}[E_{\mathrm{ASE}}]\}^2> - <\mathrm{Re}[E_{\mathrm{ASE}}]> = n_{\mathrm{sp}}(G - 1)hf\Delta f/2$. Therefore, the classical picture introduced in Section 2 is confirmed by the quantum mechanical treatment presented here, except for the inherent quantum noise of 1/4. This noise 1/4 is sometimes called "vacuum fluctuation" or "zero-point fluctuation," that appears owing to quantum mechanics.

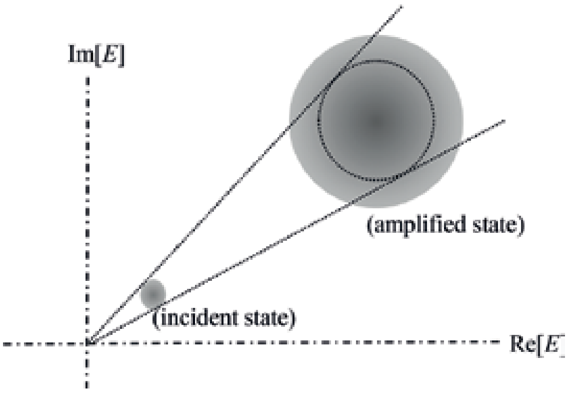

Figure 1. Constellation diagram of amplified light.

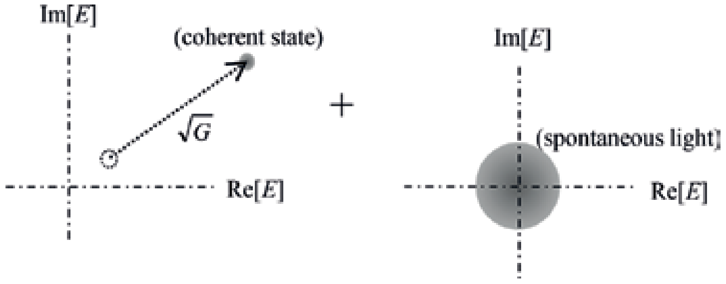

Figure 2. Decomposition of amplified light in the constellation diagram.

4.5. Photon-number fluctuation

We next discuss photon-number fluctuations. These fluctuations are evaluated employing the variance of the photon number as $\sigma_{\mathrm{n}}^2 = <\Psi_0|\hat{n}^2|\Psi_0> - <\Psi_0|\hat{n}|\Psi_0>^2$. From Eq. (14), the short-time evolution of the mean square of the photon-number operator is calculated as

$$\begin{aligned} <\Psi_0|\hat{n}^2(t_0+\tau)|\Psi_0> &= <\Psi_0|\left\{\hat{a}^\dagger(t_0+\tau)\hat{a}(t_0+\tau)\right\}^2|\Psi_0> \\ &= <\Psi_0|\left[\left\{\hat{a}^\dagger(t_0)\left(1-\hat{\Pi}^\dagger(t_0)\right)+\hat{\mathrm{P}}^\dagger(t_0)\right\}\left\{\hat{a}(t_0)\left(1-\hat{\Pi}(t_0)\right)+\hat{\mathrm{P}}(t_0)\right\}\right]^2|\Psi_0> \\ &= <\Psi|\hat{n}^2(t_0)|\Psi> \left\{1+4\kappa^2(N_2-N_1)\pi\tau\right\}+2\overline{n}(t_0)\kappa^2(3N_2+N_1)\pi\tau+2\kappa^2N_2\pi\tau, \end{aligned} \tag{37}$$

where higher-order interaction terms are neglected as before. This expression can be translated to the short-length evolution as

$$<\Psi_0|\hat{n}^2(z_0+\Delta z)|\Psi_0> = <\Psi|\hat{n}^2(z_0)|\Psi> \{1+2g(N_2-N_1)\Delta z\}+g\overline{n}(z_0)(3N_2+N_1)\Delta z+gN_2\Delta z, \tag{38}$$

from which the following differential equation is obtained:

$$\frac{d<\hat{n}^2>}{dz} = 2g(N_2-N_1)<\hat{n}^2> + g(3N_2+N_1)\overline{n}+gN_2. \tag{39}$$

with $<\hat{n}^2> = <\Psi|\hat{n}^2|\Psi>$. The first term represents an amplification process with a gain coefficient of $2g(N_2 - N_1)$, and the second and third terms represent the number of photons generated at a local position, which propagate and reach the medium end while being amplified by the first term. Then, the solution of Eq. (39) can be expressed as

$$<\hat{n}^2(L)> = <\hat{n}^2(0)> e^{2g(N_2-N_1)L} + \int_0^L \left\{g(3N_2+N_1)\overline{n}(z)+gN_2\right\}e^{2g(N_2-N_1)(L-z)}dz. \tag{40}$$

Here, $\overline{n}(z)$ is expressed from Eq. (29) as $\overline{n}(z) = \overline{n}(0)\exp[g(N_2-N_1)z]$, and then Eq. (40) is calculated as

$$< \hat{n}^2(L) >=< \hat{n}^2(0) > G^2 + n_{\mathrm{sp}}(G-1) + 4\overline{n}(0)G(G-1)n_{\mathrm{sp}} + 2n_{\mathrm{sp}}^2(G-1)^2 - \overline{n}(0)G(G-1). \tag{41}$$

From this equation and Eq. (29), the photon-number variance at the amplifier output is expressed as

$$\begin{aligned}\sigma_{\mathrm{n}}^2(L) >&=< \hat{n}^2(L) > -\{\overline{n}(L)\}^2 \\ &= 2\overline{n}(0)G(G-1)n_{\mathrm{sp}} + n_{\mathrm{sp}}^2(G-1)^2 + \overline{n}(0)G + n_{\mathrm{sp}}(G-1) \\ &\quad + G\left[< \hat{n}^2(0) > -\{\overline{n}(0)\}^2 - \overline{n}(0)\right].\end{aligned} \tag{42}$$

Recalling that the mean photon numbers of the amplified signal and the spontaneous emission are $\overline{n}(0)G$ and $n_{\mathrm{sp}}(G-1)$, respectively, each term in Eq. (42) can be interpreted as follows. The first term is equivalent to 2 × (signal light intensity) × (spontaneous light intensity), corresponding to the signal-spontaneous beat noise represented by the first term in Eq. (4). The second term is equivalent to (spontaneous light intensity)^2, corresponding to the spontaneous-spontaneous beat noise represented by the second and third terms in Eq. (4). The third and fourth terms denote the mean photon numbers of the amplified signal and spontaneous emission, respectively, corresponding to the inherent quantum noises of the amplified signal light and the spontaneous emission, respectively. In the fifth term, $< \hat{n}^2 (0) > -\{\overline{n}(0)\}^2$ is the photon-number variance at the input and $\overline{n}(0)$ is that of a coherent state. Thus, their difference represents noise other than the inherent quantum noise, i.e., excess noise, and then the fifth term corresponds to the amplified excess noise.

The first and second terms in Eq. (42) correspond to the classical intensity noise represented by Eq. (4), as described above, supporting the classical treatment. In addition, the inherent quantum noises are included in Eq. (42), owing to the full quantum mechanical treatment, and the amplified excess noise is simultaneously included as well. Sometimes in the classical treatment, the inherent quantum noise is phenomenologically added as the shot noise arising at the electrical stage after direct detection [2]. In fact, however, it exists in the optical stage as derived above. Therefore, the inherent quantum noise is sometimes called "optical shot noise."

4.6. Noise figure

The noise figure, defined as the ratio of the signal-to-noise ratios (SNRs) at the input and output of an amplifier in terms of the light intensity or the photon number, is usually used as an indicator for the noise performance of an amplifier. Based on the above results, we describe the noise figure of population-inversion-based amplifiers in this subsection. The output SNR is obtained from Eqs. (29) and (42) as

$$(\mathrm{SNR})_{\mathrm{out}} = \frac{\{\overline{n}(0)G\}^2}{2\overline{n}(0)G(G-1)n_{\mathrm{sp}}}, \tag{43}$$

where only the signal power and the signal-spontaneous beat noise are taken into account, assuming that the amplified signal is sufficiently larger than the spontaneous emission. On the other hand, the input SNR is evaluated for a coherent state, according to the definition of the noise figure, which is $(\text{SNR})_{\text{in}} = \overline{n}(0)$. Therefore, the noise figure is expressed as

$$\text{NF} = \frac{(\text{SNR})_{\text{in}}}{(\text{SNR})_{\text{out}}} = 2n_{\text{sp}}\frac{G-1}{G}. \tag{44}$$

This expression equals the classical result given by Eq. (6).

The noise figure is proportional to the population inversion parameter $n_{\text{sp}} = N_2/(N_2 - N_1)$, as shown above. The minimum value of n_{sp} is 1, which is achieved when $N_1 = 0$, i.e., the fully inverted condition where all atoms are in the upper states. Under this condition, NF = 3 dB for $G >> 1$. This is the quantum-limited noise figure of population-inversion-based optical amplifiers. Near-quantum-limited noise figure has been demonstrated experimentally in Erbium-doped fiber amplifiers [6, 7].

The fact that the noise performance is determined by the population inversion parameter can be intuitively understood as follows. The source of amplifier noise is spontaneous emission. A small amount of spontaneous emission suggests a good noise performance. However, spontaneous emission is roughly proportional to the signal gain (Eq. (29)), which is desired to be high as an amplifier. Thus, the amount of spontaneous emission normalized to the signal gain, (ASE power)/(signal gain), can be an indicator for the noise performance. The spontaneous emission rate is proportional to the number of atoms in the upper energy level N_2, i.e., (ASE power)$\propto N_2$, and the signal gain is determined by the balance between stimulated emission and absorption and thus is proportional to the difference between the numbers of atoms in the upper and lower states, roughly speaking, i.e., (signal gain)$\propto(N_2 - N_1)$. Subsequently, (ASE power)/(signal gain)$\propto N_2/(N_2 - N_1) = n_{\text{sp}}$, which suggests that the amplifier noise performance is determined by the population inversion parameter n_{sp}.

5. Optical parametric amplifiers

Whereas population-inversion–based amplifiers are widely used, there is another type of optical amplifiers, that is an optical parametric amplifier (OPA) based on optical nonlinearity [8]. When signal light is incident onto a nonlinear medium along with intense pump light, a signal and idler photons are created from one pump photon in case of second-order nonlinearity, satisfying the energy conservation of $\hbar\omega_{\text{s}} + \hbar\omega_{\text{i}} = \hbar\omega_{\text{p}}$ (ω_{s}, ω_{i}, and ω_{p} are the angular frequencies of the signal, idler, and pump lights, respectively), or they are created from two pump photons in case of third-order nonlinearity, satisfying $\hbar\omega_{\text{s}} + \hbar\omega_{\text{i}} = \hbar\omega_{\text{p1}} + \hbar\omega_{\text{p2}}$. Through this photon exchange phenomenon, the signal light is amplified. This signal amplification scheme also offers optical signal processing functions such as wavelength conversion and generation of phase-conjugated light [9]. This section describes quantum noise in OPAs [10].

5.1. Heisenberg equation

The Hamiltonian for parametric interaction between signal and idler via pump light(s) can be expressed as [11]

$$\widehat{H} = \hbar\omega_{\mathrm{s}}\widehat{a}_{\mathrm{s}}^{\dagger}\widehat{a}_{\mathrm{s}} + \hbar\omega_{\mathrm{i}}\widehat{a}_{\mathrm{i}}^{\dagger}\widehat{a}_{\mathrm{i}} + i\hbar\left(\chi\widehat{a}_{\mathrm{s}}^{\dagger}\widehat{a}_{\mathrm{i}}^{\dagger} - \chi^{*}\widehat{a}_{\mathrm{s}}\widehat{a}_{\mathrm{i}}\right). \tag{45}$$

The first and second terms are the Hamiltonians of signal and idler lights without interaction, respectively, where $\widehat{a}_{\mathrm{s}}$ and $\widehat{a}_{\mathrm{i}}$ are the field operators of signal and idler, respectively. The third term is the interaction Hamiltonian between signal, idler, and pump lights, which represents photon energy exchange such that signal and idler photons are created while pump photon(s) is annihilated and vice versa, with the coupling coefficient χ. Since the pump light is so intense that its quantum properties do not matter here, the pump light is treated classically, whose amplitude E_{p} is included in the coupling coefficient as $\chi \propto E_{\mathrm{p}}$ or $E_{\mathrm{p1}}E_{\mathrm{p2}}$ for the second- or third-order nonlinear interaction, respectively.

From the Heisenberg equation with the above Hamiltonian, temporal differential equations for the field operators are obtained as

$$\frac{d\widehat{a}_{\mathrm{s}}}{dt} = \frac{1}{i\hbar}\left[\widehat{a}_{\mathrm{s}}, \widehat{H}\right] = -i\omega_{\mathrm{s}}\widehat{a}_{\mathrm{s}} + \chi\widehat{a}_{\mathrm{i}}^{\dagger}, \tag{46a}$$

$$\frac{d\widehat{a}_{\mathrm{i}}^{\dagger}}{dt} = \frac{1}{i\hbar}\left[\widehat{a}_{\mathrm{i}}^{\dagger}, \widehat{H}\right] = i\omega_{\mathrm{i}}\widehat{a}_{\mathrm{i}}^{\dagger} + \chi^{*}\widehat{a}_{\mathrm{s}}. \tag{46b}$$

These temporal differential equations can be translated to spatial ones as

$$\frac{d\widehat{a}_{\mathrm{s}}}{dz} = -i\beta_{\mathrm{s}}\widehat{a}_{\mathrm{s}} + \frac{\chi}{(c/n)}\widehat{a}_{\mathrm{i}}^{\dagger}, \tag{47a}$$

$$\frac{d\widehat{a}_{\mathrm{i}}^{\dagger}}{dz} = i\beta_{\mathrm{i}}\widehat{a}_{\mathrm{i}}^{\dagger} + \frac{\chi^{*}}{(c/n)}\widehat{a}_{\mathrm{s}}. \tag{47b}$$

where $\beta = n\ (\omega/c)$ is the propagation constant (n: the refractive index, c: the light velocity in the vacuum). The above equations can be simplified by the variable translation $\widehat{a}_{\mathrm{s,i}}(z) \rightarrow \widehat{a}_{\mathrm{s,i}}(z)$ $\exp\left(-i\beta_{\mathrm{s,i}}z\right)$ as

$$\frac{d\widehat{a}_{\mathrm{s}}}{dz} = \frac{\chi}{(c/n)}\widehat{a}_{\mathrm{i}}^{\dagger}e^{i\left(\beta_{\mathrm{s}}+\beta_{\mathrm{i}}\right)z}, \tag{48a}$$

$$\frac{d\widehat{a}_{\mathrm{i}}^{\dagger}}{dz} = \frac{\chi^{*}}{(c/n)}\widehat{a}_{\mathrm{s}}e^{-i\left(\beta_{\mathrm{s}}+\beta_{\mathrm{i}}\right)z}. \tag{48b}$$

Here, we consider the propagation phase of the right-hand term in the above equations. The coefficient χ includes the pump light amplitude as $\chi \propto E_{\mathrm{p}}$ or $E_{\mathrm{p1}}E_{\mathrm{p2}}$, and the pump amplitude can be expressed as $E_{\mathrm{p}} = E_{\mathrm{p}}\ (0)\exp(-i\beta_{\mathrm{p}}z)$ under no pump-depletion condition (β_{p} is the propagation constant of the pump light). Subsequently, $\chi \propto E_{\mathrm{p}}\ (0)\exp(-i\beta_{\mathrm{p}}z)$ or $E_{\mathrm{p1}}(0)E_{\mathrm{p2}}(0)$ $\exp[-i(\beta_{\mathrm{p1}} + \beta_{\mathrm{p2}})z]$. From these considerations, Eq. (48) can be rewritten as

$$\frac{d\widehat{a}_{\mathrm{s}}}{dz} = \kappa\widehat{a}_{\mathrm{i}}^{\dagger}e^{i\Delta\beta z}, \tag{49a}$$

$$\frac{d\hat{a}_{\mathrm{i}}^{\dagger}}{dz} = \kappa^{*}\hat{a}_{\mathrm{s}}e^{-i\Delta\beta z}. \tag{49b}$$

where κ is the coupling coefficient in the spatial domain, excluding $\exp(-i\beta_{\mathrm{p}}z)$ or $\exp[-i(\beta_{\mathrm{p1}} + \beta_{\mathrm{p2}})z]$, and $\Delta\beta \equiv \beta_{\mathrm{s}} + \beta_{\mathrm{i}} - \beta_{\mathrm{p}}$ or $\beta_{\mathrm{s}} + \beta_{\mathrm{i}} - \beta_{\mathrm{p1}} - \beta_{\mathrm{p2}}$. This parameter $\Delta\beta$ is called "phase mismatch," and determines the signal gain of an OPA as shown later. As for κ, its absolute value is $|\kappa| = d\gamma|E_{\mathrm{p1}}|\,|E_{\mathrm{p2}}|$ when an optical fiber is used as a nonlinear medium, where γ is the nonlinear coefficient, and d is the degeneracy factor that takes 2 and 1 for $f_{\mathrm{p1}} \neq f_{\mathrm{p2}}$ and $f_{\mathrm{p1}} = f_{\mathrm{p2}}$, respectively. Regarding the phase of κ, it is determined by the incident phase(s) of the pump light(s).

From Eq. (49), the signal field operator at the output is calculated as

$$\hat{a}_{\mathrm{s}}(L) = \left\{\cosh(gL) - i(\Delta\beta/2g)\sinh(gL)\right\}\hat{a}_{\mathrm{s}}(0) + e^{i\varphi}\sqrt{1 + (\Delta\beta/2g)^{2}}\sinh(gL)\hat{a}_{\mathrm{i}}^{\dagger}(0), \tag{50a}$$

where $g \equiv \{|\kappa|^{2} - (\Delta\beta/2)^{2}\}^{1/2}$, L is the medium length, and $\varphi \equiv \arg(\kappa)$. Eq. (50a) includes the field operators of signal and idler lights, i.e., the signal and the idler are treated separately. For particular frequency conditions such as $2\omega_{\mathrm{s}} = \omega_{\mathrm{p}}$ for the second-order nonlinearity or $2\omega_{\mathrm{s}} = \omega_{\mathrm{p1}} + \omega_{\mathrm{p2}}$ for the third-order nonlinearity, the idler frequency equals to the signal frequency, $\omega_{\mathrm{i}} = \omega_{\mathrm{s}}$, and the signal and the idler are degenerate. Under such conditions, Eq. (50a) is rewritten as

$$\hat{a}_{\mathrm{s}}(L) = \left\{\cosh(gL) - i(\Delta\beta/2g)\sinh(gL)\right\}\hat{a}_{\mathrm{s}}(0) + e^{i\varphi}\sqrt{1 + (\Delta\beta/2g)^{2}}\sinh(gL)\hat{a}_{\mathrm{s}}^{\dagger}(0), \tag{50b}$$

As shown later, degenerate and nondegenerate OPAs have definitely different characteristics. For simplifying mathematical expressions, hereafter, we rewrite Eq. (50) as

$$\hat{a}_{\mathrm{s}}(L) = \left\{Ae^{i(\varphi-\phi)/2}\hat{a}_{\mathrm{s}}(0) + Be^{-i(\varphi-\phi)/2}\hat{a}_{\mathrm{i,s}}^{\dagger}(0)\right\}e^{i(\varphi+\phi)/2}, \tag{51}$$

with

$$A = \sqrt{\cosh^{2}(gL) + (\Delta\beta/2g)^{2}\sinh^{2}(gL)}, \tag{52a}$$

$$\phi = \arctan\left[-\frac{(\Delta\beta/2g)\sinh(gL)}{\cosh(gL)}\right], \tag{52b}$$

$$B = \sqrt{1 + (\Delta\beta/2g)^{2}}\sinh(gL). \tag{52c}$$

The mean values of the physical quantities after amplification can be evaluated using Eq. (51). In the evaluation, we need the initial state in addition. Here, we assume that only signal light is incident to an OPA, and express the initial state as $|\Psi_{0}> = |\Psi>_{\mathrm{s}}\otimes|0>_{\mathrm{i}}$, where $|\Psi>_{\mathrm{s}}$ and $|0>_{\mathrm{i}}$ denote the signal and idler states, respectively. When the initial state is a coherent state as $|\Psi>_{\mathrm{s}} = |\alpha>$, we have $\hat{a}_{\mathrm{s}}(0)|\Psi> = \sqrt{\overline{n}_{\mathrm{s}}(0)}e^{i\theta}|\Psi>$, where $\overline{n}_{\mathrm{s}}(0)$ and θ are the mean photon number and the phase of the incident signal light, respectively. On the other hand, $\hat{a}_{\mathrm{i}}(0)|0>_{\mathrm{i}} = 0$.

5.2. Mean amplitude, photon number, and signal gain

The mean amplitude and photon number at the output are evaluated by $\overline{a}_s(L) =< \Psi_0|\widehat{a}_s(L)|\Psi_0 >$ and $\overline{n}_s(L) =< \Psi_0|\widehat{a}_s^\dagger(L)\widehat{a}_s(L)|\Psi_0 >$, respectively. For nondegenerate OPA, these are calculated from Eq. (51) as

$$\overline{a}_s(L) = \overline{a}_s(0)Ae^{i\varphi}, \tag{53}$$

$$\overline{n}_s(L) = \overline{n}_s(0)A^2 + B^2. \tag{54}$$

Eq. (53) indicates that the signal field is simply amplified while preserving the phase state, with no additional field on average. On the other hand, Eq. (54) shows that the output photons consist of two components. The first term is proportional to the incident photon number, which corresponds to the amplified signal photons with a gain of

$$A^2 = \cosh^2(gL) + \left(\Delta\beta/2g\right)^2 \sinh^2(gL) \equiv G. \tag{55}$$

It is noted in this expression that parameter $g = \{|\kappa|^2 - (\Delta\beta/2)^2\}^{1/2}$ is equivalent to the gain coefficient. When $\Delta\beta = 0$, g is maximum and the signal gain is maximum. Therefore, it is important to satisfy the condition $\Delta\beta = 0$, that is called the "phase matching condition," in implementing an OPA [9]. The second term in Eq. (54) is independent on the signal input, and represents spontaneously emitted photons. The above results, i.e., the spontaneous light does not appear in the mean amplitude while it does in the photon number, suggest that the amplitude of the spontaneous emission is completely random. However, we do not know how random it is at this stage. The photon number of the spontaneous emission is expressed from the second term in Eqs. (54) and (52c) as

$$B^2 = \left\{1 + \left(\Delta\beta/2g\right)^2\right\}\sinh^2(gL) = G - 1, \tag{56}$$

where Eq. (55) is applied. This expression is equivalent to the spontaneous photon number in population-inversion-based amplifiers indicated in Eq. (29) with $n_{sp} = 1$. This correspondence suggests that nondegenerate OPAs can offer the ideal noise performance achievable in EDFAs, which is shown later.

Regarding degenerate OPA, on the other hand, its mean output amplitude is calculated as

$$\overline{a}_s(L) = \left\{Ae^{i\left\{\theta_0 + (\varphi - \phi)/2\right\}} + Be^{-i\left\{\theta_0 + (\varphi - \phi)/2\right\}}\right\}|\overline{a}_s(0)|e^{i(\varphi + \phi)/2}, \tag{57}$$

where θ_0 is the phase of the incident signal light. The mean output amplitude does not have a simple form as in nondegenerate OPA (Eq. (53)). Under the condition where $\Delta\beta = 0$ and the gain coefficient g is so large as $\cosh(gL) \approx \sinh(gL) \approx e^{gL}/2$, Eq. (57) is approximated as

$$\overline{a}_s(L) = \cos(\Delta)e^{gL}|\overline{a}_s(0)|e^{i(\varphi+\phi)/2}, \tag{58}$$

where $\Delta \equiv \theta_0 + (\varphi - \phi)/2$ is introduced. This expression indicates that the phase state of the incident signal light is not transferred to the output.

The mean photon number in degenerate OPA is calculated from Eq. (51) as

$$\overline{n}_{\mathrm{s}}(L) = \left(A^2 + B^2\right)\overline{n}_{\mathrm{s}}(0) + AB\left\{ < \Psi| \left[\{\widehat{a}_{\mathrm{s}}(0)\}^2 e^{i(\varphi-\phi)/2} + \left\{\widehat{a}_{\mathrm{s}}^{\dagger}(0)\right\}^2 e^{-i(\varphi-\phi)/2} \right] |\Psi > \right\} + B^2. \quad (59)$$

Unfortunately, this equation cannot be further developed, because we cannot readily calculate $< \Psi|\{\widehat{a}_{\mathrm{s}}(0)\}^2|\Psi >$ and $< \Psi|\left\{\widehat{a}_{\mathrm{s}}^{\dagger}(0)\right\}^2|\Psi >$ for an arbitrary $|\Psi>$. However, for a coherent incident state, these quantities can be evaluated using $\widehat{a}_{\mathrm{s}}(0)|\Psi >= \sqrt{\overline{n}_{\mathrm{s}}(0)}e^{i\theta}|\Psi >$, and then Eq. (59) is developed as

$$\overline{n}_{\mathrm{s}}(L) = \overline{n}_{\mathrm{s}}(0)\left\{A^2 + B^2 + 2AB\cos(2\Delta)\right\} + B^2. \quad (60)$$

In this expression, the first term represents amplified signal photons, and the second term represents spontaneous emission whose mean amplitude is zero as indicated in Eq. (57).

From the first term in Eq. (60), the signal gain is expressed as

$$G = A^2 + B^2 + 2AB\cos(2\Delta), \quad (61)$$

which is dependent on the relative phase $\Delta = \theta_0 + (\varphi - \phi)/2$. Hence, degenerate OPA is called "phase-sensitive amplifier (PSA)." The maximum gain is obtained when $\Delta = 0$ as

$$G(\Delta = 0) = (A + B)^2. \quad (62)$$

5.3. Amplitude fluctuation

Next, we evaluate the amplitude noise in OPAs. For the evaluation, the light amplitude is decomposed into two quadratures and the variance of each quadrature is calculated, as in Section 4.3. In case of OPAs, the output field operator is phase-shifted by $(\varphi + \phi)/2$, as indicated by Eq. (51). Accordingly, we introduce a phase-shifted field operator defined as $\widehat{b} \equiv \widehat{a}_{\mathrm{s}}e^{-i(\phi+\varphi)/2}$, and evaluate the variances of the real and imaginary components of $\widehat{b}$, i.e., $\widehat{x}_1 = \left(\widehat{b} + \widehat{b}^{\dagger}\right)/2$ and $\widehat{x}_2 = \left(\widehat{b} - \widehat{b}^{\dagger}\right)/2i$, respectively, as $\sigma_{x1(2)}^2 = <\Psi_0|\widehat{x}_{1,2}^2|\Psi_0> - <\Psi_0|\widehat{x}_{1,2}|\Psi_0>^2$.

The calculation result for nondegenerate OPA is expressed as

$$\sigma_{x1(2)}^2(L) = A^2\sigma_{x1(2)}^2(0) + \frac{1}{4}B^2 = A^2\sigma_{x1(2)}^2(0) + \frac{1}{4}(G - 1), \quad (63)$$

where Eqs. (55) and (56) are applied. The first term represents noise amplified from the incident light, and the second term represents additional noise superimposed via OPA. Note that Eq. (63) is equivalent to the amplitude variance of population-inversion-based amplifiers shown by Eq. (35) with $n_{\mathrm{sp}} = 1$, suggesting that the ideal noise performance achievable in EDFAs can be obtained in OPA. Similar to Eq. (35), Eq. (63) is rewritten for a coherent incident state as

$$\sigma_{x1(2)}^2(L) = \frac{1}{4} + \frac{1}{2}(G-1). \tag{64}$$

The first term is the inherent quantum noise of a coherent state, and the second term represents noise superimposed via OPA in a classical picture. The sum of the second terms of the two quadratures equals the photon number of spontaneous emission light indicated in Eq. (56). This consideration supports the classical noise treatment, described in Section 2, where spontaneous emission with random phase is superimposed onto signal light at the amplifier output.

For degenerate OPA, on the other hand, the amplitude variances are calculated as

$$\sigma_{x1}^2(L) = (A+B)^2\sigma_{x1}^2(0) = G_0\sigma_{x1}^2(0), \tag{65a}$$

$$\sigma_{x2}^2(L) = (A-B)^2\sigma_{x2}^2(0), \tag{65b}$$

where $G_0 \equiv G(\Delta = 0)$ is the phase-synchronized gain introduced in Eq. (62). The results show that the output variances are unequal in the two quadratures, such that ${\sigma_{x1}}^2$ is enhanced while ${\sigma_{x2}}^2$ is depressed. Since $\hat{x}_1$ and $\hat{x}_2$ are the real and imaginary parts of the phase-shifted operator, respectively, this result suggests that amplitude noise along the axis of a phase of $(\varphi + \phi)/2$ is enhanced and that along the orthogonal axis is depressed, in the complex amplitude space. It is noted in Eq. (65a) that it only has fluctuations amplified from incident light with no additional fluctuation, unlike population-inversion-based amplifiers (Eq. (35)) and nondegenerate OPA (Eq. (63)). This result suggests that even the noise-enhanced quadrature $\hat{x}_1$ is expected to have lower noise than these amplifiers. Regarding the imaginary part, Eq. (65b) for high-gain conditions, where $\cosh(gL) \approx \sinh(gL) \approx e^{gL}/2$ and then $A \approx B$, is rewritten as ${\sigma_{x1}}^2 \approx 0$. This consideration indicates that the amplitude noise along the phase axis orthogonal to the signal output phase approaches zero as the signal gain increases. The above-mentioned characteristics of amplitude fluctuation in degenerate OPA can be illustrated in the complex amplitude space as shown in **Figure 3**.

5.4. Photon-number fluctuation and noise figure

Next, we discusses photon-number fluctuations in OPAs, which are evaluated through the photon-number variance as ${\sigma_n}^2 = <\Psi_0|\hat{n}^2|\Psi_0> - <\Psi_0|\hat{n}|\Psi_0>^2$. Using Eq. (51), the average of the square of the photon-number operator for nondegenerate OPA is calculated as

$$< \Psi_0|\hat{n}_s^2(L)|\Psi_0 >=< \Psi_0|\left\{\hat{a}_s^\dagger(L)\hat{a}_s(L)\right\}^2|\Psi_0 >=< \Psi_0|\hat{n}_s(L)|\Psi_0>^2 + \left(A^2+B^2\right)A^2\overline{n}_s(0) + (AB)^2. \tag{66}$$

Subsequently, the photon-number variance is obtained as

$$\begin{aligned}\sigma_n^2(L) &= \left(A^2+B^2\right)A^2\overline{n}_s(0) + (AB)^2 = (2G-1)G\overline{n}_s(0) + G(G-1) \\ &= 2(G-1)G\overline{n}_s(0) + (G-1)^2 + G\overline{n}_s(0) + G(G-1),\end{aligned} \tag{67}$$

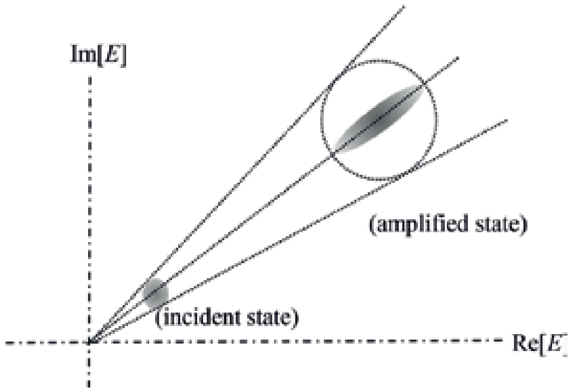

Figure 3. Constellation diagram of amplified light in a phase-synchronized degenerate OPA.

where Eqs. (55) and (56) are applied. Recalling that the mean photon number of the amplified signal is $G\overline{n}_{\rm s}(0)$ and that of spontaneous emission light is $(G-1)$, as indicated by Eqs. (54)–(56), each term in Eq. (68) can be interpreted as follows. The first term is equivalent to 2 × (signal light intensity) × (spontaneous light intensity), which corresponds to the signal-spontaneous beat noise. The second term is equivalent to (spontaneous light intensity)^2, which corresponds to the spontaneous-spontaneous beat noise. The third and fourth terms are equal to the mean photon numbers of the amplified signal and of spontaneous emission, respectively, and correspond to the optical shot noises of the amplified signal light and the spontaneous emission, respectively.

Next, we consider degenerate OPA. As indicated by Eq. (59), properties of the photon number in degenerate OPA are hard to evaluate for an arbitrary initial state. Thus, we assume a coherent incident state here. From Eq. (51), the average of the square of the photon-number operator for the initial state $|\Psi_0\rangle = |\alpha\rangle_{\rm s} \otimes |0\rangle_{\rm i}$ is calculated as

$$\begin{aligned}
< \Psi_0|\widehat{n}_{\rm s}^{\,2}(L)|\Psi_0 >&= [A^2 + B^2 + 2AB\cos(2\Delta)\overline{n}_{\rm s}(0) + B^2]^2 \\
&\quad + \left\{\left(A^2+B^2\right)^2 + 4(AB)^2 + 4\left(A^2+B^2\right)AB\cos(2\Delta)\right\}\overline{n}_{\rm s}(0) + 2(AB)^2 \\
&=< \Psi_0|\widehat{n}_{\rm s}(L)|\Psi_0>^2 + \left\{\left(A^2+B^2\right)^2 + 4(AB)^2 + 4\left(A^2+B^2\right)AB\cos(2\Delta)\right\}\overline{n}_{\rm s}(0) + 2(AB)^2, \qquad (68)
\end{aligned}$$

Subsequently, the photon-number variance at the output is

$$\begin{aligned}
\sigma_{\rm n}^2(L) &= \left\{\left(A^2+B^2\right)^2 + 4(AB)^2 + 4\left(A^2+B^2\right)AB\cos(2\Delta)\right\}\overline{n}_{\rm s}(0) + 2(AB)^2 \\
&= \left\{G^2 + 4(AB)^2\sin^2(2\Delta)\right\}\overline{n}_{\rm s}(0) + 2(AB)^2,
\end{aligned} \qquad (69)$$

where Eq. (61) is applied. This expression cannot be decomposed and interpreted as that of nondegenerate OPA indicated by Eq. (68), which could be because the amplitude distribution is not simply isotropic in two quadratures, unlike nondegenerate OPA.

The noise figure can be evaluated from the results obtained above. For nondegenerate OPA, it is obtained as

$$\mathrm{NF} = \frac{(\mathrm{SNR})_{\mathrm{in}}}{(\mathrm{SNR})_{\mathrm{out}}} = \overline{n}_{\mathrm{s}}(0)\frac{2(G-1)G\overline{n}_{\mathrm{s}}(0)}{\{G\overline{n}_{\mathrm{s}}(0)\}^2} = 2\frac{G-1}{G}. \tag{70}$$

where only the signal-spontaneous beat noise is considered for the output SNR, according to the definition on the noise figure. This noise figure equals that of ideal population-inversion–based amplifiers indicated by Eq. (44) with $n_{\mathrm{sp}} = 1$. For the degenerate case, on the other hand, it is expressed as

$$\mathrm{NF} = 1 + 4\frac{(AB)^2}{G}\sin^2(2\Delta). \tag{71}$$

For $\Delta = 0$, NF = 1 (0 dB), suggesting no SNR degradation in phase-synchronized degenerate OPA. In fact, a noise figure of less than 3 dB in a phase-sensitive amplifier has been experimentally demonstrated [12, 13].

6. Conclusion

This chapter describes quantum noise of optical amplifiers. Full quantum mechanical treatment based on the Heisenberg equation for physical quantity operators was presented, by which quantum properties of optical amplifiers were derived from first principles. The obtained results are consistent with a conventional classical treatment, except for the inherent quantum noise or the zero-point fluctuation, providing the theoretical base to the conventional phenomenological treatment.

Author details

Kyo Inoue

Address all correspondence to: kyo@comm.eng.osaka-ua.c.jp

Osaka University, Osaka, Japan

References

[1] Yamamoto Y, Inoue K. Noise in amplifiers. Journal of Lightwave Technology. 2003;**21**: 2895-2915. DOI: 10.1109/JLT.2003.816887

[2] Olsson N. Lightwave system with optical amplifiers. Journal of Lightwave Technology. 1989;**7**:1071-1082

[3] Yariv A. Quantum Electronics. 3rd ed. USA: Wiley; 1989. 676 p

[4] Loudon R. The Quantum Theory of Light. 3rd ed. New York: Oxford; 2000. 438 p

[5] Inoue K. Quantum mechanical treatment of optical amplifiers based on population inversion. IEEE Journal of Quantum Electronics. 2014;**50**:563-567. DOI: 10.1109/JQE.2014.2325906

[6] Smart RG, Zyskind JL, Sulhoff JW, DiGiovanni DJ. An investigation of the noise figure and conversion efficiency of 0.98 μm pumped erbium-doped fiber amplifiers under saturated conditions. IEEE Photonics Technology Letters. 1992;**4**:1261-1264

[7] Laming RI, Zechael MN, Payne DN. Erbium-doped fiber amplifier with 54 dB gain and 3.1 dB noise figure. IEEE Photonics Technology Letters. 1992;**4**:1345-1347

[8] Marhic M. Fiber Optical Parametric Amplifiers, Oscillators and Related Devices. 1st ed. New York: Cambridge; 2008. 366 p

[9] Hansryd J, Andrekson PA, Westlund M, Li J, Hedekvist P. Fiber-based optical parametric amplifiers and their applications. IEEE Journal of Selected Topics in Quantum Electronics. 2002;**8**:506-520

[10] Inoue K. Quantum noise in parametric amplification under phase-mismatched conditions. Optics Communication. 2016;**366**:71-76. DOI: 10.1016/j.optcom.2015.12.034

[11] Walls D, Milburn G. Quantum Optics. 2nd ed. Berlin: Springer; 2008. 425 p

[12] Imajuku W, Takada A, Yamabayashi Y. Inline coherent optical amplifier with noise figure lower than 3 dB quantum limit. Electronics Letters. 2000;**36**:63-64

[13] Tong Z, Bogris A, Lundström C, McKinstrie CJ, Vasilyev M, Karosson M, Andrekson A. Modeling and measurement of the noise figure of a cascaded non-degenerate phase-sensitive parametric amplifier. Optics Express. 2010;**18**:14820-14835

Edited by Pankaj Kumar Choudhury

Optical amplifiers are indispensable in long-haul communication systems operating in a relatively broad range of electromagnetic spectra. Various forms of optical amplifiers and their advancements have been extensively discussed in the literature emphasizing the relative merits and demerits of different types of configurations and/or designs and also usefulness in specific applications. The book—*Optical Amplifiers: A Few Different Dimensions*—aims at reporting developments in these devices in the recent years. The contributed chapters in this book encompass both theoretical and experimental results covering various aspects in the relevant research directions. This somehow makes the volume useful to both experts and novice researchers. Finally, the expectation remains of the contents to be of some merit for the R&D scientists working in universities and research institutions.

Published in London, UK

IntechOpen

ISBN 978-1-83881-480-9